NUI MAYNOOTH
Ollscoil na hÉireann Má Nuad

Development of a scanning system for use in the Terahertz region of the Electromagnetic Spectrum

Presented by

Brian Mc Laughlin B.Sc

A thesis submitted for the Degree of

Master of Science

Department of Experimental Physics

NUI Maynooth

Co. Kildare

Ireland

October 2012

Head of Department

Professor J. A. Murphy, MSc, MS, PhD.

Research Supervisor

Dr Marcin Gradziel MSc, PhD.

Table of Contents

Abstract

This thesis concerned the development of a scanner system for use in the Terahertz region of the Electromagnetic spectrum. The approach used by the prototype developed, utilises two tilting mirrors for the purposes of scanning a target under investigation. An object is scanned by tilting an incident beam of radiation to a point of interest on the target, on this basis an image can be formed on a point by point basis.

The Thesis begins with an Introduction to THz radiation and its associated properties. The need for a Terahertz scanner and the potential applications in the biomedical, security and space research are outlined. The reader is then introduced to various approaches utilised by currently existing scanners and the approach used for the work carried out in this thesis outlined in detail.

The techniques used for computationally modelling diffraction limited optical systems are discussed namely Fresnel Diffraction, Gaussian Beam Mode Analysis (GBMA) and Physical Optics. The effectiveness of these techniques are highlighted by using each method to model elementary optical systems. The techniques are then used to computationally model the optical system used for the prototype developed and results presented.

The final section is concerned with the development of the prototype including background theory on components used, implementation of the components and verification of alignment procedure. The development of the computer controlled tilting mirror system and its integration with the prototype is also outlined. Finally the results of the operational scanning prototype are presented and discussed.

Acknowledgements

First and foremost I would like to thank my supervisor Dr. Marcin Gradziel for his commitment and dedication throughout the course of this research project, without your input this work would not have been undertaken. I would also like to thank the Head of the department Prof. Anthony Murphy for placing the facilities of the department at my disposal.

I would like to thank my parents, Eilish and John who have supported me in many ways not only over the last few years of University but over the last 25 years. Thanks also to my sisters Sarah, Anna and Laura for your support and encouragement throughout the years.

I would also like to say thanks to all the staff of the Experimental Physics department for their help and guidance over the course of this work and throughout my Undergraduate years. Special recognition goes to Mr. Pat Seery and Mr. David Watson for their help with the stepper motor implementation and manufacture of the phase modulating dielectric. Also many thanks go to Ms. Gráinne Roche and Mr. John Kelly, Mr. Ian McAuley and Mr. Derek Gleeson who were always happy to help me with any problems that arose.

Gratitude must also be expressed to Dr. Vladimir Yurchenko for providing the dielectric lenses used and aiding in their description and use.

Thanks also to Dr. Neil Trappe, Mr. Gerry Mc Mahon, Dr. Frank Mulligan, and Dr. Peter Van Der Burgt for affording me the opportunity to demonstrate undergraduate laboratories under their guidance. Also a special thanks to Dr. Niall Mc Keith for allowing me to take care of the science museum during the summer months.

I would also like to thank my office mates Mairéad Bevan, Ronan Mahon and Francis Mahon for keeping me sane and for putting up with me over the last two years, I'm sure it can't have been easy at times. Thanks also to my housemates Paul Mc Laughlin, Donnacha Gayer, Deirdre Mullen and Robert Dixon for the truly deep conversations about everything and anything and introducing me to the games of "box" and "kitchen

To my Parents

Overview of Thesis:

This Thesis will outline the work that was undertaken throughout the duration of a Research Masters in the Experimental Physics Department NUI Maynooth. The work on the masters started in October 2010. It was at this time that the author joined the THz group under the guidance of Dr. Marcin Gradziel. This group is heavily involved in the design and analysis of sub–millimetre wave optics systems.

In recent times there has been intense interest in developing THz scanner units for the scanning of objects and people. The purpose of these scanners is to exploit the unique properties of the THz sub-section of the electromagnetic spectrum. Many scanners have been developed for application in this region however no publications to date utilise the approach attempted in this thesis. This is to be achieved by utilising two computer controlled tilting mirrors. The goal is to scan a target by tilting a focused electromagnetic radiation beam from a source to a spot on the target by reflecting the beam off two mirrors.

In this thesis the author will discuss in more detail the mechanisms of the system and how this was achieved. The author will also discuss existing scanning methods and hence the motivation behind the development of a scanner of this type. The unique properties and applications that make this particular region of the electromagnetic spectrum of interest are also described.

The comparatively long wavelength of sub–millimetre electromagnetic waves renders the traditional techniques used for analysing optical systems in the visible wavelength ineffective. As a result a range of methods have been developed over the years for analysing these so called "quasi–optical" systems. The author will discuss the theory behind some of these techniques that were utilised during the design and analysis stage of the development of this scanner along with the results of the modelling process.

The development of the experimental setup of the prototype is also outlined and results documented.

1 Chapter 1

Introduction

1.1 The Terahertz Spectrum

In nature it is very easy to see the variation in the behaviour of light of different wavelengths and its interaction with the world around us, from something as simple as the reflection of light by a mirror to the formation of an interference pattern by shining monochromatic light through a diffraction grating. Electromagnetic (EM) radiation is subject to a broad range of phenomenon through its interaction with matter. The position of a certain form of radiation on the EM spectrum is determined by the wavelength λ of the radiation (which is directly related to its frequency f). The part of the EM spectrum that this thesis is concerned with is known as the terahertz region. It is sandwiched between the microwave and infrared region of the EM spectrum (and encompasses the Far IR region) as shown in Figure 1-1 below. The gap spans from radiation of $\lambda = 0.03$ mm to $\lambda = 3$mm.
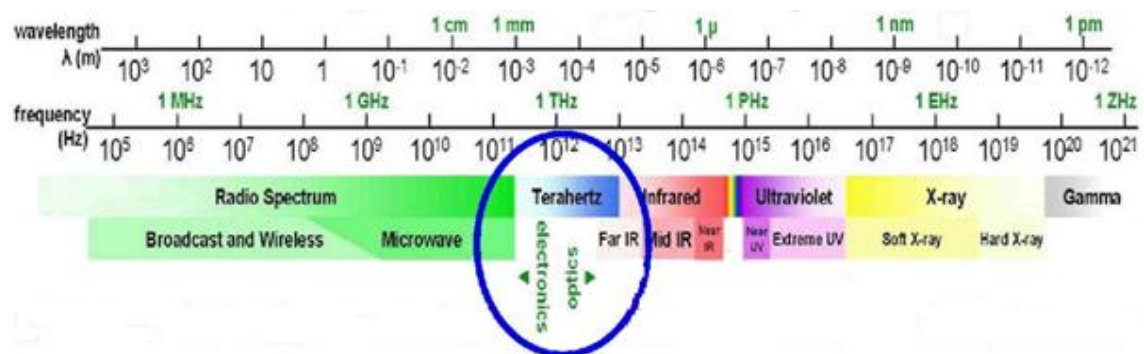
Figure 1-1: The Electromagnetic spectrum. (1)

The Terahertz region is the last accessible part of the EM spectrum to be fully exploited. The relative difficulty in producing Terahertz sources and components in comparison with X–Rays for example has led to the region being somewhat neglected until recently. The region became known as the "Terahertz gap" for many years due to lack of efficient sources and detectors, and research into it. In recent years however there has been a massive increase in development into the region driven not only by

technological advances in the area, but also by the unique properties of radiation of at these wavelengths which have applications in areas as diverse as biomedical imaging, quality control and security.

Most scientists are familiar with geometrical optics which deals with radiation in the limit that the wavelength $\lambda \rightarrow 0$. Geometrical optics provides rigorous and complete methods for analysing optical systems where the dimensions of the optical components (lenses etc) are large enough to neglect the finite wavelength of the radiation. (2) In other situations where λ is comparable to component dimensions, for example when dealing with microwaves, diffraction effects dominate. The Terahertz region lies somewhere between these two limiting cases, where the system involves a beam of radiation (which is propagating through free space) whose diameter is only moderately large when measured in wavelengths compared to dimensions of the components in the system. In this situation procedures that work well for short wavelengths (ray tracing etc) become inaccurate and other methods such as physical optics become extremely computationally time consuming. This allows the theory of Gaussian Beam Mode Analysis to be employed as an effective tool. This formalism includes the effects of diffraction within certain limits. (2)

It can be said that that THz / mm-wave radiation is where optics crosses over into electromagnetism. The development of Terahertz radiation in recent years has borrowed heavily from optical studies and methods behind the analysis of both long and short wavelength radiation without any need to reinvent existing ideas relating to the manipulation and measurement of radiation.

There is no strict definition of the limits of the Terahertz / mm – wave and so the terms are often used interchangeably. The Terahertz region is generally considered to be from 300 GHz – 3 THz. Although the frequencies encountered in the content of this work are generally centered around 100 GHz, outside the limits of the commonly accepted classification, we shall still use Terahertz to include this frequency. This is permissible as radiation at these wavelengths has the same properties as radiation in the commonly accepted THz range e.g. absorption in water is strong while absorption in dielectrics is weak. (3)

1.2   Applications of Terahertz Radiation

As discussed above there has been a surge of development recently in the Terahertz region mainly due to the development of reliable and accurate sources and detectors. The driving force behind the development of these devices was a need to develop sources and detectors for observations of the universe. The technology developed for Terahertz astronomical observations could be then applied to other applications. Terahertz radiation is of great interest to astronomers because of its unique properties. At far–infrared wavelengths dust and gas become transparent to the radiation, this enables astronomers to probe deep inside star forming regions in Galaxy's that would be obscured at optical wavelengths. (4)

The fact that the universe has cooled to just below 3 Kelvin means that the Cosmic Microwave Background (CMB) emits its radiation at the far infra - red region of the EM spectrum. (4) This makes these wavelengths ideal for studying fluctuations in the CMB. Measurements of this type are currently ongoing with the ESA Planck Surveyor whose mission aim is to map the CMB in more detail than previous missions. (5)

One of the main properties of radiation at this wavelength is that water attenuates its propagation very efficiently. As a result most astronomical observations have to be made outside the Earth's atmosphere due to its water content. However there are "propagation windows" at specific wavelengths namely 35, 94, 140 and 220 GHz allowing ground based observations. (6) There is currently amazing research into exploiting these propagation windows (where the attenuation of air and fog is also modest) for the application of remote sensing. This may allow for the application of terahertz for the imaging of objects and land masses where they would otherwise be shrouded by fog or clouds as shown in Figure 1-2 and Figure 1-3 below. (7)
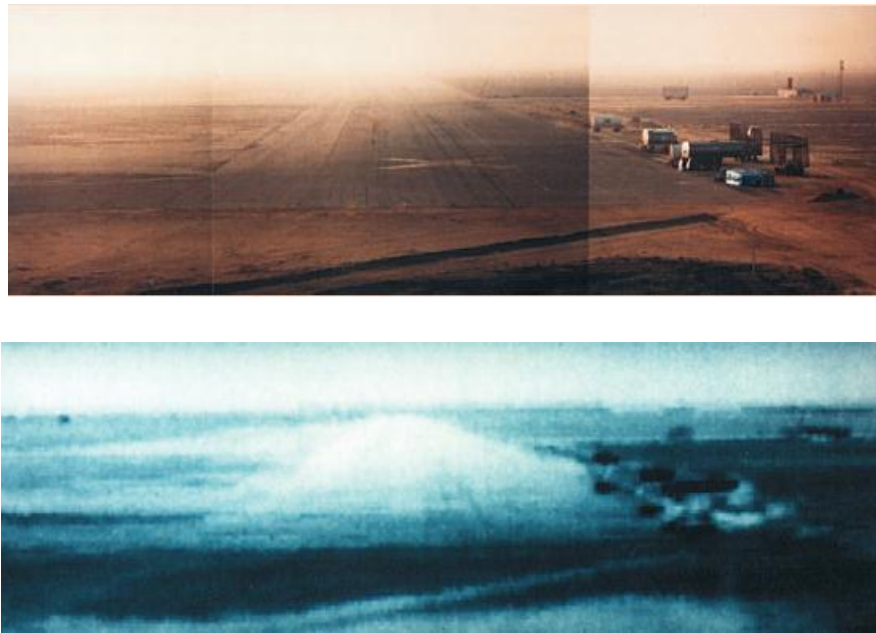
Figure 1-2: Image of an airfield taken at visible wavelengths (top). Terahertz image of the same airfield taken at 94 GHz (bottom) (6).
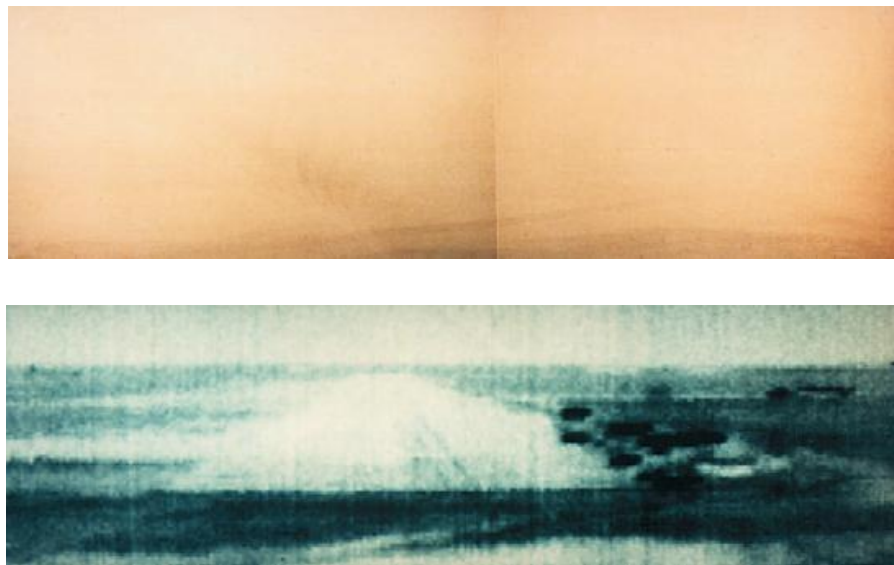
Figure 1-3: Airfield covered in thick fog (top). A Terahertz image of the same airfield where the runway and terrain can clearly be seen taken at 94GHz (bottom) (6).

Over the past few years there has been an increased interest in the potential of THz detection for imaging of weapons and explosives concealed on the person or in baggage. There are three main properties of THz radiation contributing to this interest: (8)

1) Terahertz radiation is readily transmitted through most non-metallic materials, thus enabling THz systems to "see through" concealing barriers such as

packaging, corrugated cardboard, clothing, etc. in order to probe the potentially dangerous materials concealed within.

2) Many materials of interest for security applications including explosives, chemical agents and biological agents have characteristic THz spectra that can be used to fingerprint and thereby identify these concealed materials. (8)

3) Terahertz radiation poses either no or minimal health risk to either a suspect being scanned by a THz system or the systems operator (8), as photon energies are low and therefore non-ionising.

One area of research involves not only the scanning of objects for concealed threats but also the characterisation of these threats. For example since each explosive or chemical agent has a unique spectral fingerprint in the THz spectrum it should be possible not only to determine if an object is an explosive but also the explosive type (TNT, ammonium nitrate etc) as illustrated in Figure 1-4. This could also prove useful if drugs were detected in a package in determining whether they were illicit or legal.
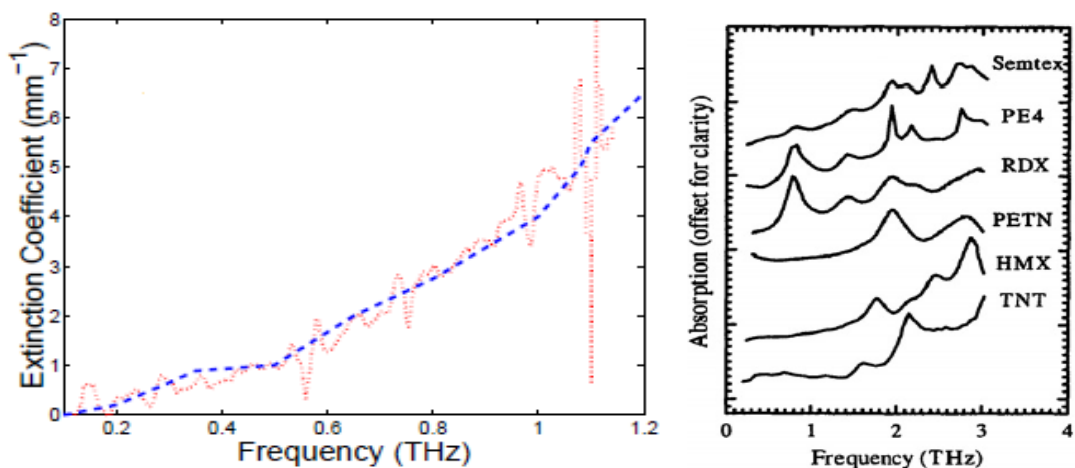
Figure 1-4 – dotted line is measured data of 1mm thick ammonium nitrate sample, dashed line is known absorption spectrum for ammonium nitrate and dashed is measured spectrum. The discrepancy in the data is due to the fact that the measured plot is limited by sampling and sensitivity of the measurement. (9) Examples of absorption spectra of various types of explosive (right). (9)

There has also been considerable focus on the development of scanners to detect the presence of concealed weapons, with some scanners being implemented on a trial basis at some train stations and airports in America. The radiation can penetrate clothes to reveal concealed weapons and can also detect non-metallic objects that would be missed by metal detectors such as ceramic knives etc. (4)
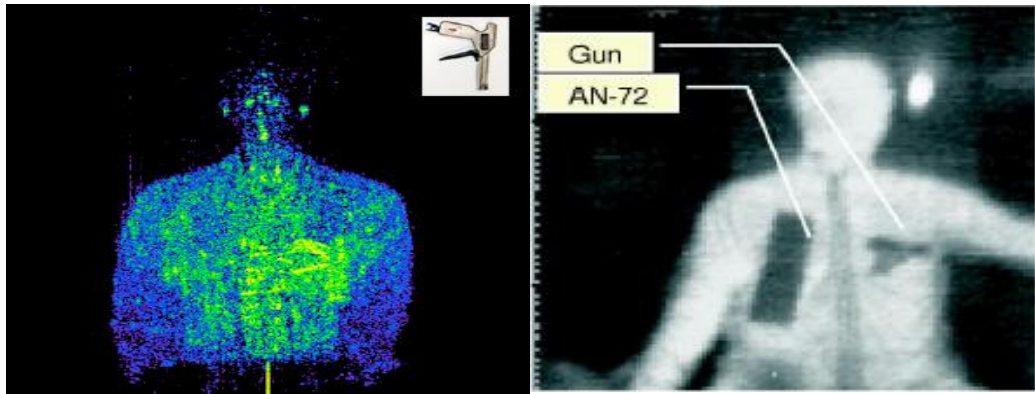
Figure 1-5: Active image of person with gun in left pocket taken at 350GHz (left). (9) Passive imaging with centre frequency at approximately 450GHz (right). (10)

Figure 1-5 shows images of people taken with THz radiation. The images are taken using two different processes as discussed by Federici and Dickinson (11) & (10).

There are also applications of Terahertz radiation in the biomedical sector. Since this type of radiation has relatively low energies ($E \approx 1.2$ meV @ 300 GHz) compared with some other types of radiation it is suitable for use on patients because it is non - ionizing. The dangers of X–Ray imaging is well publicised in that patients can only be exposed to a certain amount of the radiation within a certain period of time etc. With so called T–Rays these problems are eliminated however the high absorption of radiation at these wavelengths by moisture means that more invasive imaging similar to the capabilities of X–rays are not possible due to the radiation being absorbed within the first few millimetres of skin. Figure 1-6 below contains an image of a tooth that was imaged using a specific imaging technique called Terahertz Pulsed Imaging (TPI) which involves imaging using picoseconds pulses rather than continuous wave sources. Cavities in the tooth can be clearly seen in one image and the enamel and dentine can be seen in the second image. (12)
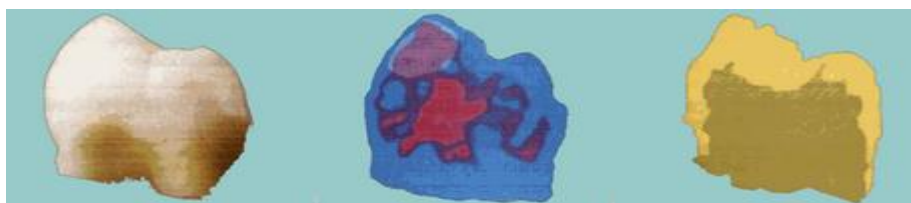
Figure 1-6: Human tooth (Left), THz image of the tooth reveals cavities in red (Centre), Time of flight THz data show enamel and dentine in tooth (Right).

Research done at the Penn-State electro optics group illustrates the use of Terahertz Pulsed Imaging (TPI) for use in the biomedical sector. With TPI time delayed THz pulses are stacked to form an image, this technique provides very fine resolution. (13) Below (left) is an image of a piece of chicken burnt with a hot piece of metal (threaded screw at 300 ℃). Although the burn is covered with a bandage a THz image of the burn can be retrieved. TPI is especially useful for investigating the depth of wounds as demonstrated below (right) where a 2D image of the extent of the wound can be seen. (13)
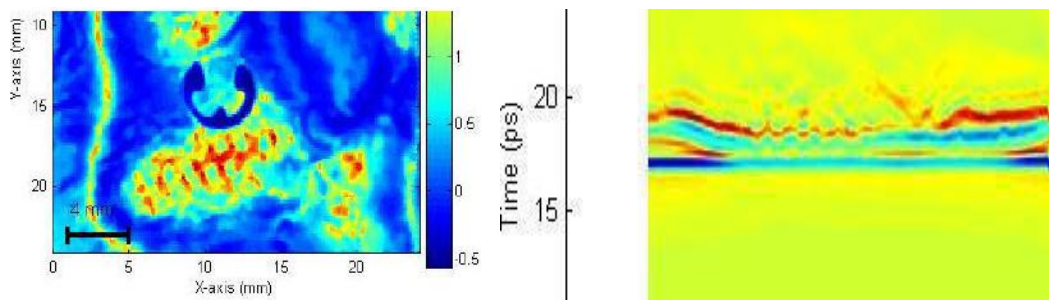
Figure 1-7: *Image of burn wound ($f = 1.5\ THz$) covered with bandage (left) and z-axis time cut through the thickness (right).*

Although THz radiation is heavily absorbed by the water content in human skin, there are still applications for near surface applications. Surface cancers for example make up roughly 80% of all cancers (5) and due to their varying level of water content compared with normal tissue, a THz scan has the potential to detect such growths. Also the fact that a healing wound has different levels of water content at different stages of the healing process has the potential to allow a doctor to investigate the progress of a wound without removing bandages.

1.3   Various types of scanning methods

1.3.1 "One shot" THz imaging

With this method the aim is to replicate the operation of a digital camera at optical wavelengths where each point on a target is imaged by a corresponding pixel on a Charged Coupled Device (CCD). So for a THz image of an object to be obtained at these wavelengths, radiation from a point on the target needs to be focused to a detector in an array of detectors in such a way that each point on the object has its own

corresponding detector as illustrated in Figure 1-8. In this way each point on the target can be imaged simultaneously creating images with a single measurement. This is by far the fastest method of imaging, however, due to problems with the integration and sensitivity of the detectors the technology for this method is still in its infancy at Terahertz wavelengths.
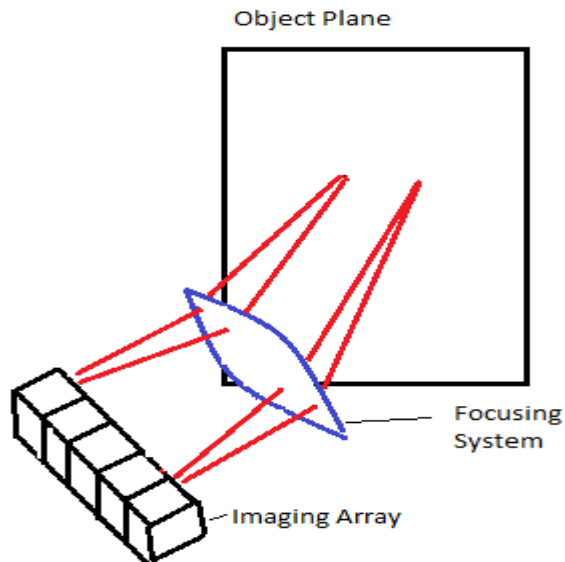
Figure 1-8: Schematic diagram illustrating the mechanisms of imaging using an array of detectors.

1.3.2 Single Pixel detection

A more commonly used process for imaging is to use a single pixel detector and to image a target on a point by point basis either by having adaptive optics to focus the radiation from different points onto a stationary detector as illustrated in Figure 1-9 or by moving the detector around so that it is receiving radiation from a certain point of interest on the object. Although this method is a lot more cost efficient than the "One shot" method it is at the expense of the time it takes to form an image as the target has to be imaged on a point by point basis. The main advantage of this method is that the technology needed is currently in existence.
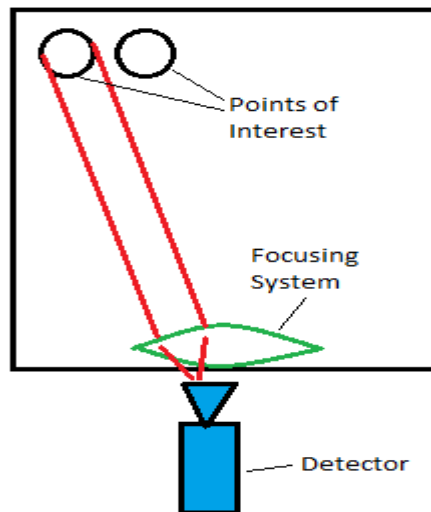
Figure 1-9: Schematic diagram illustrating the concept of imaging using a single pixel detector.

For example the main scanner currently in operation in the Experimental Physics department NUI Maynooth operates using a single transmitter detector pair (two converter heads connected to a Vector Network Analyser (VNA). Using this method the transmitter or detector head is scanned over the target area on a point by point basis so that information such as the phase and magnitude of the reflected radiation can be stored for each point on the target. The scan is carried out in such a way that one converter head remains in a fixed position and the other moves in a raster pattern as illustrated in Figure 1-10.
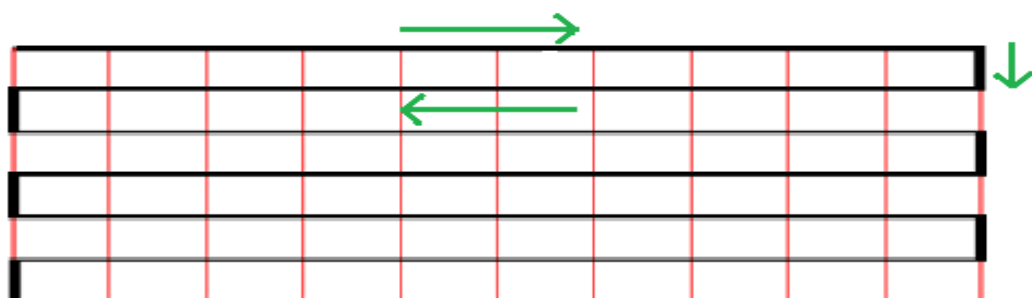
Figure 1-10: Illustration of path taken of converter head moving in a raster pattern as radiation detected on a point by point basis.

The object is illuminated by the stationary head and the reception pattern is focused on to a small detector beam, then, the reflection and transmission parameters are

recorded on a point by point basis. An image of the object can then be formed where a point on a scan represents a pixel on an image as illustrated in Figure 1-11.
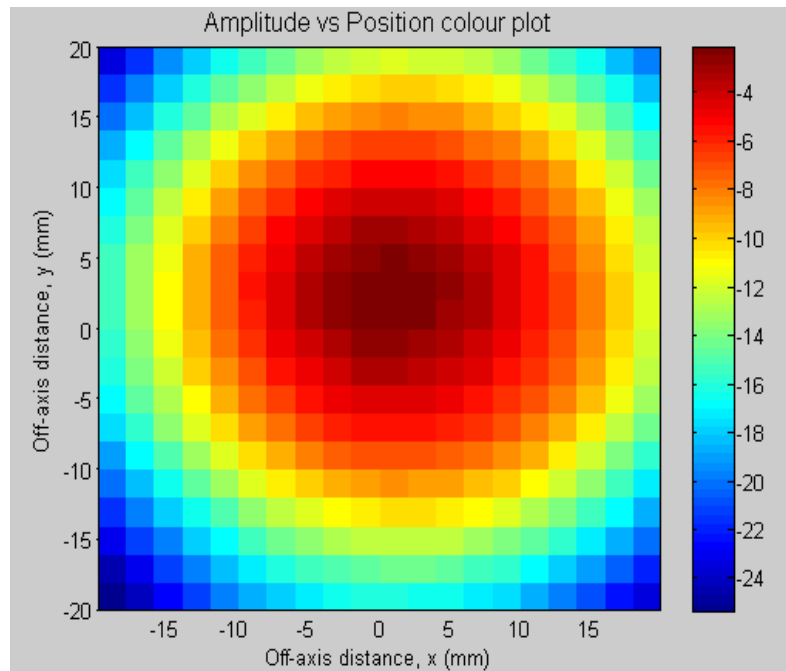
Figure 1-11: Example of raster scanner image obtained from in house scanner, capturing image of beam refocused through a Fresnel lens. Each square on the image is a measured point with fraction of total loss being measure in decibels. This scan took roughly 20 minutes to complete.

1.3.3 Active and passive Imaging

There are two main types of imaging, passive and active. With passive imaging it is the ambient THz radiation that is emitted by every object and person (essentially thermal radiation) that is detected to form an image. The difficulty with this method is that extremely sensitive detectors are required to detect the low levels of radiation being emitted. With active imaging the object of interest is illuminated with an external THz source in such a way that it provides spatial information about the target, this process is similar to the operation of a flash on a standard digital camera. Active imaging can be subdivided into reflective and transmission imaging. In transmission imaging the radiation is detected after being transmitted through the target, in reflective imaging the detector is placed in such a way as to receive the reflected radiation from the target.

1.3.4 Electro – Optic Imaging

With this technique THz images are shifted into visible light so that a CCD can be used to store the image. This method is a lot faster than the two previous methods however the trade-off is at the expense of low dynamic range, and also, low reflecting objects cannot be imaged due to a lack of sensitivity. (4)

1.4 Approach to be used in this project

1.4.1 Integrated active imaging system

The design for the scanner developed for this project is an active imaging system and is a variation of the "single pixel" method described in section 1.3.2 above. The system will have a single transmitter and receiver module which will illuminate the object with THz radiation in such a way that the reflected radiation will be picked up by the detecting component.
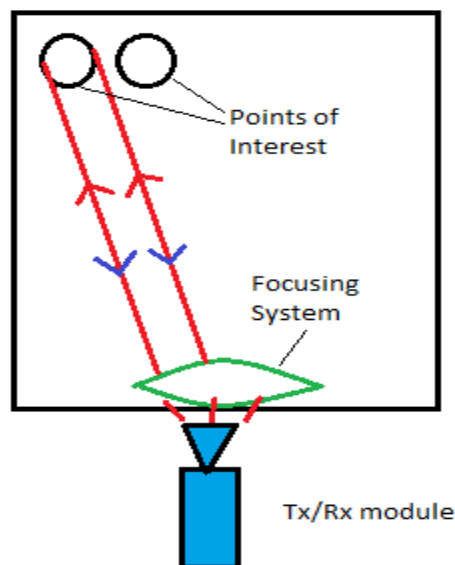
Figure 1-12: Schematic representation of the active imaging system used

Traditionally active imaging is implemented by having a separate radiation source illuminating the target and either a moving stand-alone detector or a stationary detector for detection of radiation. The method being used here is a somewhat novel approach in that it uses a single module for the transmission and detection of the

radiation. The transmitter / receiver module (Tx/Rx module) will be stationary so an adaptive optics system is needed to point the transmitted beam to a point of interest on the target and to point the reflected beam for that point back onto the detector. The module will transmit and receive along essentially the same optical path.

1.4.2 Tilting mirror approach

As discussed above, using the integrated active imaging approach there was a need for some kind of adaptive optics for pointing the beam of radiation from the stationary transmitter to the point of interest on the target, and back again. It was decided to try and achieve this using a pair of plane mirrors which can be tilted around an axis as illustrated in Figure 1-13. The idea was to tilt the beam of radiation from the source using the mirrors. One mirror was placed in a position so as to tilt the beam in a vertical motion and the second to tilt the beam in a horizontal motion. Additional optics components were needed to focus the radiation from the source to the mirrors and from the mirrors onto a point on the screen.
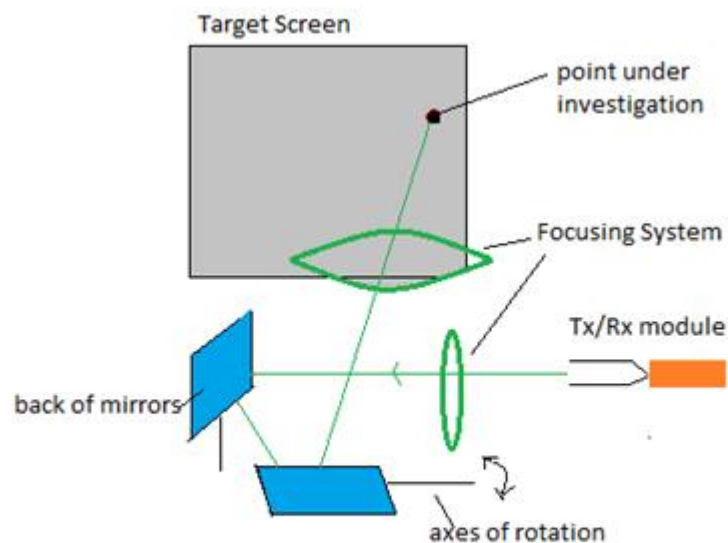
Figure 1-13: Schematic representation of how the use of two mirrors will be employed to tilt the beam of radiation at a particular point on a target under study. The mirror on the left will control the horizontal motion of the beam across the target and the second mirror will control the vertical movement.

The mirrors were to be computer controlled so that a high degree of accuracy could be achieved when positioning the mirrors at a desired orientation, and the whole measurement could be completely automated.

As the beam is tilted in different orientations it inevitably interacts with the focusing elements in such a way that the beam is distorted as it scans across the image due to aberrational effects. As a result it was envisaged that post processing of the data received from a scan would be necessary to retrieve and accurately image the target. To this end it was predicted that it would be necessary to develop an understanding of the beam and power at the target by modelling the system for various tilt orientations. It was also envisaged that it would be possible to design the optics in such a way as to allow post processing of the data obtained from a scan to increase the resolution of an image. To achieve this it was necessary to not only have a well understood beam throughout the system and at the target plane but also essential the beam at the target be fairly wide ($\approx 15mm$). The concept behind this post processing technique and the reasoning behind the requirements are discussed in more detail in Chapter 5.

1.5   Summary

In this chapter the nature of sub-mm wave radiation was introduced to the reader along with the associated properties which distinguish it from other forms of radiation in the electromagnetic spectrum. A brief introduction into the effects of diffraction at these wavelengths and hence the need for novel propagation techniques such as Gaussian Beam Mode Analysis, for accurate but yet not computationally time consuming analysis was also outlined.

An introduction into the various interesting properties of THz radiation and how these properties can be utilised for applications within modern society was also discussed, with particular reference to the space, security, biomedical and aerospace industries. This led to a discussion of some of the various types of scanning systems currently in existence and the advantages and disadvantages of each method.

Next the approach that was utilised in this project was outlined, in that the system was to be an active imaging system with a single pixel detector. The system would incorporate a transmitter and receiver module for the purposes of imaging and the

transmitted and received radiation would travel along the same optical path. It was determined that the imaging was to be achieved by tilting a beam of radiation to a desired point under investigation by utilising two tilting mirrors.

Finally the need for a well understood beam throughout the system for the purpose of post processing of the data was outlined. It was established that it was necessary to perform post processing of the data to account for aberrations due to varying beam tilt orientations and for the purpose of increasing the resolution of scans. It was also established that a minimum beam width requirement of $\approx 15\ mm$ be placed on the width of the beam at the output plane.

2   Chapter 2

Development of theory, and tools used to model quasi-optical systems

2.1   Introduction

In this chapter the nature of sub-mm wave radiation and hence the theory of the propagation techniques used for modelling optical systems at these wavelengths is discussed. Analysis on some simple systems that were investigated using the different techniques will also be discussed to compare the strengths and weaknesses of each method. It is perhaps apt to start with a short discussion of what exactly quasi-optics is and give a brief introduction to each of the methods used in this research project.

When designing sub-millimetre wave systems the main aim is to couple the radiation from the source to the detector as efficiently as possible. At these frequencies the radiation is often propagated as a beam through free space. Unlike optical propagation in the visible spectrum for example the collimated beam is a few wavelengths in diameter, meaning that diffraction effects cannot be completely neglected meaning that traditional techniques such as ray tracing become inadequate at comprehensively modelling the system. These types of systems are called quasi-optical systems as the diffraction effects do not completely dominate. (2)

With physical optics it is possible to address these situations comprehensively using Maxwell's equations however these calculations can be extremely computationally time consuming. To reduce demands on memory and processing power, a scalar representation of the field is often used. This scalar field amplitude is associated with the electric field vector E and is represented by a single complex scalar. (5) This treatment gives rise to diffraction integrals as a means of solving for electric field values at certain planes etc throughout the system. Although this method uses a Physical Optics approach, the term Physical Optics is usually reserved for the full vector treatment of the problem.

As stated above, when radiation of a relatively long wavelength is propagated through an optical system it is the diffraction effects which dominate, however, when the diffraction is not severe one of the most efficient ways to analyse the propagation is using Gaussian Beam Mode Analysis (GBMA). This serves as a very useful tool for investigating systems with a sufficient accuracy however with a great reduction in computation time.

Three main analysis techniques were involved during the development of this project, these being Gaussian Beam Mode Analysis, Scalar diffraction and Physical Optics. The following sections will outline these in greater detail.

2.2 Gaussian Beam Mode Analysis

2.2.1 The Paraxial Wave Equation

The theory of Gaussian Beam Modes was developed during the 1960's and this thesis will use the approach outlined in the seminal book Quasi-optical Systems by Goldsmith (2). Other useful sources from which material was drawn are White & Loughran (5) (14).

The first assumption that will be made when dealing with GBMA is that the propagating radiation is largely collimated, that is, it has a well-defined direction of propagation but also has some transverse variation compared to a plane wave which does not. We can thus develop a paraxial wave equation which forms the basis for Gaussian Beam Propagation. We will also assume that the Gaussian beam does not have an infinitesimal point source instead we will assume it expands from a region of finite extent unlike a source in geometrical optics. A single component of electromagnetic radiation, γ propagating in a uniform medium satisfies the Helmholtz wave equation:

$$\nabla^2 \gamma + k^2 \gamma = 0 \tag{2.1}$$

Since γ represents any component of the electric E or magnetic H fields then this equation can equally be written as:

$$\nabla^2 E + k^2 E = 0 \tag{2.2}$$

$$\nabla^2 H + k^2 H = 0 \tag{2.3}$$

In the Helmholtz equation we assume a time variation of the form $e^{i\omega t}$ where ω is the angular frequency, equal to 2πi with i representing the actual frequency and i is $\sqrt{-1}$. The wave number k is equal to $\frac{2\pi}{\lambda}$ where λ is the wavelength, so that the equation for the speed of a wave $c = f\lambda$ can be expressed in the form:

$$c = \frac{\omega}{k} \tag{2.4}$$

We now consider the propagation of a paraxial beam of radiation which is quasi-collimated in the region of a "focus" and spreads out with a small opening angle. In general the electromagnetic wave is transverse locally. For a paraxial beam we assume that the electric and magnetic components of the fields are mutually perpendicular, not just locally but over the full wave front. We will also assume that the components are perpendicular to the dominant axis of propagation of the beam which we call the z-axis. For convenience, we can express any component of the electric field, ignoring time dependence, as

$$E(x,y,z) = \mu(x,y,z)e^{-ikz} \tag{2.5}$$

where μ is a complex scalar function that defines the non-plane wave part of the beam. This turns out to be a useful form for paraxial beams.

Following substitution for $E(x,y,z)$ using Equation 2.5, the Helmholtz equation can then be re-expressed in rectangular coordinates, (x,y,z) as follows:

$$\frac{\partial^2 \mu}{\partial x^2} + \frac{\partial^2 \mu}{\partial y^2} + \frac{\partial^2 \mu}{\partial z^2} - 2ik\frac{\partial \mu}{\partial z} = 0 \tag{2.6}$$

This is called the reduced wave equation, it is accurate but if we make assumptions about the variation of the beam in the z direction then it can be simplified further. By definition the paraxial wave approximation assumes that the variation in μ is small over distances in z comparable to a wavelength, i.e. that

$$\frac{\partial^2 \mu}{\partial z^2} \ll \frac{2\pi}{\lambda}\frac{\partial \mu}{\partial z} \tag{2.7}$$

This means that the third term in equation 2.6 is small compared to the last term. Secondly the paraxial approximation assumes that the variation of μ with z is a lot less than with x and y so that the third term is also small compared to the first two, as must

be the case for a quasi-collimated beam with a small opening angle in the far field. Thus the paraxial wave equation allows us to drop the third term to obtain what is known as the paraxial wave equation:

$$\frac{\partial^2 \mu}{\partial x^2} + \frac{\partial^2 \mu}{\partial y^2} - 2ik\frac{\partial \mu}{\partial z} = 0 \qquad (2.8)$$

The paraxial assumption is considered reasonable and not very restrictive as the equation is considered applicable as long as the angular divergence of the beam is within 30° of the z axis. The equation can also be expressed in cylindrical polar coordinates as:

$$\frac{1}{r}\frac{\partial}{\partial r}\left(\frac{\partial \Psi}{\partial r}\right) + \frac{1}{r^2}\frac{\partial^2 \Psi}{\partial \theta^2} - 2ik\frac{\partial \Psi}{\partial z} = 0 \qquad (2.9)$$

The precise nature of the solutions of these equations for specific systems depends on the symmetry of the system and the coordinate system chosen.

2.2.2 Higher Order Hermite-Gaussian Modes

In the case of using a rectangular coordinate system for higher order modes, the general two dimensional Gaussian Beam mode can be represented by the product of two one-dimensional functions which are solutions to the paraxial wave equation discussed in section 2.2.1. If we initially consider the x coordinate alone, we include an additional x-dependant function H to obtain the higher order modes. A trial solution of the form

$$u(x,z) = A(z)H\left(\frac{\sqrt{2}x}{w(z)}\right)exp\left[-\frac{ikx^2}{2q(z)}\right] \qquad (2.10)$$

is successful assuming w is the width of the radius of the beam and q is the complex beam parameter. This function H satisfies Hermite's differential equation

$$\frac{d^2H(u)}{du^2} - 2u\frac{dH(u)}{du} + 2mH(u) = 0 \qquad (2.11)$$

where m is a positive integer. This is the defining equation for the Hermite polynomial of order m, denoted $H_m(u)$. If n = 0, 1, 2….. Then the solution is given by Rodrigues' formula

$$H_n(u) = (-1)^n e^{u^2}\frac{d^n}{du^n}\left(e^{-u^2}\right) \qquad (2.12)$$

From this the first five Hermite Polynomials are:

$$H_0(u) = 1 \tag{2.13}$$

$$H_1(u) = 2u$$

$$H_2(u) = 4u^2 - 2$$

$$H_3(u) = 8u^3 - 12u$$

$$H_4(u) = 16u^4 - 48u^2 + 12$$

From this the expression for the one dimensional Gaussian beam mode of order m can be shown to be

$$E_m(x,z) = \left(\frac{2}{\pi}\right)^{0.25} \left[\frac{1}{w_x 2^m m!}\right]^{0.5} H_m\left(\frac{\sqrt{2}x}{w_x}\right)$$

$$\cdot \exp\left[-\frac{x^2}{w_x^2} - ikz - \frac{i\pi x^2}{\lambda R_x} + \frac{i(2m+1)\emptyset_{0x}}{2}\right] \tag{2.14}$$

The beam width parameter w and the beam radius of curvature R are mode independent but the beam phase slippage term Ø is mode dependant as it varies for each mode.

In dealing with the two dimensional case, the paraxial wave equation for *u(x,y,z)* separates the appropriate trial solution formed from a product of functions like those in equation 2.14. This gives the ability to deal with high order modes that have unequal beam waist radii and different beam waist locations. Higher order modes in rectangular coordinates obey the orthogonality relationship

$$\iint_{-\infty}^{\infty} E_{mn}(x,y,z) E_{pq}^*(x,y,z) dxdy = \delta_{mp}\delta_{nq} \tag{2.15}$$

One special situation is that in which beams in *x* and *y* with equal beam waist radii are located at the same value of *z*. In this case we obtain

$$E_{mn}(x,y,z) = \left(\frac{1}{\pi w^2 2^{m+n+1} m! n!}\right)^{0.5} H_m\left(\frac{\sqrt{2}x}{w}\right) H_n\left(\frac{\sqrt{2}y}{w}\right)$$

$$\cdot \exp\left[-\frac{(x^2+y^2)}{w^2}\right] - ikz \frac{i\pi(x^2+y^2)}{\lambda R} + i(m+n+1)\emptyset_0. \tag{2.16}$$

The graph below was produced using LabVIEW software developed by the author and shows the fundamental mode (simple Gaussian), and the result of multiplying this pattern by the higher Hermite polynomials for subsequent modes. In general, any paraxial propagating beam must be expressible as a linear sum of Hermite modes since the mode set is complete for this class of beam. From figure 2-1 we note that odd numbered modes are asymmetric about the *x*-axis and so will not contribute any power to symmetric beams. This property of Hermite Gaussian modes is useful when attempting to computationally recreate Electric fields as the modes which contribute no power can be omitted from the modelling process.

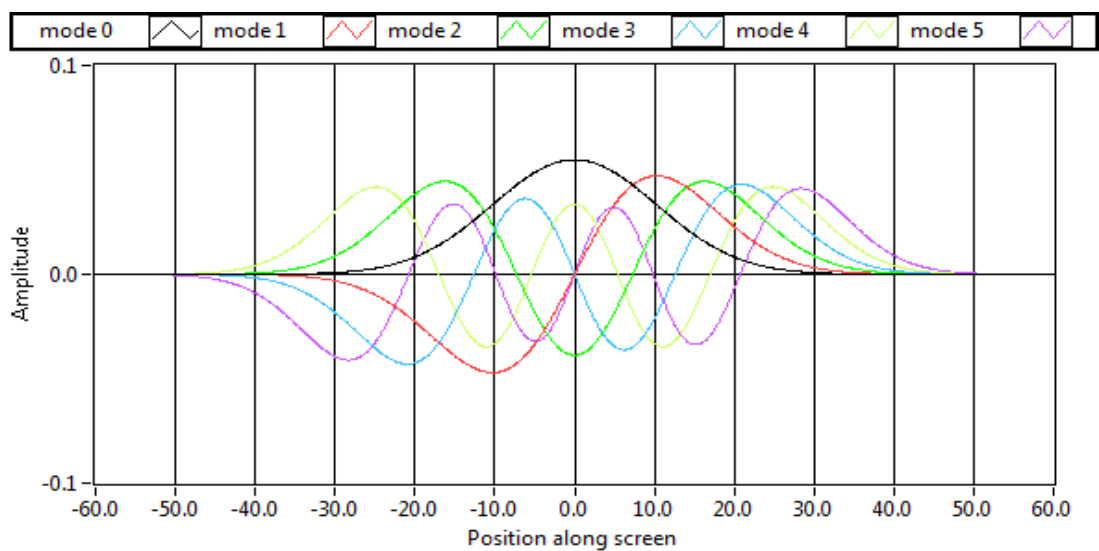*Figure 2-1: Plot of the first six Hermite Gaussian modes. It is clear that the odd numbered modes are asymmetric.*
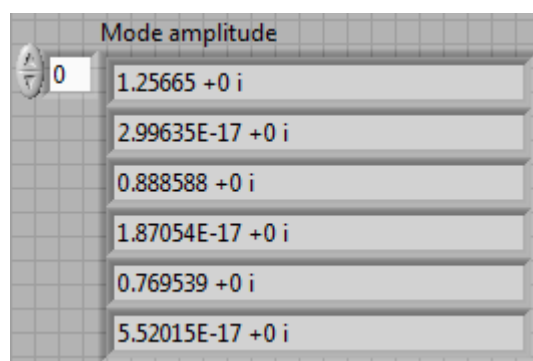

Figure 2-2: Amplitude values for each mode, illustrating that odd numbered modes have a negligible contribution to the field.

As stated above, the Hermite Gaussian modes described above form a basis set to describe any beam of interest. A useful approach for modelling certain classic beam

surfaces is to combine the modes as a linear sum to form a top hat or Bessel beam as will be discussed in more detail later. As each mode propagates through space from a source it keeps its basic shape, however, it may broaden or flatten with increasing propagation distance. The linear sum of modes does however change its form, for example with the case of a top hat it will change to a sinc pattern in the 1D case. This will be illustrated in more detail later.

2.2.3 Characterisation of the Fundamental Gaussian Beam Mode

For a full understanding of Gaussian Beam Modes it is essential to understand how they change as they propagate along the axis of a system. As discussed in section 2.2.2, the fundamental mode of the Hermite Mode set has a simple Gaussian profile. Since this fundamental mode has such a simple shape it becomes increasingly useful when designing optical systems as predictions about the beam can be used to position optical elements throughout a system in order to get a desired beam profile at a desired point in the system.

The beam waist radius or beam width is essentially the distance r from the propagation axis to the location where the field drops to $\frac{1}{e}$ of its maximum value or similarly where the intensity of the beam drops to e^{-2} of its maximum.
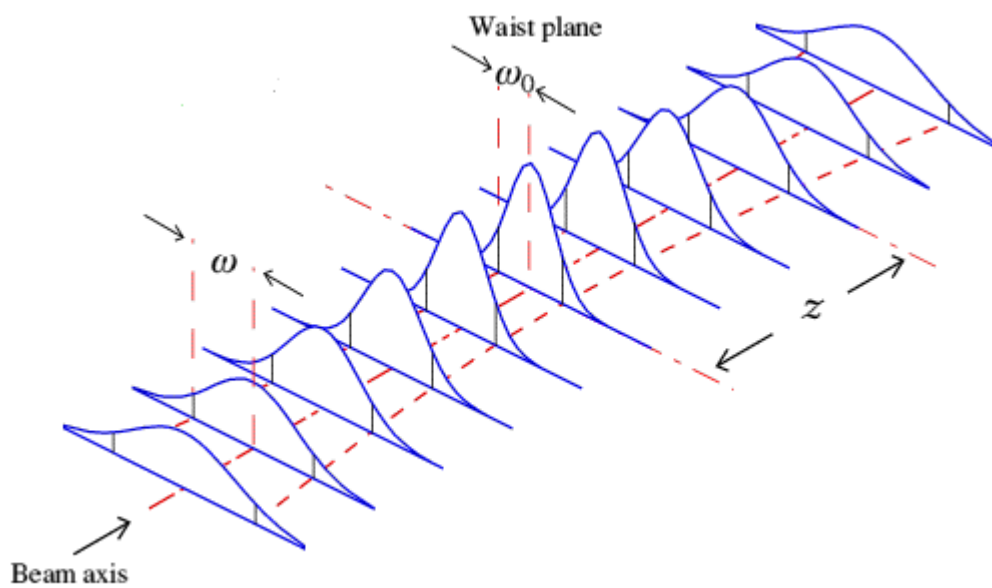

Figure 2-3: Illustration of propagation of fundamental Gaussian Beam.

The beam width radius varies as a function of propagation distance z as determined by the following equation (2)

$$W(z)^2 = W_0{}^2 \left[1 + \frac{z\lambda}{\pi W_0{}^2}\right] \qquad (2.17)$$

where λ is the wavelength of the radiation. The W_0 term denotes the position of the beam waist. The beam waist is essentially the quasi-optical equivalent of a focus in geometrical optics, where the beam reaches its minimum width. These beam waist positions can be achieved by using focusing elements such as mirrors or lenses, beam waist positions also occur inside some sub-mm wave sources such as corrugated feed horns.

The next parameter of importance with respect to the propagation of a fundamental mode is a term called the radius of curvature which gives the curvature of regions of equal phase. At the waist of a beam the radius of curvature is infinite i.e. the beam looks like a plane wave. As the mode propagates through a distance z from the waist the curvature of the beam is given by the following expression.

$$R(z) = z \left[1 + \left(\frac{\pi W_0{}^2}{\lambda z}\right)\right]^2 \qquad (2.18)$$
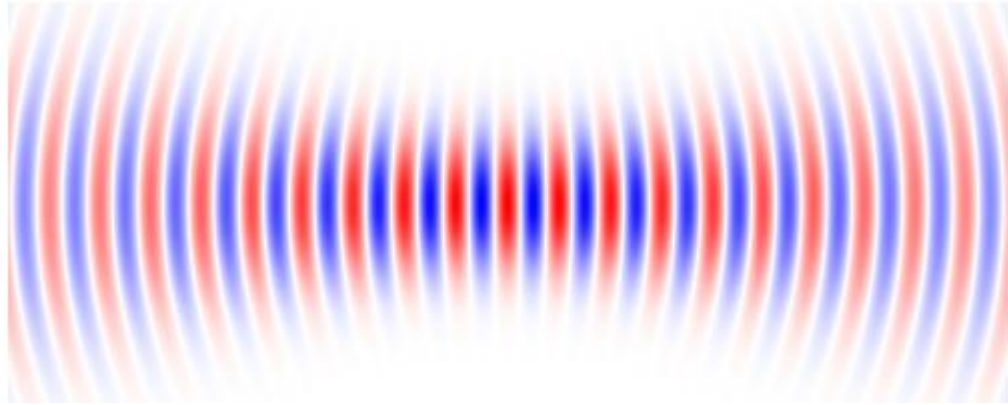

Figure 2-4: Illustration of radius of curvature of a beam. (15)

It is clear that for large values of z, R approaches z, meaning that the beam becomes spherical in the far field, it follows that the radius of curvature has a minimum value known as the confocal distance and can be determined from *(15)*

$$z_c = \frac{\pi w_0^2}{\lambda}. \qquad (2.19)$$

The phase of a mode depends heavily on the radius of curvature of a beam as described above, but for a full analysis of the phase another term known as the phase slippage term has to be taken into account. This phase slippage term is mode dependant and in fact it is the term which causes the mode to evolve with distance a phenomenon usually attributed to diffraction. (16) The phase slippage term for a mode is represented by the following expression:

$$\phi_0 = arc\,tan\left(\frac{\lambda z}{\pi W_0{}^2}\right) \tag{2.20}$$

2.2.4 Modelling Electric fields using Gaussian Beam Mode Analysis

As discussed before Gaussian Beam Modes prove a useful tool when attempting to model the Electric field distributions of quasi-optical systems, as it provides a computationally quick method for a first approximation. In this approach the complex scalar field E, representing one of the transverse components of the fields is written as a sum of modes (16)

$$E = \sum_n A_n \Psi_n \tag{2.21}$$

Where E is the electric field, n is the mode number, Ψ is the mode and A is a term called the mode coefficient which effectively scales what part of the mode makes a contribution to the overall field.

To demonstrate this principle we will consider the situation of an aperture with a plane wave incident on it. The aim will be to calculate the E-field at a plane set at a certain distance from the aperture. The first step in the process is to recreate the E-field at the aperture which is achieved by summing the individual modes together. Then the aperture can be used to create the mode coefficient for each individual mode. This is done by assuming that the areas outside the aperture boundaries are completely opaque. Hence the E field within the boundaries can be calculated to be $E_0\exp(-ikz)$ (16) (where E_0 is the value of the incident source field), and the value of the E field outside the aperture boundaries can be assumed to be zero. The value of the mode coefficients for each mode can then be calculated by integrating across the aperture plane as follows, where E^* is the field at the aperture plane

$$A_n = \int_{-\infty}^{\infty} E^* \Psi_n dx \tag{2.22}$$

24

When the mode coefficient is known it is then possible to calculate the E field at the aperture using equation 2.21 above. To obtain a profile of the E field at the output plane then we simply propagate the modes using the rules for mode propagation as outlined in section 2.2.3, scale each mode by its mode coefficient again and sum all the modes to obtain the output Electric field pattern (again using equation 2.21). As the number of modes used in the model increases so does the accuracy of the result. This is illustrated in Figure 2-5.

A LabVIEW program was written by the author for analysing the situation described above. Theory suggested that a for the 1D case a top hat structure would be found when the screen is placed at the aperture and would evolve into a sinc pattern when the screen is placed further from the aperture.
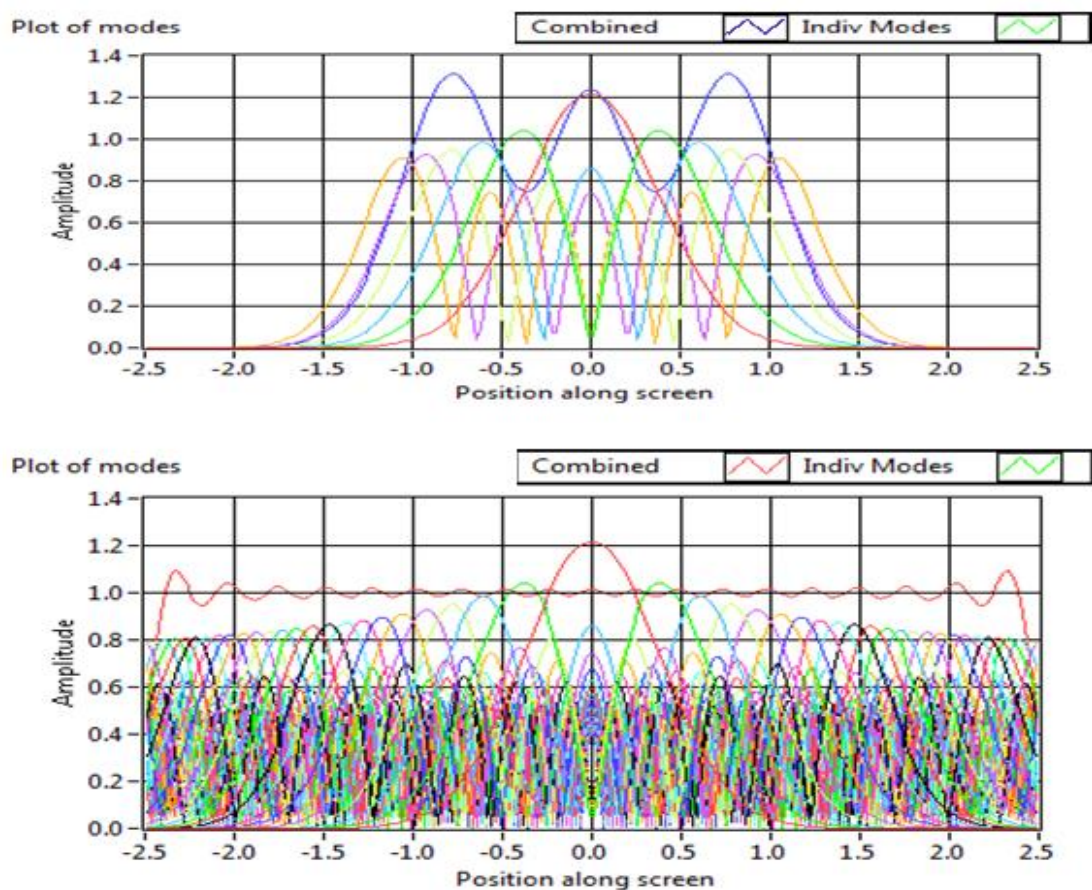
Figure 2-5: Reconstruction of field at aperture using a low number of modes (6 modes) (top) and a high number of modes (50 modes) (bottom). The aperture was set to be 5mm wide and the wavelength set to 1mm in this case.

From inspection of the plots of the field at the aperture above it is clear how the number of modes used affects the accuracy of the representation of the E-field. When

25

a small number of modes are used the modelled field is not a top hat which fills the 5 mm wide aperture. By using a higher number of modes the pattern is more representative of the field, however, is still not a perfect top hat structure. Only using an infinite number of modes (or a more accurate modelling method) will achieve this. So to summarise although computationally fast GBMA is not as accurate as other modelling techniques. However it does provide a fast and reliable method for a first evaluation of an optical system at the design stage.

Figure 2-6: Reconstruction of field at aperture (3 mm) (top) and at a distance of 100 mm from aperture. Intensity is plotted as a function of position along screen by sample number. It should be noted that in the second scenario the screen is a lot wider.

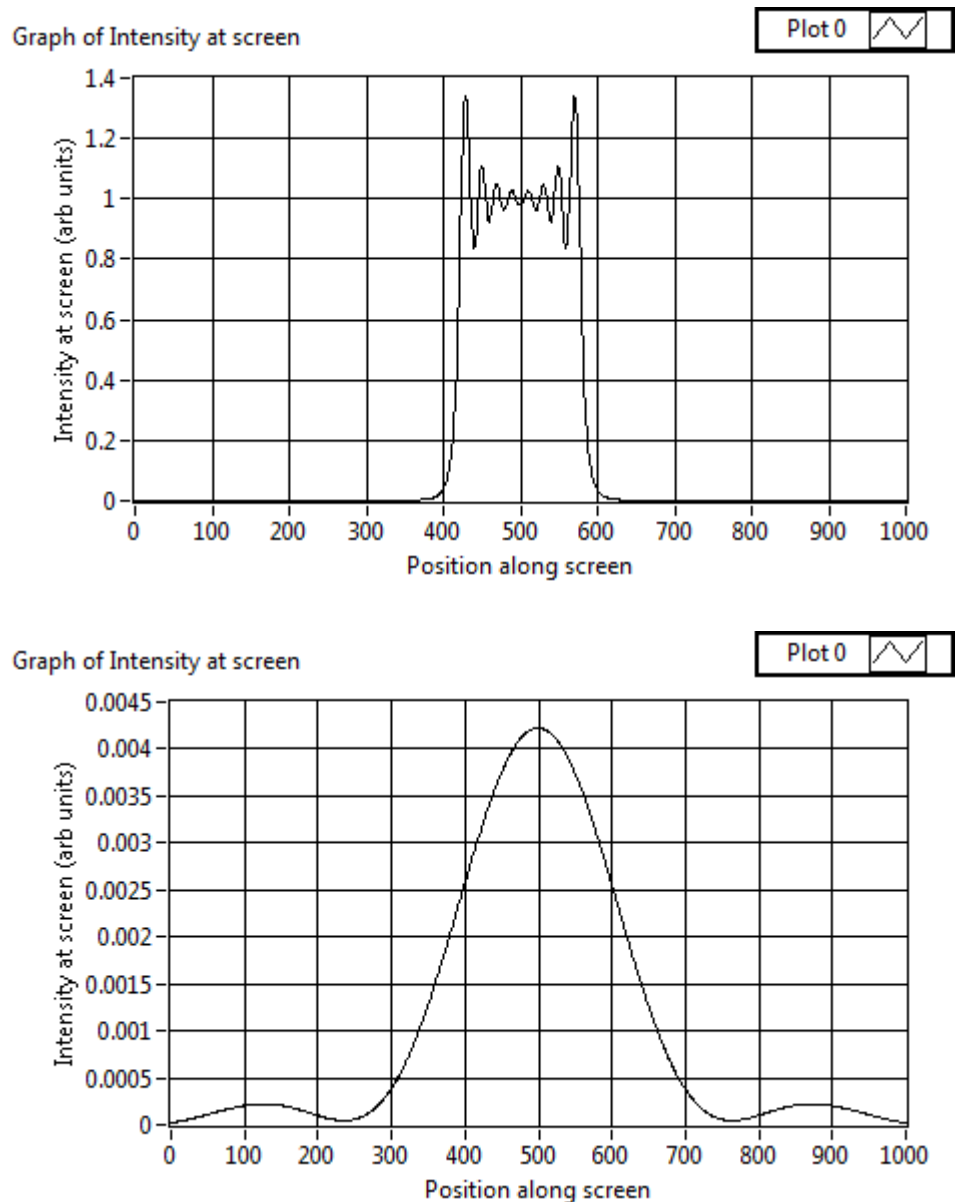From the plots in Figure 2-6 it can be clearly seen how the field evolves to a sinc pattern in the far-field as predicted by theory. It should be noted that although the screen in the second scenario is a lot wider the integrated power is the same.

In order to create a realistic Electric field pattern at an aperture the modes being used have to "fit" the aperture. This implies that for a given aperture there is going to be an optimum beam width for producing an accurate representation of the field. Code was written by the author to allow the investigation of this process. For a defined number of modes the program started at a small beam width (initially .01mm), calculates the power increases the width slightly then repeats the procedure. The program was then run for varying numbers of modes but using the same beam widths for each mode set. The width of the aperture was defined to be 5mm.
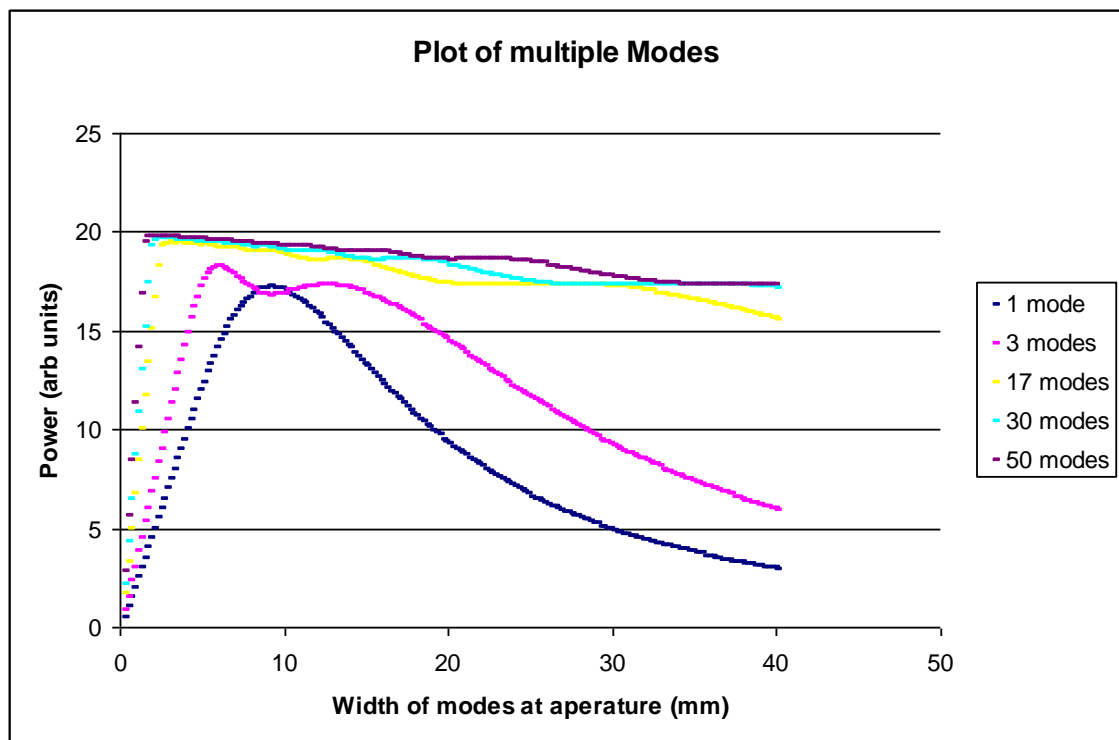
Figure 2-7: Plot of power in modes as a function of mode width at aperture.

It can be seen in Figure 2-7 that when a low number of modes is used the choice of mode width at the aperture has to be quite exact as a couple of millimetres either side of the peak leads to significant power loss. As the number of modes increase the graph plateaus indicating that the choice of beam width does not have to be quite as exact. It can also be seen from the graph that for increasing mode numbers the optimum mode width shifts to lower values.

2.2.5 Ray Transfer Matrices

A quick and effective way of analysing an optical system is to use Ray transfer matrices. Consider a situation where we have a spherical wave with a certain radius of curvature expanding. This wave can be thought of as a collection of rays expanding from a point surface. A ray can be defined by x, the off axis distance of the ray and y, the angle between the ray and the principle axis of the system. If an input ray of a certain x_{in} and y_{in} is incident on an optical element in a system the corresponding output ray in terms of x_{out} and y_{out} can be determined from (2)

$$\begin{pmatrix} x_{out} \\ y_{out} \end{pmatrix} = \begin{pmatrix} A & B \\ C & D \end{pmatrix} \begin{pmatrix} x_{in} \\ y_{in} \end{pmatrix} \qquad (2.23)$$

where the ABCD matrix represents the focusing properties of the optical element in question as illustrated in Figure 2-8.
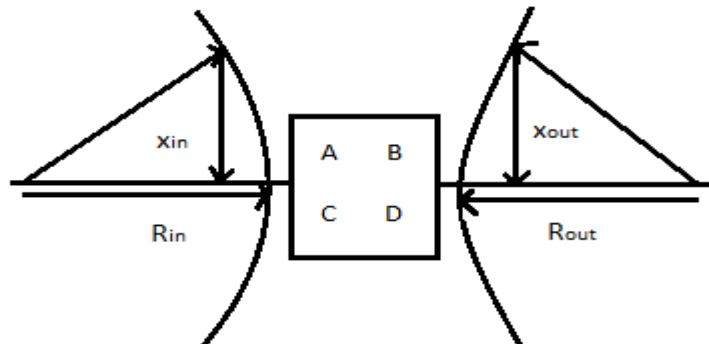
Figure 2-8: Schematic of ABCD matrix situation described above.

However, a paraxial spherical wave is not a useful analytical form for a physical propagating beam as the paraxial approximation is violated. The propagation of a simple Gaussian beam can be described by considering the source to be complex, radiating both real and complex rays. (17) Siegman's Lasers shows that in such cases the rays emanating from the source are defined by the complex beam parameter q which is related to the width of the beam w, the radius of curvature of the beam R and wavelength of radiation λ by

$$\frac{1}{q_{in}} = \frac{1}{R} - i\left(\frac{\lambda}{\pi w^2}\right). \qquad (2.24)$$

The complex beam parameter after passing through and optical element can be found from the equation:

$$q_{out} = \left(\frac{Aq_{in}+B}{Cq_{in}+D}\right)$$ (2.25)

At any point in an optical system if the complex beam parameter is known then the beam radius and radius of curvature can be found from

$$w = \sqrt{\frac{\lambda}{\pi \, Im[q^{-1}]}}$$ (2.26)

and

$$R = \frac{1}{Re[q^{-1}]}$$ (2.27)

respectively. Where *Re* and *Im* denote the real and imaginary components of the complex beam parameter.

It is clear ABCD matrices are a simple and computationally efficient means of analysing optical elements and hence complete optical systems under study, as the characteristics of a beam can easily be investigated throughout the system. Each optical component in a system has its own ray transformation matrix as does free space (or a region of uniform refractive index).

Another massive advantage of ray transformation matrix analysis is that although the analysis can be achieved on each optical element individually (e.g. ray transformation through a lens) the analysis of full systems can be carried out in one application of equation 2.25. For this to be achieved a resultant ABCD matrix for the combined system has to be determined. The matrix equivalent for a series of elements is simply the multiplication of the matrix for each element. However care must be taken to ensure that the matrix corresponding to each element are placed in reverse order with respect to the order the beam would encounter them in i.e. first element encountered is placed last when multiplying. This is demonstrated with the use of an example below. Figure 2-9 contains the ABCD matrices for different ray transformation situations. (18)

Element	Matrix	Remarks
Propagation in free space or in a medium of constant refractive index	$\begin{pmatrix} 1 & d \\ 0 & 1 \end{pmatrix}$	d = distance
Refraction at a flat interface	$\begin{pmatrix} 1 & 0 \\ 0 & \frac{n_1}{n_2} \end{pmatrix}$	n_1 = initial refractive index n_2 = final refractive index.
Refraction at a curved interface	$\begin{pmatrix} 1 & 0 \\ \frac{n_1-n_2}{R \cdot n_2} & \frac{n_1}{n_2} \end{pmatrix}$	R = radius of curvature, $R > 0$ for convex (centre of curvature after interface) n_1 = initial refractive index n_2 = final refractive index.
Reflection from a flat mirror	$\begin{pmatrix} 1 & 0 \\ 0 & 1 \end{pmatrix}$	Identity matrix
Reflection from a curved mirror	$\begin{pmatrix} 1 & 0 \\ -\frac{2}{R} & 1 \end{pmatrix}$	R = radius of curvature, $R > 0$ for concave
Thin lens	$\begin{pmatrix} 1 & 0 \\ -\frac{1}{f} & 1 \end{pmatrix}$	f = focal length of lens where $f > 0$ for convex/positive (converging) lens. Valid if and only if the focal length is much greater than the thickness of the lens.

Figure 2-9: Table of ray transformation matrices (18)

When dealing with thick lenses the transformation consists with passing from free space (or region of constant refractive index) through the curved interface of the lens, through another region of constant refractive index and finally through the second curved interface of the lens. Care must be taken to use the correct signs for the radius of curvature and refractive index values depending on the situation.

To illustrate the concept if using Ray tracing matrices to analyse the beam through an optical system consider the Gaussian Beam telescope situation depicted below: (18)
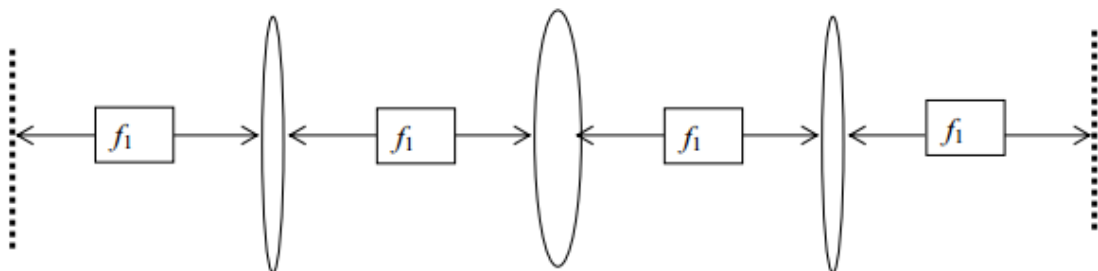

Figure 2-10: Illustration of optical system containing three lenses (18)

In this situation we will assume that the two outermost lenses have a focal length of f_1 and the middle lens has a focal length of f_2. Each outermost lens is a distance f_1 to either an input or output plane. We will assume a beam waist of 7 mm at the input plane and a radiation wavelength of 3 mm. It is desired to determine how the width of the beam at the output plane varies as a function of f_2. For this to be achieved the individual transformation matrices for each component must be multiplied or "cascaded" to obtain a resultant matrix that represents the entire system. Taking care to ensure that the first transformation undergone by the beam is rightmost in the product:

$$\begin{pmatrix} 1 & f1 \\ 0 & 1 \end{pmatrix} \cdot \begin{pmatrix} 1 & 0 \\ \frac{-1}{f1} & 1 \end{pmatrix} \cdot \begin{pmatrix} 1 & f1 \\ 0 & 1 \end{pmatrix} \cdot \begin{pmatrix} 1 & 0 \\ \frac{-1}{f2} & 1 \end{pmatrix} \cdot \begin{pmatrix} 1 & f1 \\ 0 & 1 \end{pmatrix} \cdot \begin{pmatrix} 1 & 0 \\ \frac{-1}{f1} & 1 \end{pmatrix} \cdot \begin{pmatrix} 1 & f1 \\ 0 & 1 \end{pmatrix}$$

Cascading gives:

$$\begin{pmatrix} -\dfrac{f1-\dfrac{f1^2}{f2}}{f1} - \dfrac{f1}{f2} & f1 + f1\left(-\dfrac{f1-\dfrac{f1^2}{f2}}{f1} - \dfrac{f1}{f2}\right) - \dfrac{f1^2}{f2} \\ 0 & -1 \end{pmatrix}$$

By calculating the initial complex beam parameter using equation 2.24 and hence the complex beam parameter at the output using equation 2.25, then the width of the beam at the output and radius of curvature of the beam can be calculated using equations 2.26 and 2.27 respectively. Using Mathematica^{TM} code written by the author this calculation was repeated (for different values of f_2) and the results plotted below with width in metres as a function of f_2 plotted left and radius of curvature in metres plotted right.
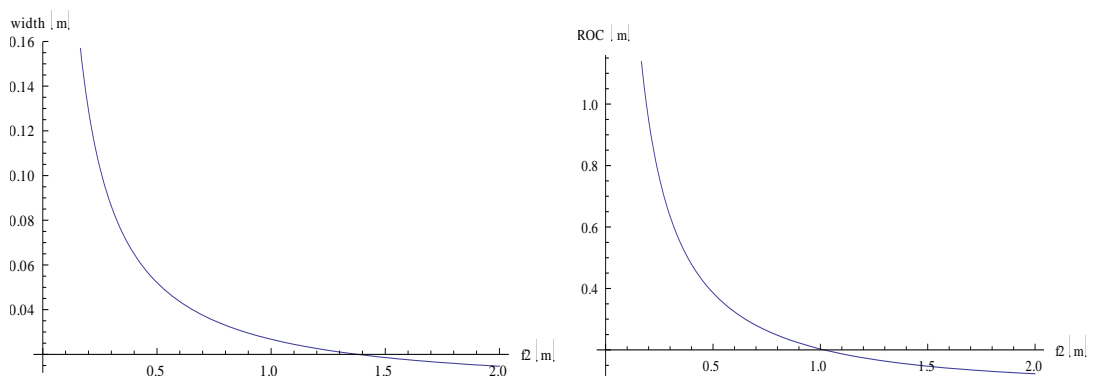

Figure 2-11: Plot of beam width in metres (left) and radius of curvature in metres (right) as a function of f_2.

From the plots in Figure 2-11 above the variation in the width and radius of curvature of the beam is clear with the radius of curvature decreasing in the same fashion as the width of the beam.

2.3 The Fresnel Kirchhoff Diffraction Integral

As discussed in section 2.1 rather than using Maxwell's equations to solve the field at a point in a system comprehensively using a full vector analysis, scalar representations of the field can be formed to obtain values for the field at a point in the system. This gives rise to diffraction integrals which effectively integrate over the source to determine the field at a distance from the source. Consider the situation as described in section 2.24 where we have a source field incident on an aperture and it is desired to investigate the electric field at a plane which is a distance z from the aperture as illustrated in Figure *2-12*.
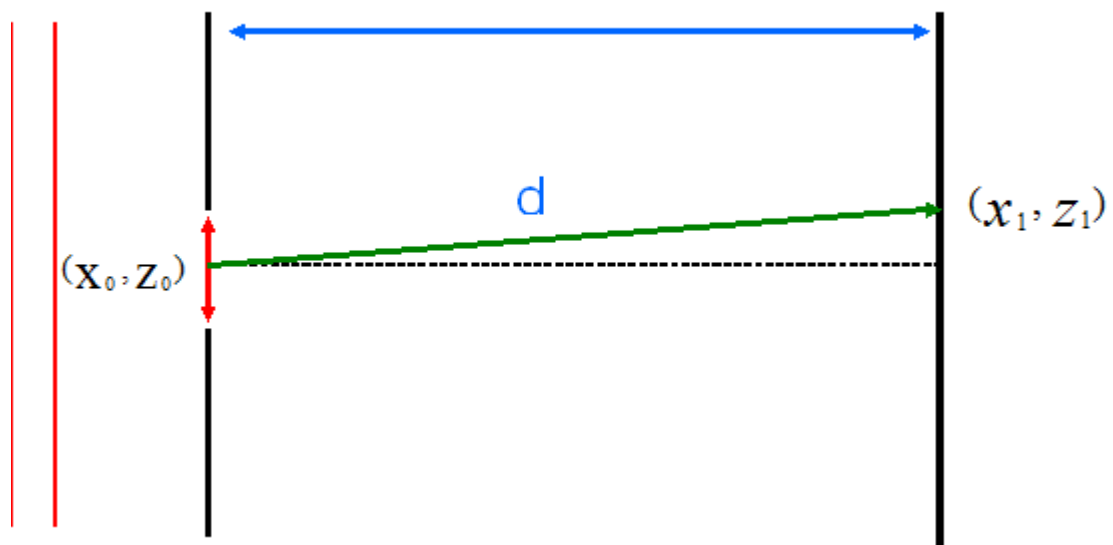
Figure 2-12: Schematic representation of a simple system consisting of a 1D aperture and screen a distance d along the z axis.

Huygens principle states that the diffraction of radiation from an aperture can be reconstructed by assuming that the aperture is made up of a large number of points, with each point acting like a point source of radiation whereby each point produces a spherical wave of radiation (19). These spherical waves interfere with each other

combining constructively where two peaks meet and destructively where a peak meets a trough. The result of these wavelets being superimposed is a diffracted wave front as shown graphically in figure 2-13 below.
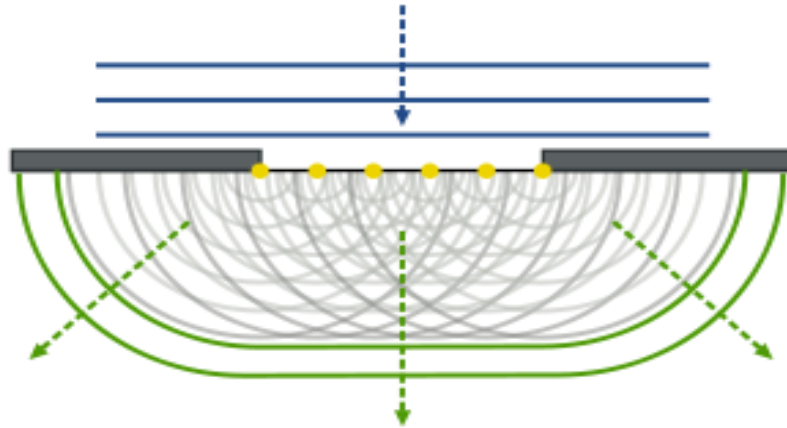

Figure 2-13: Graphical representation of the diffraction from an aperture as described by the Huygens Principle. (20)

Referring to the situation described in Figure *2-12* above, it is possible to calculate the E – field magnitude at a point on the screen by summing the contribution from each point at the aperture (i.e. integrating over the aperture). This is described mathematically by the following equation, where A is the input field Amplitudes, λ is the wavelength of the radiation and r is the length of the vector pointing from a single point at the aperture to the point of interest at the screen (19)

$$E(x_1, z_1) = -\frac{Ai}{\lambda} \int \frac{e^{ikr}}{r} \left[\frac{1+cos\theta}{2}\right] ds \qquad (2.28)$$

The k value is called the wave number and represents the phase oscillations as the wave propagates (i.e. k = 2π/r). The value of the r vector is derived using simple coordinate geometry and is described using the following expression, where (x_p, z_p) is the point of interest on the screen and (x_a, z_a) is a point on the aperture.

$$r = \sqrt{(x_p - x_a)^2 + (z_p - z_a)^2} \qquad (2.29)$$

The term in brackets in equation 2.28 is commonly referred to as the obliquity factor whose value falls in the range 0 → 1. It ensures the directionality of the wave is a function of direction i.e. that there is not backwards motion of the wave. In other

words as the angle of the source field incident on the aperture increases, the amplitude per unit area at the viewing screen will decrease (19).

2.4 Physical Optics

Consider a scattering problem where we have a known incident field on a scattering element of known geometry and electrical properties. The goal is to compute the radiated field from the scattering element. A useful relationship when dealing with these types of situations is denoted by

$$\bar{E} = \bar{E}_\iota + \overline{E_s}$$
(2.30)

where $\bar{E}_\iota$ is the incident electrical field, $\overline{E_s}$ is the scattered field and $\bar{E}$ is the total field. If it is perfectly conducting $\overline{E_s}$ is generated by induced surface currents on the surface of the scattering object. In the case of non-perfectly conducting surfaces a set of equivalent electric and magnetic surface currents can be computed which exactly replicates the scattered field. Undertaking scattering analysis on an element consists of three main steps: (21)

1) Calculate the induced or equivalent source currents.
2) Calculate the radiated field by these currents.
3) Add incident and scattered fields to obtain total field.

The first step is the most complicated and modelling it involves computationally intensive techniques such as a method of moments that becomes very time consuming for large scatterers. This is where Physical optics comes to the fore as it is a simple approximation method that gives an approximation of the surface currents valid for perfectly conducting scatterers which are large in terms of wavelengths. The second step requires no further approximations since the radiation integral of the surface currents can be computed by numerical integration with high precision. In a case where the surface of the scatterer is not perfectly conducting but refection and transmission coefficients are known the physical optics method can be modified to give an approximation of the equivalent electric and magnetic surface currents. (21)

In the Physical Optics approximation it is assumed that the surface current in a specific point on a curved, but perfectly conducting scatterer is the same as the surface current on an infinite planar surface which is tangent to the scattering surface in this point.

The induced surface currents (which are induced by incident magnetic field) on a perfectly conducting infinite plane surface illuminated by an arbitrary incoming field are given by the following equations (22)

$$\bar{J}_e = 2\hat{n} \times \overline{H}_\iota \tag{2.31}$$

and

$$\bar{J}_m = 2\hat{n} \times \overline{E}_\iota \tag{2.32}$$

where, $\bar{J}_e$ and $\bar{J}_m$ are the induced electric and magnetic fields respectively, $\hat{n}$ is the normal to the surface (pointing away from the illuminated surface), $\overline{H}_\iota$ is the incident magnetic field and $\overline{E}_\iota$ is the incident electric field. The radiated fields resulting from the induced surface currents can be obtained from Pontoppidan (22)

$$\bar{A}_e = \frac{\mu}{4\pi} \iint_B \bar{J}_e(\bar{r}') \frac{e^{-ikR}}{R} ds' \tag{2.33}$$

$$\bar{A}_m = \frac{\varepsilon}{4\pi} \iint_B \bar{J}_m(\bar{r}') \frac{e^{-ikR}}{R} ds' \tag{2.34}$$

$$\bar{E} = -i\omega \left(\bar{A}_e + \frac{1}{k^2} \nabla(\nabla \cdot \bar{A}_e) \right) - \frac{1}{\varepsilon} \nabla \times \bar{A}_m \tag{2.35}$$

$$\overline{H} = \frac{1}{\mu} \nabla \times \overline{A}_e - i\omega \left(\overline{A}_m + \frac{1}{k^2} \nabla(\nabla \cdot \overline{A}_m) \right) \tag{2.36}$$

where $\bar{A}_e$ is the electric vector potential, $\bar{A}_m$ is the magnetic vector potential and ε and μ are the permittivity and permeability, respectively. The parameter ω is the angular frequency and k is the wave number (as described in section 2.3). The distance R is represented by $R = |\bar{r} - \bar{r}'|$ where $\bar{r}$ is the observation point and $\bar{r}'$ is the integration variable running over the surface. The subscript B on the integrals denotes integration over the entire surface of the scatterer. From equation 2.35 and 2.36 it is clear that the

radiated electric and magnetic fields are found by applying the required differential operator on $\bar{A}_e$ and $\bar{A}_m$. The result becomes:

$$\bar{E}(\bar{r}) = \frac{\gamma}{4\pi} \iint_B \left(\bar{J}_e \left(-\frac{i}{kR} - \frac{1}{k^2 R^2} + \frac{i}{k^3 R^3} \right) \right.$$

$$+ (\bar{J}_e \cdot \hat{R})\hat{R} \left(\frac{i}{kR} - \frac{3}{k^2 R^2} + \frac{i}{k^3 R^3} \right) \bigg) e^{-ikR} k^2 ds' \qquad (2.37)$$

$$- \frac{1}{4\pi} \iint_B \bar{J}_e \times \hat{R} \frac{1}{k^2 R^2} (1 + ikR) e^{-ikR} k^2 ds'$$

and

$$\bar{H}(\bar{r}) = \frac{1}{4\pi} \iint_B \bar{J}_e \times \hat{R} \frac{1}{k^2 R^2} (1 + ikR) e^{-ikR} k^2 ds'$$

$$\frac{1}{4\pi\gamma} \iint_B \left(\bar{J}_e \left(-\frac{i}{kR} - \frac{1}{k^2 R^2} + \frac{i}{k^3 R^3} \right) \right. \qquad (2.38)$$

$$+ (\bar{J}_e \cdot \hat{R})\hat{R} \left(\frac{i}{kR} - \frac{3}{k^2 R^2} + \frac{i}{k^3 R^3} \right) \bigg) e^{-ikR} k^2 ds'$$

where

$$\hat{R} = \frac{\bar{R}}{R} = \frac{\bar{r} - \bar{r'}}{|\bar{r} - \bar{r'}|} \qquad (2.39)$$

and γ is the free-space impedance $\gamma = \sqrt{\mu/\varepsilon}$.
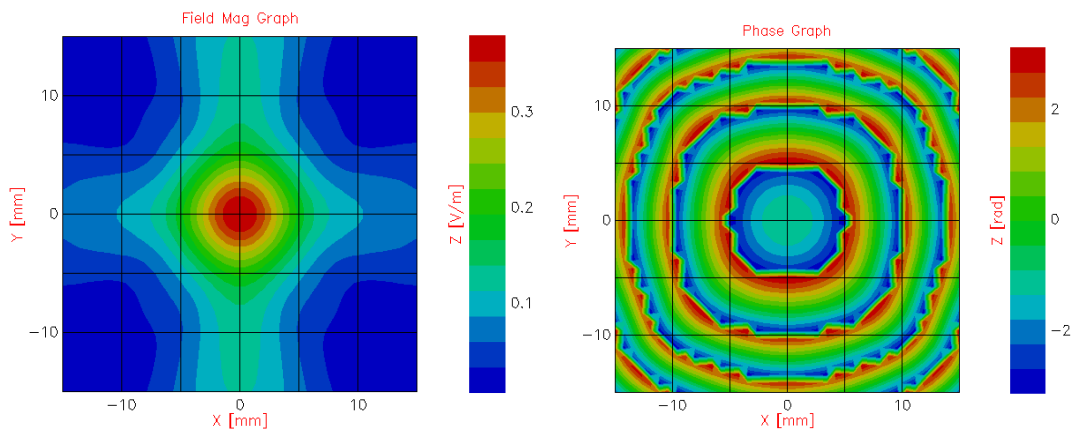
Figure 2-14: Field magnitude (left) and phase (right) of radiation after propagating through a square (6 mm wide) aperture. A Plane wave of radiation (100 GHz) placed at a distance of 30 mm, was incident on aperture and field sampled at a distance of 10 mm.

2.5 Introduction to MODAL

The Quasi Optical analysis of the systems contained in this thesis (including the plots above) were developed using an in house software package called MODAL. MODAL is an acronym for Maynooth Optical Design and Analysis Laboratory. The software is currently under development by Dr. Marcin Gradziel originally under an SFI grant. A previous prototype was developed by Dr. David White (23).

Unlike other software packages (such as Grasp) that are used to analyse systems at the wavelengths considered in this thesis, MODAL is specifically designed to target the THz region of the EM spectrum. Although other packages are accurate at these wavelengths they are designed to operate over a wider range of frequencies. MODAL was also designed to have a user friendly approach to system definition through a wide variety of implementation approaches.

MODAL also incorporates a wide variety of propagation techniques at these wavelengths namely Physical Optics, GBMA, and Fresnel Diffraction. To propagate the radiation through a system, propagators are used to propagate the radiation from one element to the next. The author implemented a simple system to illustrate the principles at work. To this end we will consider the system used to produce the Physical Optics plots in Figure 2-14 above. All aspects of MODAL are discussed in greater detail in Appendix A. Only a simple overview of essential mechanisms is presented in this section.

This system although simplistic can be used to illustrate the fundamentals of each system in MODAL. It consists simply of a plane wave source incident on a square aperture. To measure the resultant field transmitted through the aperture (also to examine diffraction effects) an output plane is placed on the opposite side to the source as shown in Figure 2-15.
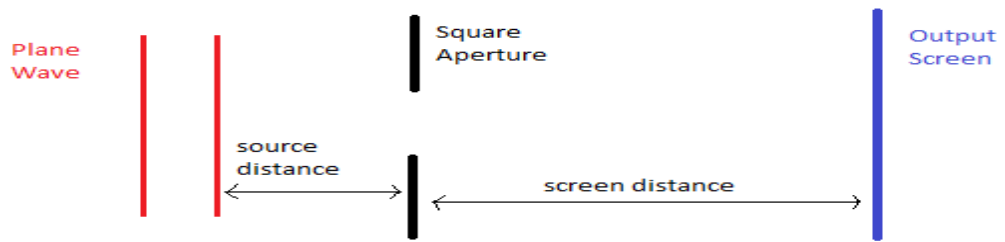
Figure 2-15: 2d schematic of system implemented, output plots plotted in Figure 2-14.

When defining this system the output screen was placed at the primary reference point (global reference point). The aperture reference frame was then defined in terms of a transformed frame with respect to the initial global reference frame. The plane wave reference frame was then defined in terms of a transformed frame with respect to the aperture frame. The incident plane wave was defined in such a way that its angle with respect to the aperture can be altered by the user to investigate radiation incident at different angles. It should be noted that the aperture actually extends to infinity although is just illustrated in Figure 2-16 as a black region in the vicinity of the opening in the project viewer.
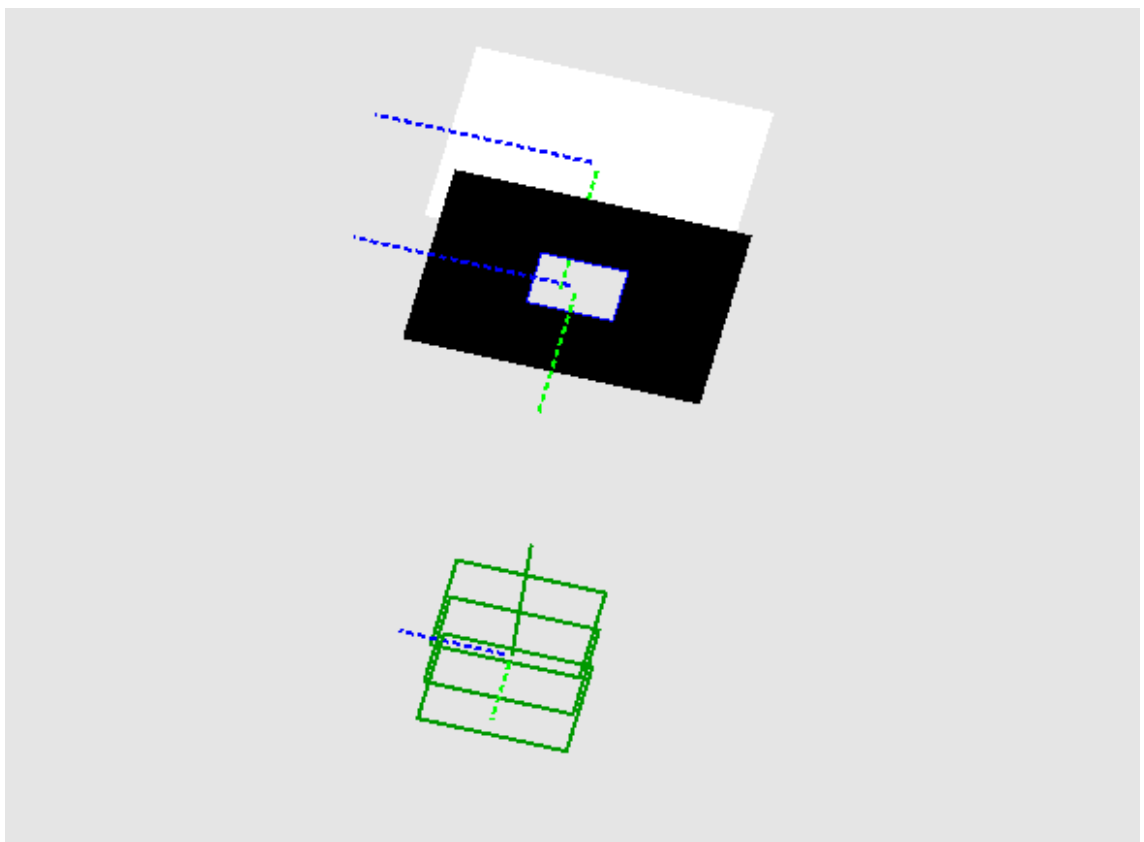

Figure 2-16: Screenshot of implemented system from MODAL's system viewer.

Physical Optics was used for propagating radiation through the system. As previously stated, propagators are used for propagating the radiation from the source to an element then from this element to the next and so on. MODAL uses a mapping technique for creating the points to be used for computational calculations for the propagators. This mapping technique is discussed in more detail in Appendix A. Once the radiation is propagated to the output plane of interest, the radiation can then either be plotted or exported using a dataset exporter. Also the power incident (along with other numeric parameters) can be plotted at each element to investigate parameter variation throughout the system (Appendix A).

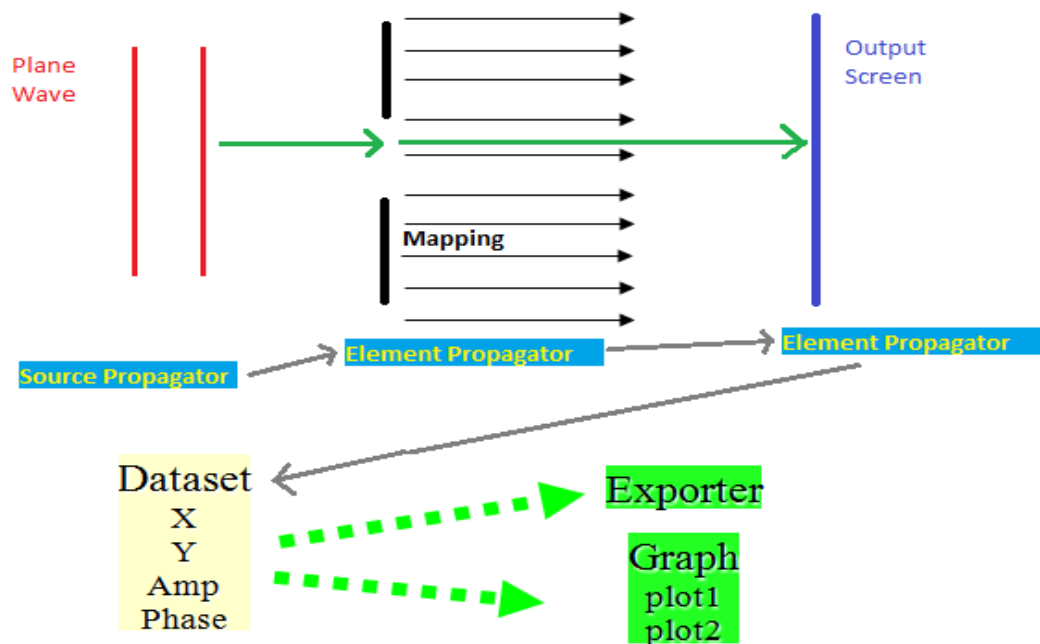*Figure 2-17: Diagram explaining operation of MODAL.*

The Field Magnitude and Phase when the direction of propagation of the source radiation is exactly perpendicular to the surface of the aperture plane are presented in Figure 2-15 above. The effects of tilting the plane wave through an angle of $15°$ so that the radiation is incident at an angle are illustrated in Figure 2-18 and Figure 2-19.
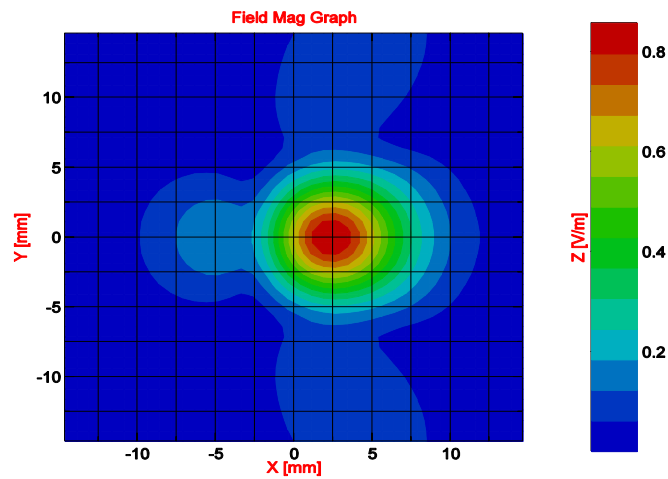
Figure 2-18: Magnitude results of model implemented by the author, placing plane wave source 30 mm from aperture at $15°$ angle with aperture 6 mm (2λ) wide and output 10 mm from aperture.
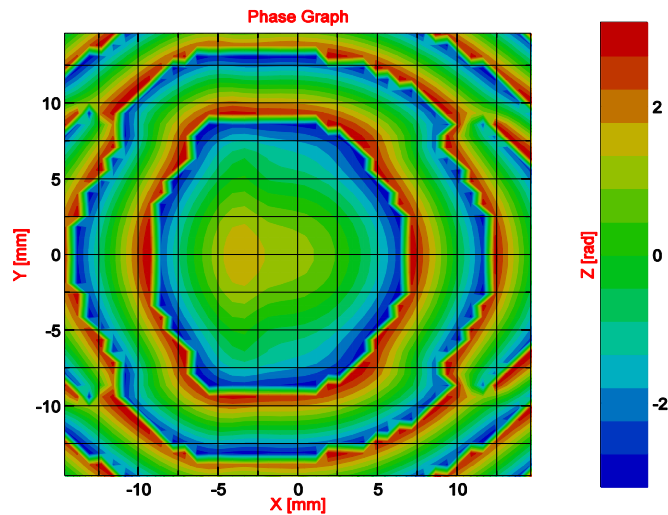
Figure 2-19: Phase results of placing plane wave source 30 mm from aperture at $15°$ angle with aperture 6 mm (2λ) wide and output 10 mm from aperture.

One of the main advantages of MODAL over other commercially available software packages is its ability to deal with dielectric lenses.

When a lens is present in an optical system the surfaces of the lenses have to be treated as dielectric interfaces and so only the Physical Optics (PO) approach can be used (24). With this approach the radiation is broken up into reflected and transmitted (R(0) and T(0) respectively) components and the field is treated as locally spherical in the vicinity of the lens interface. The angle of incidence is calculated by the local direction of the pointing vector and surface normal. The orientation and complex

40

amplitude of the transmitted and reflected fields can be calculated using the standard Fresnel relationships (25). The radiation is then propagated to the back surface of the lens where it is again broken up into its Transmitted and Reflected components (T1) and L(1). This "bouncing" process is repeated until the power in the lens is below a set threshold or a certain number of iterations have passed. The threshold power cannot currently be changed by the user however recent versions of MODAL enable the number of iterations required to be changed by the user. This was introduced for modelling done as part of this thesis in an attempt to reduce computation time. The previous default value was 5 iterations however most of the work carried out in this thesis used 2 iterations without a reduction in the accuracy of the field model. It must be ensured however that a sufficient number of PO points are used to facilitate the convergence of PO steps between the surfaces. The contributions from the individual iterations are then summed to give the total transmitted and reflected fields for the lens as illustrated in Figure 2-20 as discussed by Curran (25).
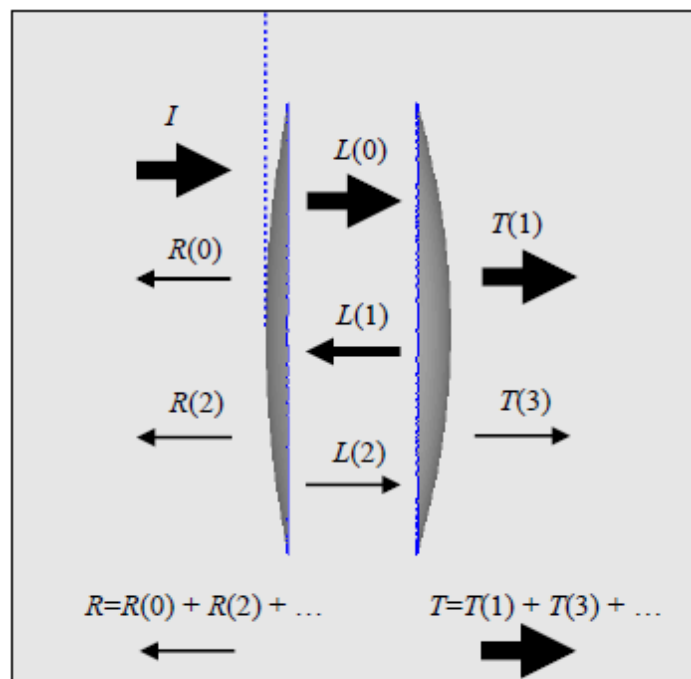

Figure 2-20: PO propagation through a dielectric lens in MODAL where I represents the incident field and R(n) and T(n) represent reflected and transmitted components respectively and L(n) represents the wave propagating through the lens. (24)

3 Chapter 3

Computational modelling and verification of Optical Design used

3.1 Overview

This Chapter will discuss the development of the design and theoretical testing of the Optical System used. Nearly all of the modelling work was carried out using the MODAL software package. As discussed in section 1.4.2 above additional optical components are needed to focus the radiation from the source onto the tilting mirrors and from the mirrors onto the target of interest. The following sections will reveal the thought process behind the decision on which elements to use and their location within the system. The requirements of the system will also be outlined along with the work carried out to verify the optical components used (in particular the lenses) i.e. verifying that MODAL systems were representative of real world systems.

3.2 Requirements / constraints on system

The beam launcher (which also acts as the detector) to be used with the Transmitter/Receiver module is a corrugated feed horn with a beam width at the aperture of 4.596 mm. The beam then has to be focused onto the tilting mirrors used for directing the beam (ideally there will be a beam waist at this location) which were defined to be 20 x 20 mm in area. After propagating from the mirrors further components are needed to focus the beam to a desired width at the object plane. The beam will then be reflected from the object back through the system (along the same optical path) to the corrugated horn (where an image of that pixel can be formed). As the system has to be symmetrical it is essential to have a beam waist at the object plane because if this is not the case, the beam will not travel back along the same path having the correct widths at the desired locations. For example the beam width at the tilting mirrors during illumination will not be the same as when the radiation is being detected (reflected back).

Care was also taken to ensure that the beam width at the focusing components is not wider than the component itself so as to avoid beam truncation. As discussed in section 1.4.2 it was established that post processing would be necessary for the data received. This imposed a minimum beam width requirement at the object plane of $\approx 15 \, mm$ as the beam could not be too focused. The system was also to have the following scanning capability requirements.

- The scanner should be capable of scanning an area 30 x 30cm.
- An initial value of 1 metre was set as a desired scanning distance (i.e. distance from the last focusing component to the target).

Finally, as the scanner was essentially to be a proof of concept the focusing system was to be devised from in house and currently existing components where possible. Figure 3-1 shows a MODAL view of how the system was to operate. The system shown is an early version incorporating only two lenses which is now rendered obsolete however it illustrates the concept adequately. The black box surrounding the mirrors represents the housing of a scanner (see Figure 3-2) that was to be used however due to the motor breaking beyond repair, this method was abandoned.
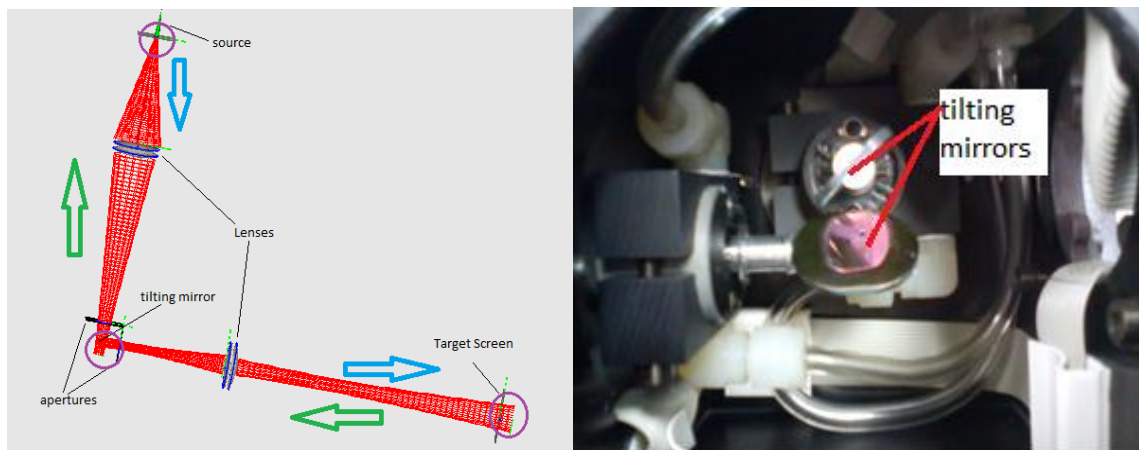

Figure 3-1 (left): View from MODAL's viewer illustrating what the demands on the system design are. Blue arrows indicate path of illuminating radiation and green arrows represent reflections back through the system. Figure 3-2 (right): Picture of inside of original scanning unit that was to be used.

3.3 Existing Components

As was mentioned above the system was designed using existing and in-house components only. These components had been designed and manufactured for previous MSc and PhD projects within the Terahertz group.

They included;

FourPlano-convex lenses with focal lengths of 250 mm.

A pair of parabolic mirrors with a focal length of 150mm and an angle of throw of 90°. (26)

A pair of ellipsoidal mirrors with focal lengths of 500mm and an angle of throw of 45°. (24)

A pair of parabolic mirrors with focal lengths of 350mm and an angle of throw of 90°. (27)

A set of three ellipsoidal mirrors with a focal length of 500mm and an angle of throw of 45° designed to operate for mm-wave radiation.

These were quickly disregarded however, as they were designed with mm-wave radiation in mind which requires a less smooth finish. For operation at 100 GHz the mirror surface needs to be smoother to operate with the shorter wavelength. (27)

When this project was commenced the author assisted Dr Vladimir Yurchenko with the alignment of a Gaussian Beam Telescope setup for the purposes of measuring transmission through a sample placed at the centre of the setup. As two focusing elements were required Dr. Yurchenko designed a pair of dielectric lenses. The lenses are comprised of two hyperbolic surfaces and machined from Teflon. They were specifically designed to work with the corrugated feed horn used in this system in such a way that if the horn aperture is placed 125 mm from the first surface the sample under investigation will be illuminated by a region of flat phase curvature (a beam waist). The dimensions of the first half of Dr. Yurchenko's system is illustrated in Figure 3-3.
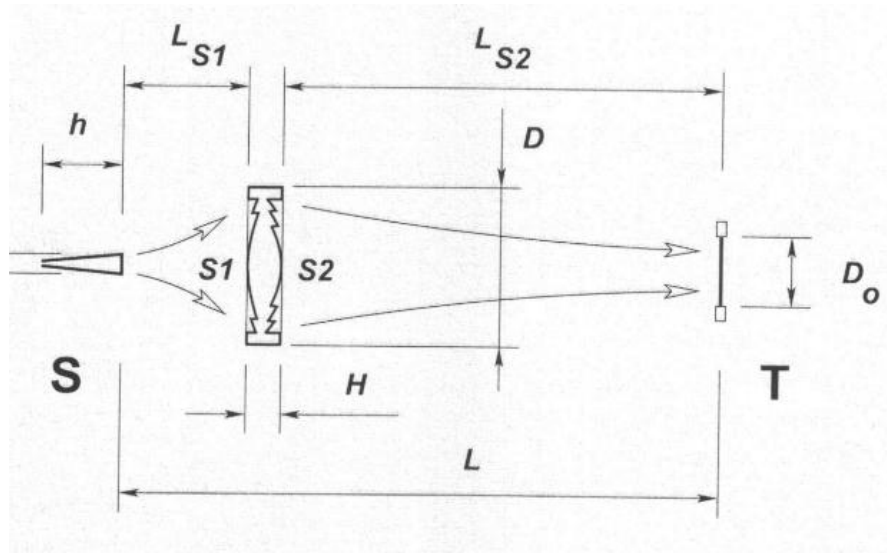
Figure 3-3: Dimensions of the first half of Dr. Yurchenko's Gaussian Beam Telescope.

System Dimensions		System Parameters	
L_{s1}	125 mm	Horn aperture radius	7.13 mm
L_{s2}	435 mm	Width / ROC at aperture	4.593 / 80 mm
L	595 mm	Frequency	100 GHz
H	35 mm	Waist width target	16.8 mm
H	80 mm	D_0 (sample width)	72 mm
		Power at edges of sample	-40 dB

Table 3-1: Dimensions and parameters associated with Gaussian Beam Telescope system.

For the purpose of reducing the amount of material used and hence reducing power attenuation through the lens, the lenses have a stepped profile with the surface of higher radius of curvature (ROC) having one step and the surface of lower ROC having two steps as illustrated in Figure 3-4. After consultation with Dr. Yurchenko it was discovered that the lenses were designed assuming a refractive index value of 1.431. However due to the granular variation of Teflon throughout the world (although a glass like polymer is still has a granular structure) (28), and the differences in manufacturing procedure throughout the world, and the fact that the sample had not been measured the refractive index of the material was not conclusively known.

Figure 3-4: Lenses provided by Dr. Yurchenko. Side with lower ROC (Left). Side with higher radius of curvature (Right).

3.4 Modelling of Lenses

3.4.1 Implementation of Lenses in MODAL

For the lenses to be implemented in MODAL the radius of curvature and conic constant of the surfaces had to be defined however little was known about the definition of the surfaces. A data file consisting of coordinate points of a cut through the lens, used for machining the lens was provided by Dr. Yurchenko. It was decided to fit a hyperbola to the data to try and extract the necessary parameters. If we consider the *x*-axis of a system to be a cut through a lens profile the corresponding surface points in the y-direction can be determined from

$$y = y_0 + \frac{kx^2}{1+\sqrt{1-k^2x^2(1-c)}} \tag{3.1}$$

where

$$k = \frac{1}{R} \tag{3.2}$$

Where R is the radius of curvature of the hyperbola, and c is the conic constant which is related to the eccentricity of the hyperbola by: (29)

$$c = 1 + e^2 \tag{3.3}$$

To fit the hyperbola the heights of the steps had to be estimated and the data corrected for these jumps, so as to have a smooth continuous hyperbola for fitting to.

46

An estimate for these jump values was found by plotting the curves in Excel and performing mathematical operations to the data until a smooth curve was obtained. The fitting routine used was the Levenberg–Marquartd algorithm which was implemented using LabVIEW software. The parameters determined for the surfaces are presented in the following table.

	Side One	Side Two
Radius of Curvature	127.816	-80.7758
Conic Constant	-4.9809	-1.203
Offset on y - axis	0.09634	34.904

Table 3-2: Results from fitting routine.

Once the key parameters were discovered the lens could then be implemented in MODAL. The Lens was implemented by first defining the hyperbolic surface. The section of the surface to be used was then selected by defining a bounding volume in terms of a cylinder with the same diameter as the lens. The steps in the profile were defined in a similar fashion with the diameter of the cylinder being equivalent to the width of each step. The surfaces could then be offset from one another by the height of the step.

To verify that it was implemented properly the profile of a cut through the surface was extracted to a data file and plotted for comparison with the profile obtained from Dr. Yurchenko. However it was discovered that there was a discrepancy between the profiles, in particular with the values estimated for the step heights. Initially the step heights were estimated by visually inspecting the data, however as the jump in the profile occurred over a series of data points this lead to inaccuracies. The values were then re-determined and the data on the higher side of the profile reduced by the estimated step height and the data of both sides plotted. This process of re-estimating the step height and plotting was repeated until a continuous (non-stepped) hyperbola was obtained meaning that the estimated step height was correct. The results of the calculations before and after correction are illustrated in Figure 3-5 and Figure 3-6 below.
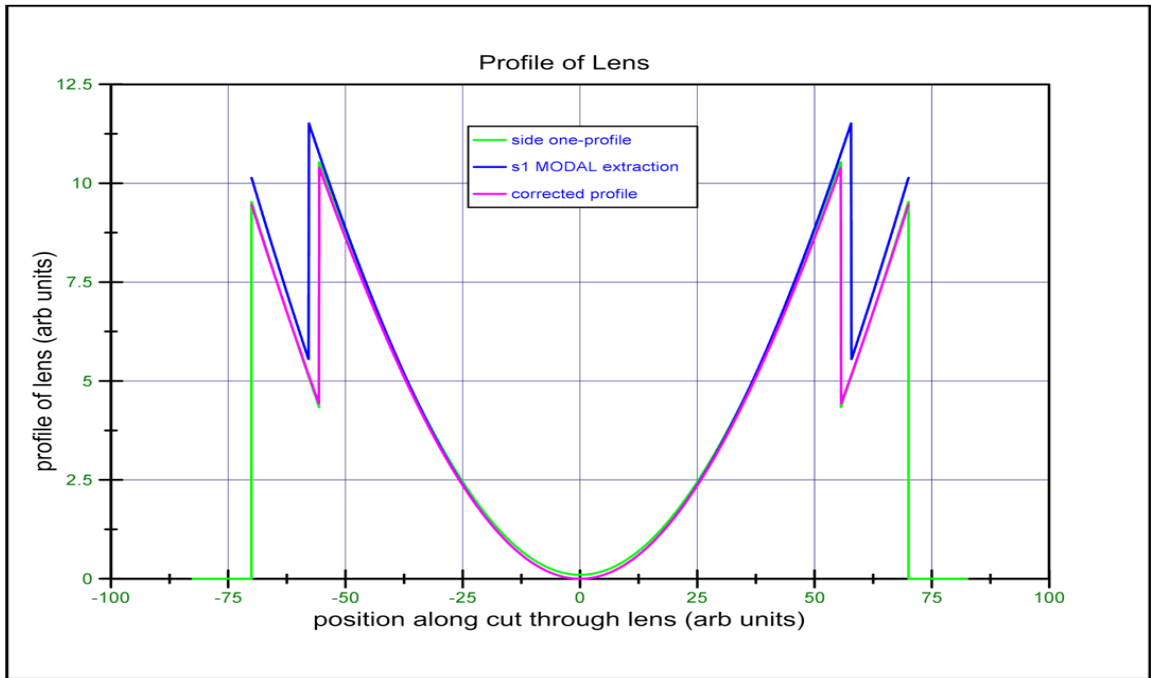
Figure 3-5: Plot of profiles of lens illustrating differences in profiles before and after correction. Data provided by Dr. Yurchenko (green) initial profile from MODAL (blue) and corrected profile (pink).
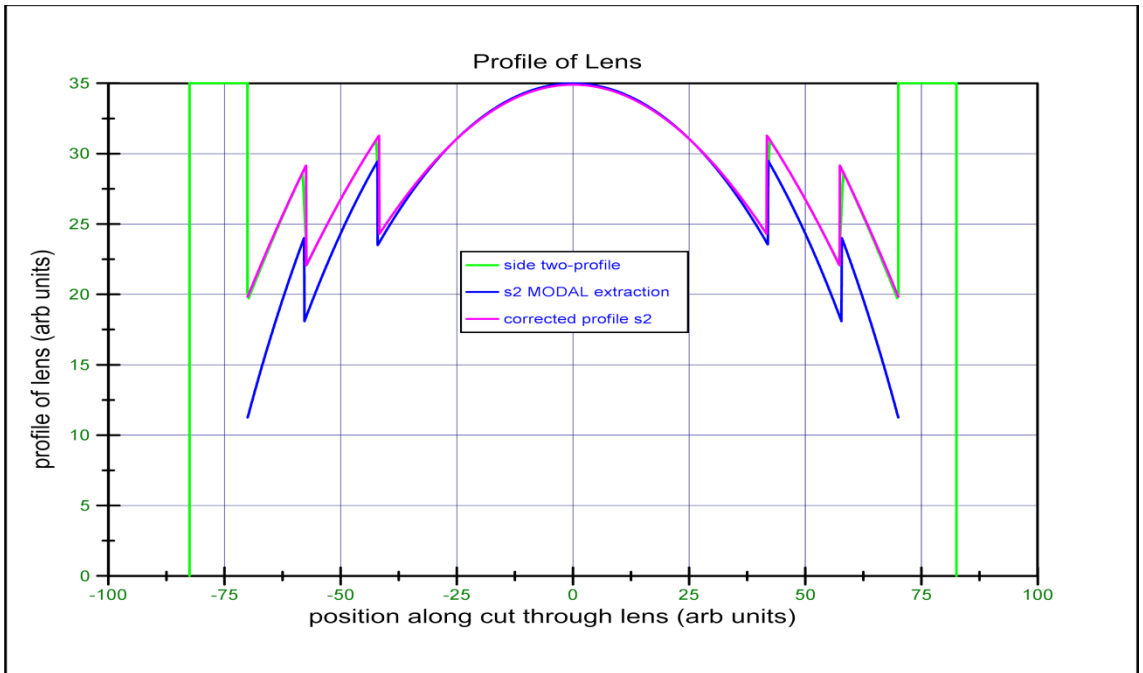

Figure 3-6: Plot of profiles of lens illustrating discrepancy in profiles and before correction for side two. Data provided by Dr. Yurchenko (green) initial profile from MODAL (blue) and corrected profile (pink).

3.4.2 Verification of Lens model

Once the Lenses were accurately implemented in MODAL the next step was to verify that they were performing correctly i.e. that their performance in MODAL was representative of the real life situation. To investigate this Dr. Yurchenkos system (see Figure 3-3) was implemented in MODAL to investigate if his predicted results could be recreated. To achieve this, a corrugated horn source as used by Dr. Yurchenko was implemented and placed at a fixed distance of 125 mm from the first lens surface. A movable output plane was then defined on the opposite side of the lens for investigating radiation characteristics at desired locations. PO propagators were used for propagating the radiation from the source to the lens and from there to the output plane.

The aim was to reconcile Dr. Yurchenkos prediction of a beam waist at a location of 435 mm from the second lens surface (470 mm from the first surface) with MODAL. However upon inspection of the beams it was found that instead of the radiation being focused to a waist beyond the lens, the beam continued diverging so it was clear that there was a serious problem with the model.
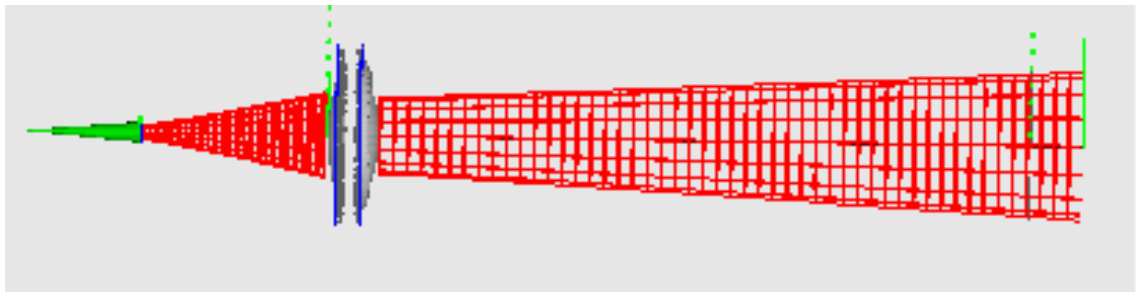
Figure 3-7: Screenshot from MODAL depicting diverging beam which was not what had been expected.

When the radiation was propagated through the system it was expected that there would be a fairly wide distribution of power at the output plane consistent with a diverging beam as illustrated in Figure 3-7. However it was found that the beam was quite focused suggesting a discrepancy between the beam drawings and the PO representation.
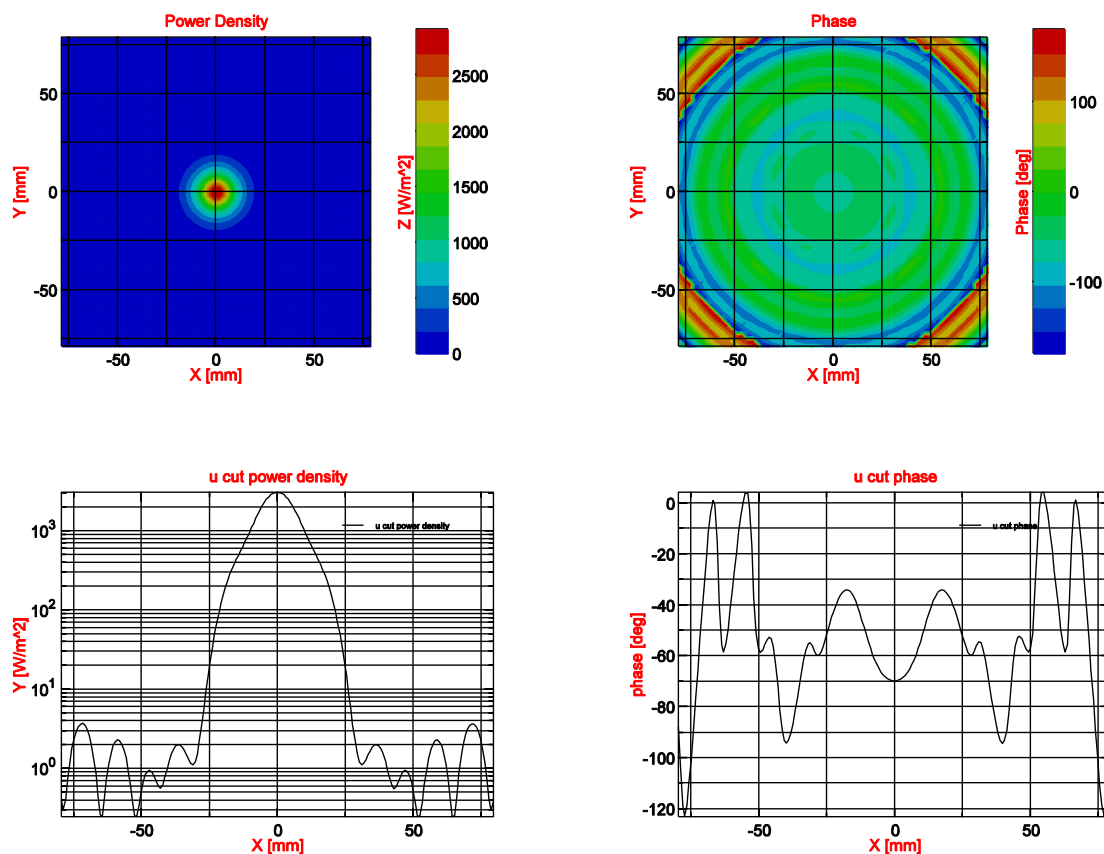
Figure 3-8: Plots of Power Density and Phase at a distance of 435mm from the lens.

From the section through the phase distribution plot in Figure 3-8 it is clear that although the phase distribution is fairly flat at this location, it is not completely flat and so it is possible that the beam waist is not located here. When Dr. Yurchenko designed the lenses it was desired to only have a fairly flat phase surface located at 435 mm and so this location didn't necessarily have to be the beam waist. Before the lenses could be used in any kind of an optical design it was clear that the performance of the lens must be more precisely understood.

3.4.2.1 Measuring Refractive Index of Lenses

As there was some uncertainty over the refractive index value of the Teflon from which the lens was manufactured, it was decided to attempt to measure the value. Consider a situation where we have a transmitting and detecting waveguide pair positioned facing each other in such a way that one is emitting radiation through a region of uniform refractive index to the second waveguide. The phase angle change due to propagating this distance *d* between the horns can be determined from the equation

$$\emptyset = \frac{w}{c} \cdot n \cdot d \tag{3.4}$$

Where w is the angular frequency of the radiation and c is its speed, n is the refractive index of the medium and d is the distance between the horns. But we know that;

$$k = \frac{w}{c} \tag{3.5}$$

Where k is the wave number and is related to its wavelength by the expression $\frac{2\pi}{\lambda}$.

By substituting this expression for k into equation 3.4 and using the relation $c = \lambda f$, equation 3.4 becomes:

$$\emptyset = \left(2\pi \frac{n}{c} d\right) f \tag{3.6}$$

Similarly in free space

$$\emptyset_0 = \left(2\pi \frac{1}{c} d\right) f \tag{3.7}$$

Now say we want to measure the refractive index of a material of thickness d this can be achieved by utilising the theory outlined and making use of the Vector Network Analyser (VNA) and its W band converter heads currently available in the department.

The VNA is capable of measuring accurately the magnitude and phase of radiation across a specific frequency band. The W-band covers a frequency range stretching from 75-110 GHz and the heads are equipped with WR10 waveguides. This is an international specification for waveguides. The '10' means that the width of the guides are one tenth of an inch. (26)

To determine the refractive index of a sample the heads are placed at a distance d from each other and a phase scan across the frequency range is measured at the detecting head from the transmitting head, the sample is then placed between the heads and the frequency scan repeated. The idea is that when the dielectric is introduced a frequency dependant phase delay is induced, by calculating the difference in delay and finding the slope of the curve the refractive index can be determined as:

$$\Delta\emptyset = \emptyset - \emptyset_0 = \left(2\pi \frac{d}{c} (n - 1)\right) f \tag{3.8}$$

and hence,

$$slope = 2\pi \frac{d}{c}(n-1) \qquad (3.9)$$

where *d* and *c* are known quantities. After the phase was measured using the VNA an automated program was written by the author using LabVIEW to post process of the data and return a refractive index value if the user provides a value for *d*.

The refractive index of the lens was measured by placing the centre of the lens between the waveguide ports on the converter heads so that the distance between the heads and by extension thickness of material was 35mm. The apparatus used is illustrated in Figure 3-9 below. After post processing the refractive index value was measured to be 1.436. The data was then exported to Microsoft Excel and using its "LINEST" function the error on the slope was calculated which was then used to calculate an error range. The final value for the refractive index was determined to be 1.436 $\mp$ .001 which was in close agreement with the value provided by Dr. Yurchenko of 1.431, the discrepancy can be explained by the fact that the thickness of dielectric was not uniform due to the curvature of the lens surface.
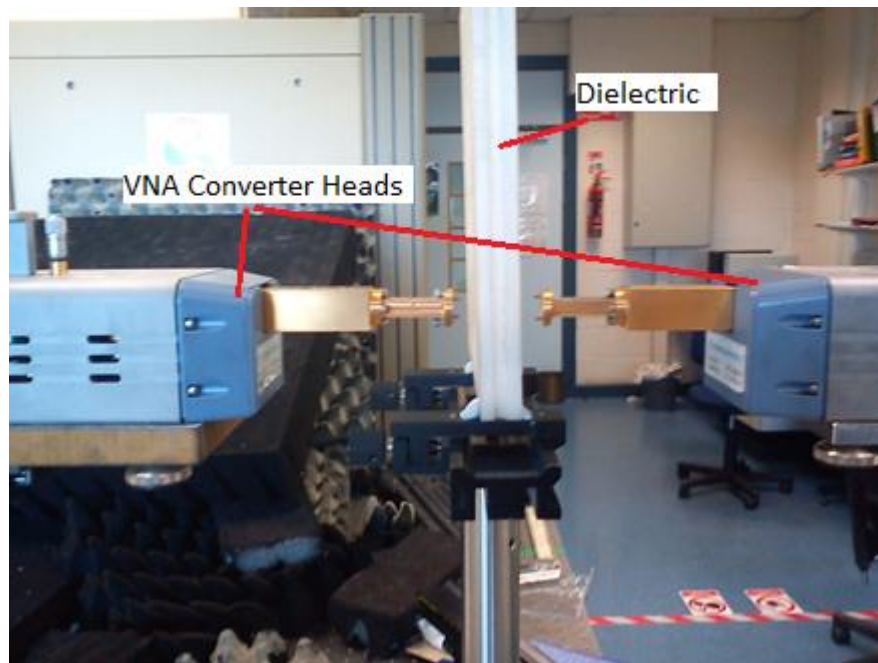

Figure 3-9: Photograph of setup used for determining refractive index. In this case the refractive index of a piece of high density polyethylene is being measured.

3.4.2.2 Modelling of lenses in Mathematica

As the refractive index value being used was verified it was decided to use ABCD matrices coded by the author using Mathematica to plot the beam width and phase radius of curvature from the second surface of the lens on-wards. In such a way that the beam waist position could be investigated i.e. where the width was at a minimum value and the radius of curvature was infinite. This was essentially to be an independent verification to compare with Dr. Yurchenkos predictions and the model in MODAL. The same procedure as was discussed in section 2.2.5 for modelling propagation through a thick lens was implemented in this situation.
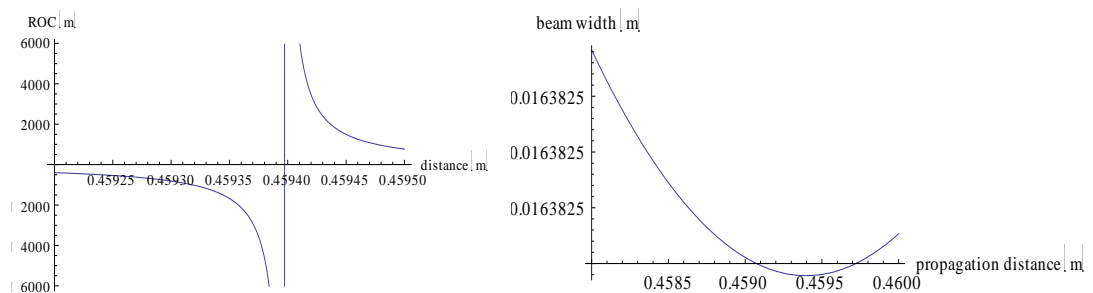

Figure 3-10: Plots from Mathematica of radius of curvature in metres (left) and beam width in metres (right) as a function of distance (also in metres) from the lens.

From the plots in Figure 3-10 it is clear that the beam waist position is located at a distance of 459.4 mm from the second side of the lens. This did not coincide with Dr. Yurchenko's predictions.

3.4.2.3 Determining beam waist position using Phase curvature

As the Mathematica model did not correspond to the waist position predicted by Dr. Yurchenko and as there was some ambiguity about the beam waist position in the MODAL program it was decided to try and determine the beam waist position in MODAL by investigating the phase profile at different distances from the lens. The idea is that as the radius of curvature changes from positive to infinite to negative as it passes through the beam waist. By sampling the phase at different locations along the axis of propagation it would be possible to see the progression of the phase and identify the waist as the position with flattest phase (infinite curvature).
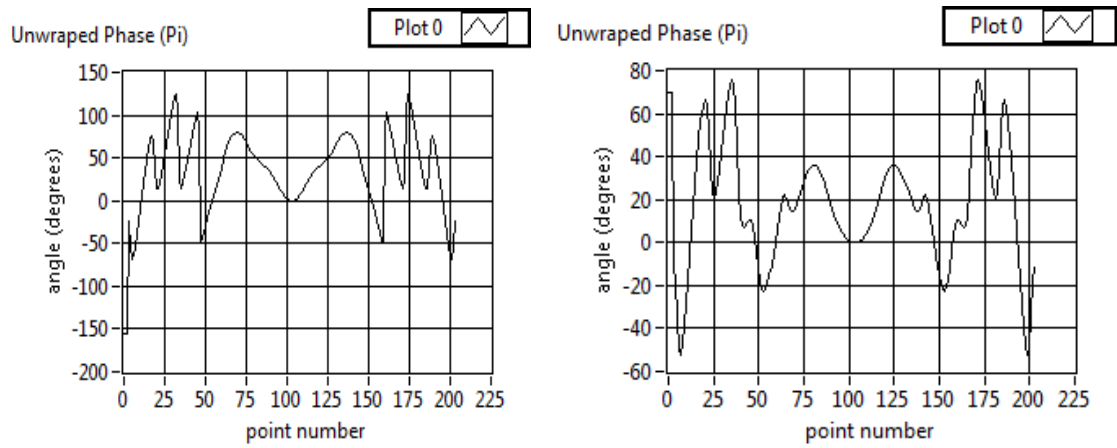
Figure 3-11: Plot of unwrapped phase plotted with output screen at 400 mm (left) and 435 mm (right) from second surface of lens.
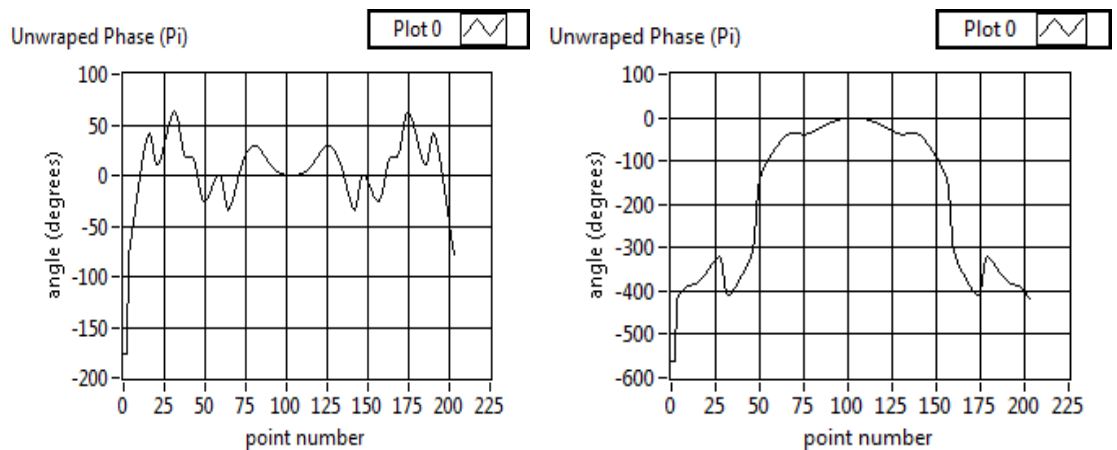

Figure 3-12: Plot of phase at 459.4 mm (left) and 540 mm (right). Illustrating phase evolution

The plots in Figure 3-11 andFigure 3-12 show the phase data that was extracted from MODAL and plotted. When the raw data was initially extracted it was then unwrapped using LabVIEW code written by the author. The evolution of phase can be seen as the field propagates from the 435 mm mark through the beam waist to the 540 mm mark. The phase curvature (and hence the beam waist) was determined to be flattest at 459.4 mm from the second surface of the lens. This implies that the PO propagators strongly agree with the ABCD matrix model.

3.4.2.4 Experimental Characterisation of Lenses

Since Mathematica and MODAL appeared to be agreeing it was decided to measure the phase of the radiation in real life using the Vector Network Analyser as a further independent verification. This was done as there was still a discrepancy between

MODAL, Mathematica and Dr. Yurchenko's predictions. The first half of the Gaussian Beam Telescope (as it is in MODAL) was setup in the lab the VNA lab.
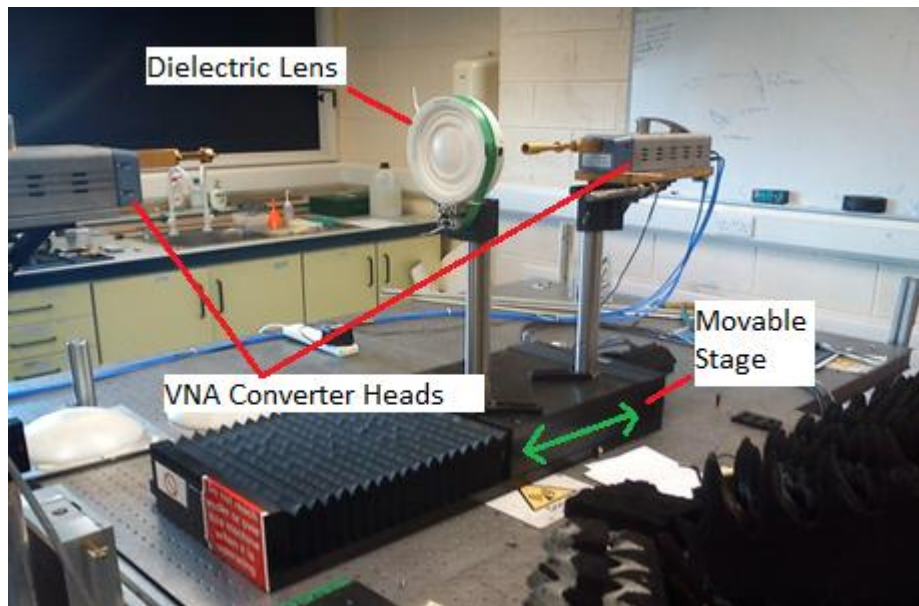

Figure 3-13: Experimental setup of Dr. Yurchenko's system for characterisation of Lens.

Figure 3-13 shows the setup used. The head on the right is effectively the emitting head in this setup (although both heads emit and detect) and uses the corrugated horn as a beam launcher. The source head is placed at a fixed distance of 125 mm from the first side of the lens. The head on the left uses a waveguide probe for detection. This head moves in a raster pattern (see section 1.3.2) to complete a scan whereby the magnitude and phase of the field is detected at each point on the scan. A text file is then exported containing coordinates of each point on the scan and the corresponding measured parameters chosen by the user.

The table that the lens and emitting head are mounted on is movable and is powered by a stepper motor. This table was utilised for automating the scan, as it was desired to measure several cuts of phase at different distances from the lens. A scan was setup so that the lens (and emitting head) would start at a set position close to the lens a scan across the centre of the lens was done, the lens moved, and the process repeated until the measurement was completed. Care was taken to ensure that the three components were aligned correctly in the system.

After the scan was completed, LabVIEW code was written by the author to extract each individual cut from the text file exported. The user was enabled to select a

section of the cut to focus on (as it was the phase curvature at the centre of the beam that was of interest). The points could then be plotted as desired.
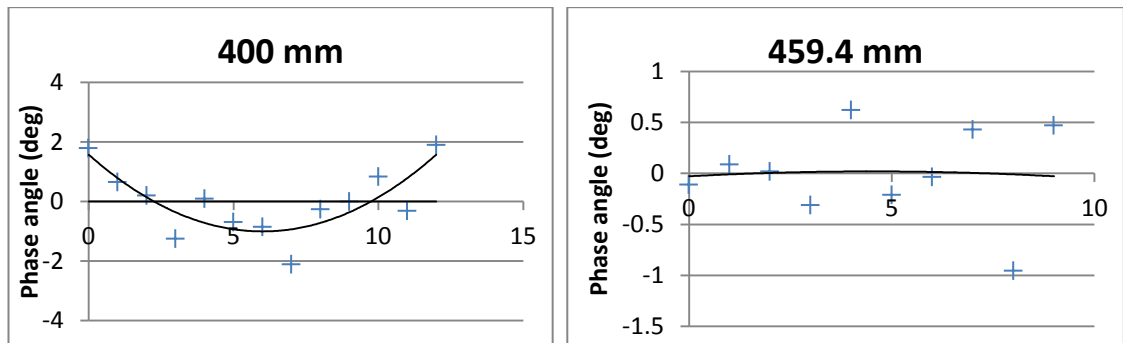

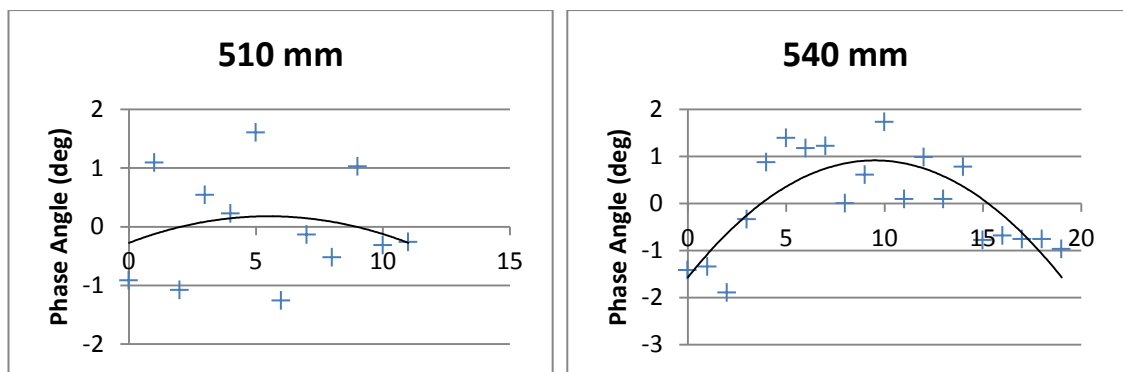*Figure 3-14: Plots of phase points at 400mm (left) and 459.4 mm (right) with trend line fitted.*

Figure 3-15: Plots of phase points at 510 mm (left) and 540 mm (right) with trend line fitted.

From inspection of the plots in Figure 3-14 and Figure 3-15 the variation in radius of curvature is clear and it was found that the flattest phase surface was at a distance of 459.4 mm from the second surface of the lens. This effectively verifies the model in Modal, as the position of the waist found using the PO propagators corresponds with the value predicted using ray transfer matrices and the VNA measurement. It is however clear that there is still a discrepancy between this value and Dr. Yurchenkos predictions. However for Dr. Yurchenkos measurements the requirements were only that the beam had a fairly flat phase curvature at 435mm (over a certain distance) from the lens so it is in fact possible that the actual beam waist position is at 460 mm from the lens.

3.4.2.5 Resolving Problems with Beams

Although the beam waist position had been located and verified using the PO propagation there was still clearly a problem with the beam drawings (which use an ABCD matrix method). It was decided to investigate the model definition of the lenses further to see if the problem lay there. As discussed in section 3.4.1 the section of the hyperbolic surface to be used was defined using an infinite cylinder as a bounding volume. It was decided to replace this with a finite cylinder as there was no need for the cylinder to be infinite. The length of the cylinder was set to half the thickness of the lens with the origin of the cylinder in the centre of the lens. In such a way that the cylinder just about encompassed the lens. It was apparent immediately the beams were more representative of the radiation as the beam was being focused as expected as illustrated in Figure 3-16.
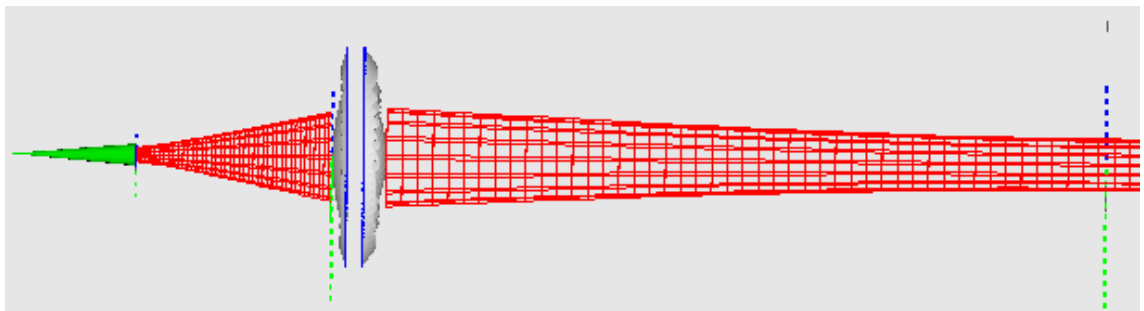

Figure 3-16: Image from MODAL'S 3D viewer depicting the new beam pattern.

It is thought that the problem lay with the fact that by definition the surface of a hyperbola has a corresponding "mirror image" surface. By not defining a finite cylinder the beam is intersecting and being transferred at the wrong surface but this is being plotted as emerging from the correct surface in the viewer. Conversely by using a finite cylinder the correct surface has to be used for the ray transfer solving the problem.

3.5 System Design

3.5.1 Implementation in MODAL

When implementing the optical system to be used, the tilting mirrors were placed at the global frame of reference. The other elements reference frames were defined with reference to this position i.e. transformations were performed on the objects with respect to this position. Although two tilting mirrors are used in the prototype the

model uses a single plane mirror that can be tilted by the user around the necessary axes as required. A single mirror was used as it was decided that it would provide an accurate approximation for modelling purposes.

Physical Optics propagators were used for propagating the radiation from the beam launcher through each component to the target plane. A plane mirror was placed at the target to mimic a perfectly reflecting object under study (as was to be the case for testing the prototype setup). PO propagators were then also used for propagation of the radiation field back through the system for detection at the transmitter receiver module. For ease of optimising the distances between elements, beams were implemented from one element to the next to highlight how the radiation was being focused instead of running the PO propagations each time. The beam width and waist positions could also be investigated. The area of object mirror was defined to be twice the beam width incident initially to allow the performance of the system to be tested i.e. the entire beam reflected.

Output planes were placed at the target screen and Transmitter Receiver module (Tx/Rx module) to investigate the radiation incident on these as desired. Contour Plots of phase and magnitude were created for each of these output planes. To investigate the power losses throughout the system, power metrics were created for each element and implemented in a list graph. Power loss metrics were also initialised at the target screen and Tx/Rx module to give an idea of power loss between source and these locations in the system.

3.5.2 Initial Design

When the modelling process was started it was envisaged that the two hyperbolic lenses would be adequate to fulfil the focusing requirements for the system. As it was necessary to focus the radiation from the source to the tilting mirror a lens was placed between the two in the transmitting receiving section. The second was placed between the tilting mirror and target screen.
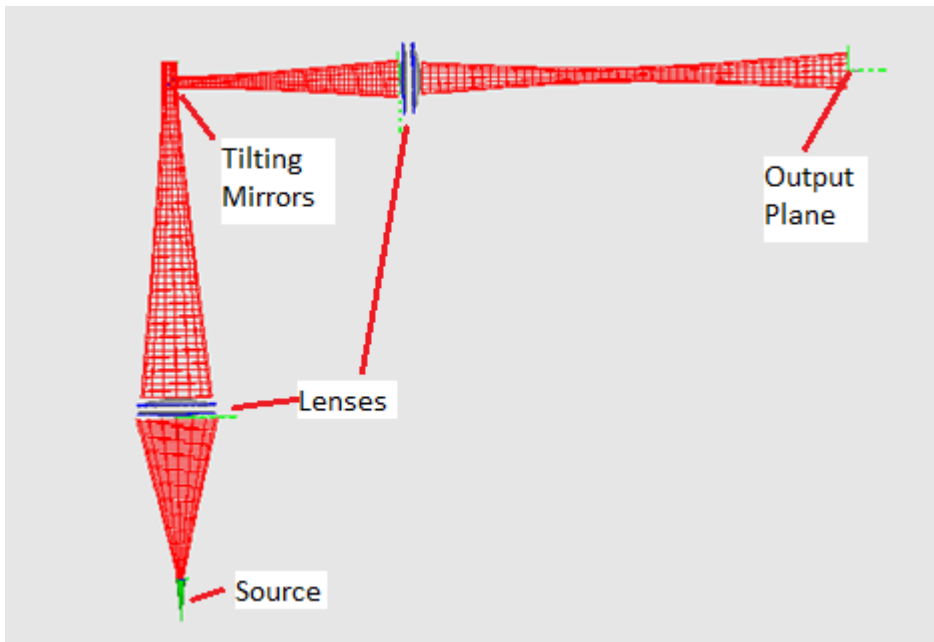
Figure 3-17: Screenshot from MODAL viewer of initial design.

However the shortcomings of this design soon became apparent. It is clear that a significantly large proportion of radiation was missing the lens (as the beams in Figure 3-17 only represent where radiation drops to 1/e, and hence don't fully represent all the radiation propagated). Furthermore the lens was incapable of focusing the radiation to a sufficiently small beam waist and hence truncation losses at the tilting mirror were substantial. With regards to the beam focusing section of the system, it was not possible to have a beam waist at the target at the required distance. When the system was investigated further it was found that there was a power loss fraction of 76.3% between radiation leaving the source and radiation incident on the detector.
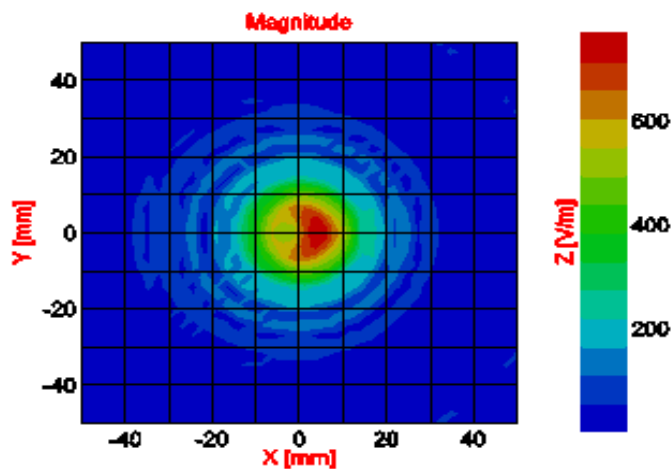

Figure 3-18: Magnitude of E-field component of field at target plane.

59

From the graphs and power values shown in Figure 3-18 the deficiencies of the system are apparent. It was clear that additional (or different) elements had to be used to meet the requirements desired.

3.5.3 Refinement of Transmitting Receiving Leg of System

When redesigning the transmitting receiving section all the components discussed in section 3.3 were considered. It was desired to collimate the radiation emanating from the source. The 500 mm ellipsoidal and 350 mm parabolic mirrors were disregarded as any source placed at a focus would produce too wide of a beam to be of any use. It was decided to use the smaller 150 mm parabolic mirrors. The source was to be placed at the focal point of the mirror so that the resulting collimated beam could be focused using a hyperbolic lens as illustrated in Figure 3-19. It was understood that this would produce a sufficiently narrow waist to focus all the radiation onto the tilting mirror eliminating truncation.
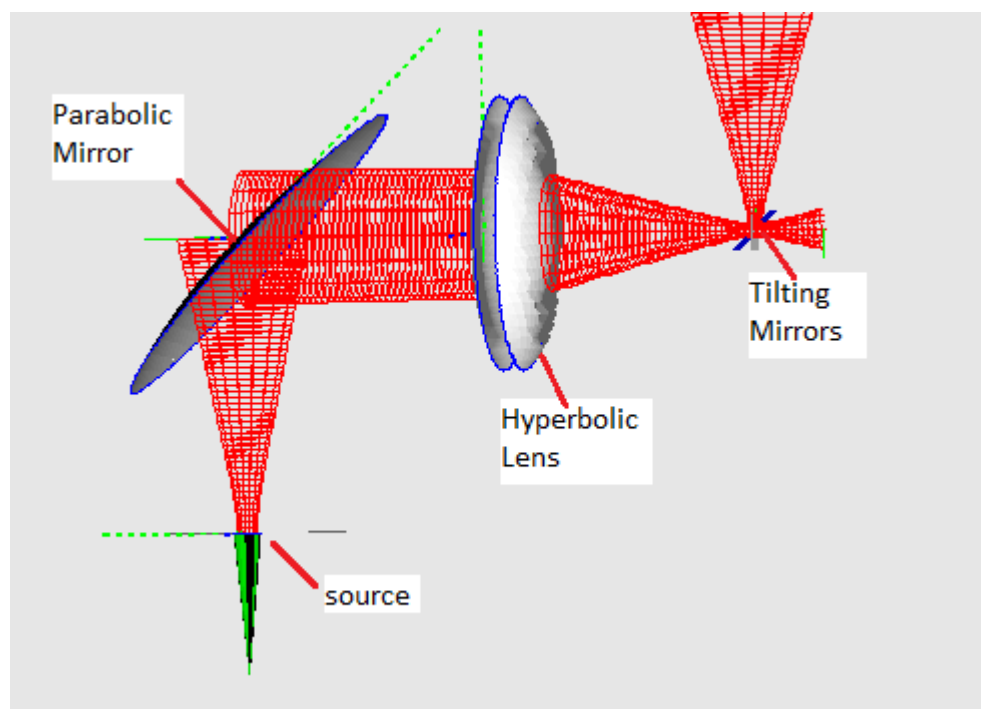

Figure 3-19: Re-designed first leg of system, incorporating 125 mm parabolic mirror.

To be at the focal point of the mirror the source was placed at a distance of 150mm from the point of interest on the mirror surface. As the beam was collimated the mirror to lens distance was arbitrary. To calculate the beam waist position the system

was modelled using ray transfer matrices and found to be 140.725 mm from the first side of the lens. The system was then setup in MODAL with these dimensions.
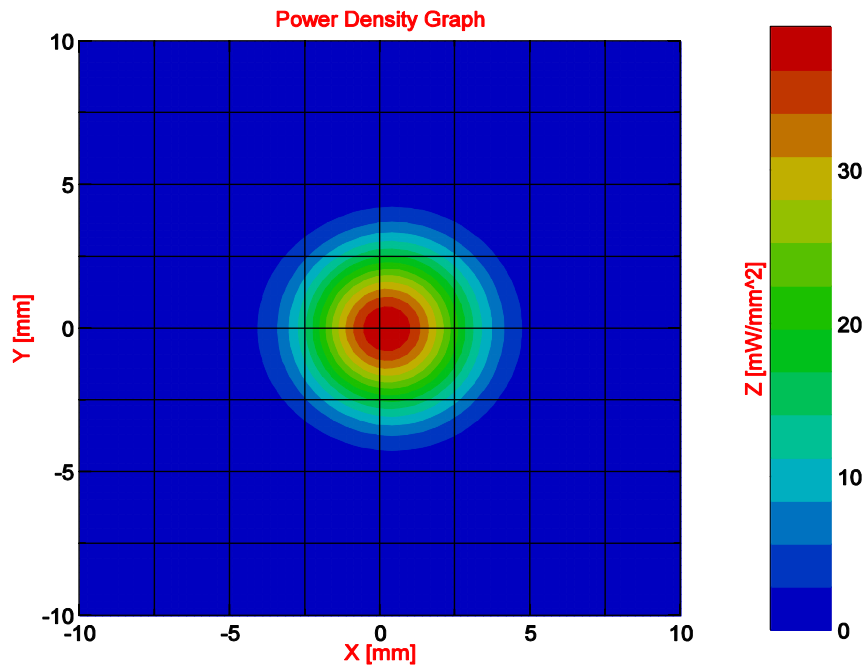

Figure 3-20: Power density graph of beam at tilting mirror position.

It is clear from Figure 3-20 that the beam power is concentrated well between the limits of the 20x20mm mirror. From the use of Power metrics it was found that 92.4% of the power was being coupled from the source to the tilting mirror a vast improvement on the previous system.

3.5.4 Design for beam focusing section of system

Now that the transmitting receiving section design was finalised, a viable design for the beam focusing section had to be finalised. All the elements as discussed in section 3.3 were considered, however once again the 350 mm parabolic and 500 mm ellipsoidal mirrors were discounted as a wide beam would be produced at the mirror surface if tilting mirrors were placed at the focus. Also if another element was used in conjunction with these to collimate the beam before incidence on the mirror this would also prove an ineffective solution. This is because the mirrors are designed to focus the radiation onto a particular point, which is acceptable for non tilted beams in the straight through position. However with tilted beams the radiation becomes skewed and will not focus a circular point onto the target. Also truncation becomes an

issue when the beam is tilted using the tilting mirrors. For these reasons it was decided to use the second hyperbolic lens to focus the radiation emanating from the tilting mirrors to a beam waist at the target as illustrated in Figure 3-21.
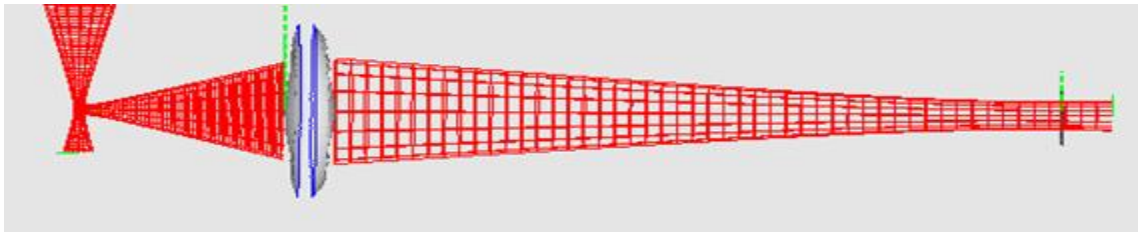

Figure 3-21: Screenshot from MODAL viewer illustrating design of beam focusing section of scanning unit.

To achieve the desired beam width at the target it was determined that the first side of the lens should be placed at a distance of 140 mm from the tilting mirror position. This position was chosen as not only did it provide an adequately wide beam width at the target, it was close enough to the tilting mirrors to minimise truncation losses at the lens as the beam is tilted. However compromises had to be made on scanning range. Initially a target distance of 1 meter was desired, however with this setup a distance of 355 mm was achieved. As the project was essentially to be a proof of concept of the tilting beam approach the concession on target distance was considered acceptable. Due to the nature of the lens used the scanning range requirement outlined in section 3.2 also had to be altered as the lens was not wide enough to focus radiation at large tilting angles.

To investigate power losses throughout the system radiation was then propagated through the whole system i.e. from source to target and then back to the Tx/Rx module. Power metrics were used to calculate percentage power at each component.

Illumination Phase	Percentage (Watts)	Reflection Phase	Percentage Power
Source	1	Object Mirror	.8049
Lens 1	.9789	Lens 2	.7509
Tilting Mirror	.8945	Tilting Mirror	.7239
Lens 2	.8624	Lens 1	.6609
Object Mirror	.8049	Tx/Rx module	.6350

Figure 3-22: Table of Power values for various components in the system.

It can clearly be seen from ꜱꜰ Figure 3-22 that there is only a 36.5% power loss throughout the system. Given the envisaged sensitivity of the detection system this was deemed to be acceptably small.

3.6 Summary

In this chapter the design of the system to be used has been outlined and modelling results have been presented. The implementation of the lenses in MODAL has been discussed. Also work carried out on the successful verification of the lenses has been outlined in detail.

In section 3.5 the deficiencies of the initial design are presented and the thought process and results behind the redesign of each section of the system outlined. Although concessions had to be made on scanning distance and area the design was expected to serve the purposes desired for a proof of concept adequately.

4   Chapter 4

Development and testing of Prototype setup.

4.1   Introduction

In this Chapter the work involved in the development of the actual prototype is outlined. Details of the equipment used are presented and the approach used for the implementation of the Transmitter Receiver discussed. The prototype setup is discussed and details of the signal measurement system outlined. Details will be provided of the development of the motion control system. This Chapter will also discuss the various modulation techniques and in particular focus on the development of a phase dielectric for the reduction of reflections. A brief discussion of the techniques used for the alignment of the system will also be given

Results of the testing of the system are also discussed in detail, starting initially with the results of the first leg testing and comparison with MODAL models. The results of the first prototype scan are then presented.

4.2   Sources and Detectors

4.2.1 Sources

The radiation source used for this prototype was a Gunn Diode source currently available in the research group's lab. A Gunn Diode is essentially a two terminal negative differential device which when coupled to a suitable resonator, generates RF power. The Gunn Diode is made from a doped n-type semiconductor with two more heavily doped regions surrounding a uniform region of n doped material. The heavily doped regions act as electrical contacts to another device.

The active region of the Gunn Diode is the central region, because it is so thin it experiences extremely high electric fields when a voltage is applied across it. When the voltage rises above the threshold voltage of the diode current can flow across it. Due to the negative differential resistance effect of the diode the current values increase

however as the voltage increases further the differential resistance increases resulting on an effective cap on the current produced, see Figure 4-1.
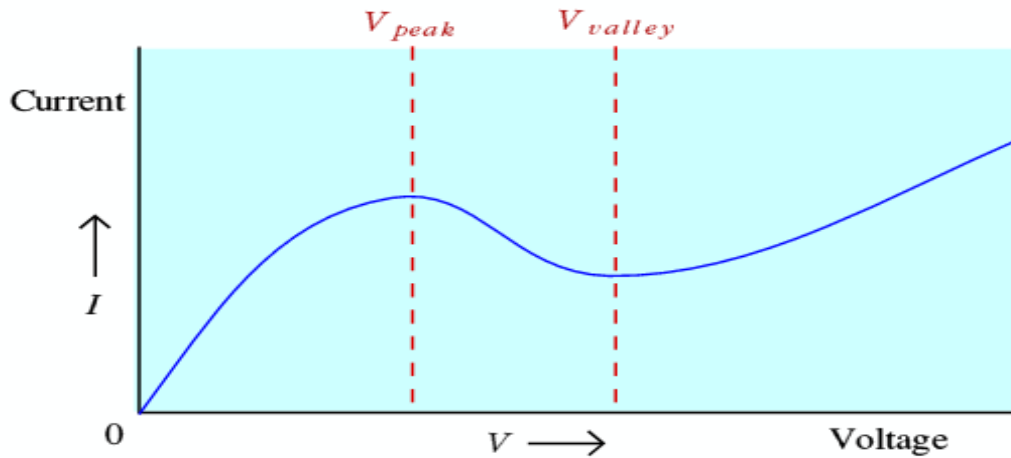

Figure 4-1: Graph of Current as a function of Voltage provided illustrating negative differential resistance region. Current flow increases only when correct voltage is provided. (30)

When combined with an oscillator circuit the negative differential resistance can be used (by adjusting the Voltage) to counteract the AC resistance of the circuit in such a way that EM radiation can be created continuously. This project uses an off-the-shelf radiation source where the diode is mounted in a resonant cavity and the EM radiation can exit through a WR10 waveguide. The cavity is tuneable through two micrometers one for tuning the frequency and the other maximising power output. Calibration sheets for setting the power at a certain frequency were provided by the manufacturer.

Figure 4-2: Picture of Gunn Diode source used with power micrometer on top and frequency tuner on side.

65

As the Gunn Diodes available were quite a few years old (≈ 10) and could have drifted it was necessary to re-calibrate the sources. This was done as the frequency produced had to be well understood for operation with the Transmitter Receiver module (discussed in next section). The setup in Figure 4-3 was used for the calibration.
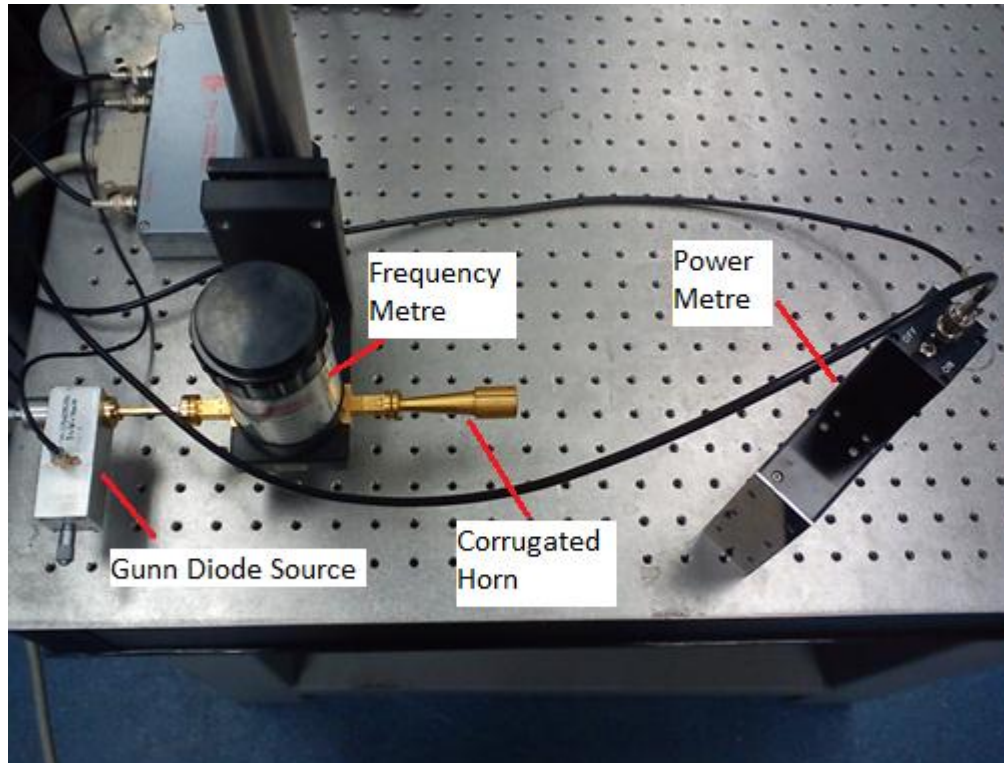

Figure 4-3: Setup for calibration of Gunn Diodes.

In this setup we have the source under test connected to a Farran Technologies Frequency meter which if set to a certain frequency will only allow radiation of that frequency to pass. This was tested and calibrated using the VNA in the department. The power emitted was measured using a Thomas Keating Ltd Absolute Power Meter. The frequency micrometer was set to its lowest value and the frequency meter adjusted until radiation passed through and hence the frequency corresponding to this micrometer position recorded. The Power micrometer was then adjusted until power reaching the Power meter was maximised. The Power meter is placed at Brewster's angle ($55°$) with respect to the plane perpendicular to the direction of incident radiation. This is to ensure that as little radiation as possible is lost due to reflection upon hitting the detector (maximum transmittance).

The source chosen was the Ostek OTGW 10 (s/n 10B – 001) source as it had a frequency range centred on 100 GHz ($95 – 105$ GHz range) and had the highest power

output ~15 mW. It requires a bias voltage of 4.20 V and draws a current of ~725 mW depending on ambient temperature. One must take care not provide a voltage of over 4.70 V to the diode as any voltage overshoot could overheat and permanently damage the diode. The manufacturer's guidelines state that the device should be connected to a power supply which has already been turned on and whose voltage output is reduced to zero. The voltage can then be increased to the desired bias voltage.

4.2.2 Crystal and Cavity Detector

The detector mechanism is a rectifier diode mounted in a resonant cavity. The cavity resonance is tuneable by means of a sliding back short attached to a micrometer screw. The sliding short allows the detector to be optimised at any frequency in the range 70–120 GHz. The detector is a Dorado CD-10 detector (s/n 040310). The detector at these frequencies works like any other rectifier diode and produces a DC voltage proportional to the incident signal energy. (26) The only way to make these devices rectify at such high frequencies is to keep the junction small < 1 μm. These diodes are formed by a gold whisker contacting a Gallium Arsenide substrate. The metal/semiconductor junction forms a Schottky diode. (26) The diode contained in the CD10 detector is supplied as a pre-contained device illustrated in Figure 4-4.

Figure 4-4: Image of CD10 crystal detector used.

4.3 Transmitter-Receiver module

As discussed in section 1.4.1 the system was to be an integrated active imaging system and would use a transmitter receiver module for the illumination of the target and detection of radiation reflected back through the system. See Figure 4-5 below.
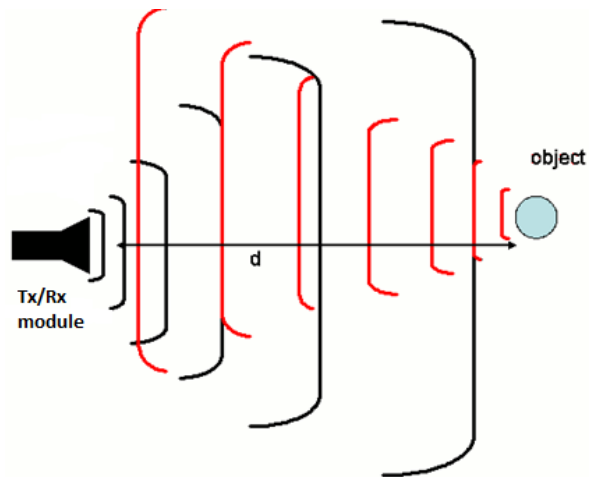

Figure 4-5: Highly schematic representation of operation of Tx/Rx module. Radiation is emitted and reflected radiation picked up by the detector.

To enable the transmitting and receiving action of the module it was decided to use a 3 port circulator component. A circulator is a ferrite device which operates by coupling all the radiation inserted to a port in one direction only.
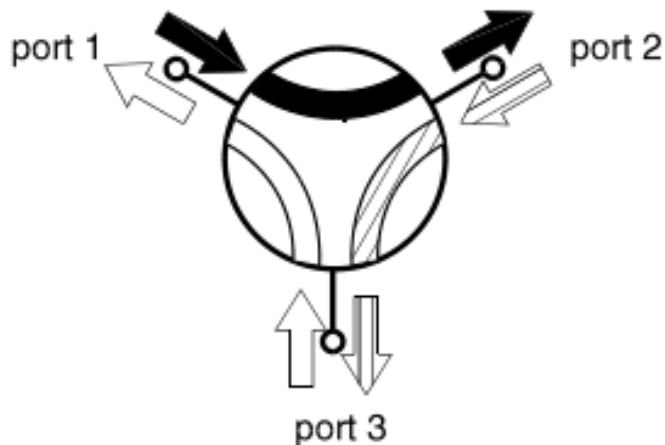

Figure 4-6: Diagram of operation of a 3-port circulator circulating in a clockwise direction.

It is a non reciprocal device in that predominantly energy entered in port 1 exits port 2, energy into port 2 exits port 3 and energy in port 3 exits port 1. Conversely ports 2&1,

1&3 and 3&2 are decoupled meaning energy cannot flow between them as illustrated in Figure 4-6. In a reciprocal device the same fraction of energy that flows from port 1 to port 2 would occur to energy flowing in the opposite direction, from port 2 to port 1. The circulators can be made to circulate either CW or CCW. A circulator is sometimes called a duplexer meaning that it duplexes two signals into one channel (i.e. transmit and receive into an antenna). (31)

The aim was to connect the source via a short waveguide to port 1, the antenna (corrugated horn) to port 2 and the detector to port 3. In such a way that radiation from the source passes out through the antenna but as ports 1 and 3 are decoupled no radiation passes directly to the detector. The radiation then passes through the system and some of it will be reflected from the target back through the system to the antenna horn. This is then circulated from port 2 to port 3 where it is picked up by the detector and ports 2 and 1 are decoupled. The Tx/Rx implementation is illustrated in Figure 4-7.
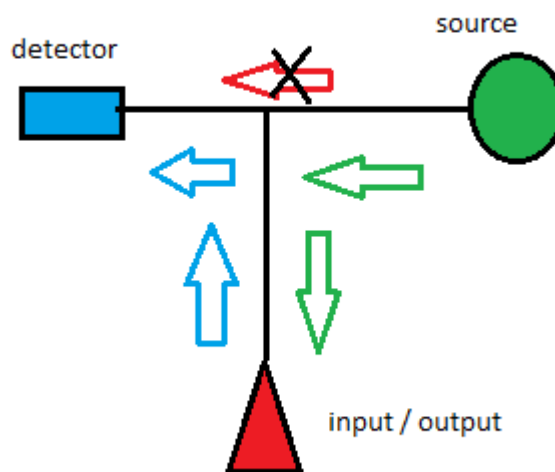
Figure 4-7: Outline of operation of Transmitter Receiver module.

The circulator utilised in this project was a Farren Technology ftl2892b and was ordered to have an optimal performance at 100 GHz and to circulate in a clockwise direction. The port connections were WR10 waveguides. An ideal circulator would have 0 insertion loss between coupling ports, and infinite isolation between non coupling ports. As the device is not ideal, the performance of the device was measured

using the VNA (see Table 4-1). When investigating two ports one converter head was placed at each port the losses between the two heads could then be measured.

Frequency (GHz)	Isolation (dB)			Insertion Loss (dB)		
	$2-1$	$3-2$	$1-3$	$1-2$	$2-3$	$3-1$
98.5	18.48	23.52	22.69	.77	.87	.74
99.0	21.17	21.20	26.88	.71	.86	.73
99.5	25.76	21.57	28.58	.77	.90	.76
100.0	35.33	25.05	31.26	.71	.67	.74
100.5	28.06	38.27	34.50	.78	.93	.64
101.0	21.16	22.97	24.18	.81	1.10	.77
101.5	17.1	16.22	17.82	.97	1.33	.95

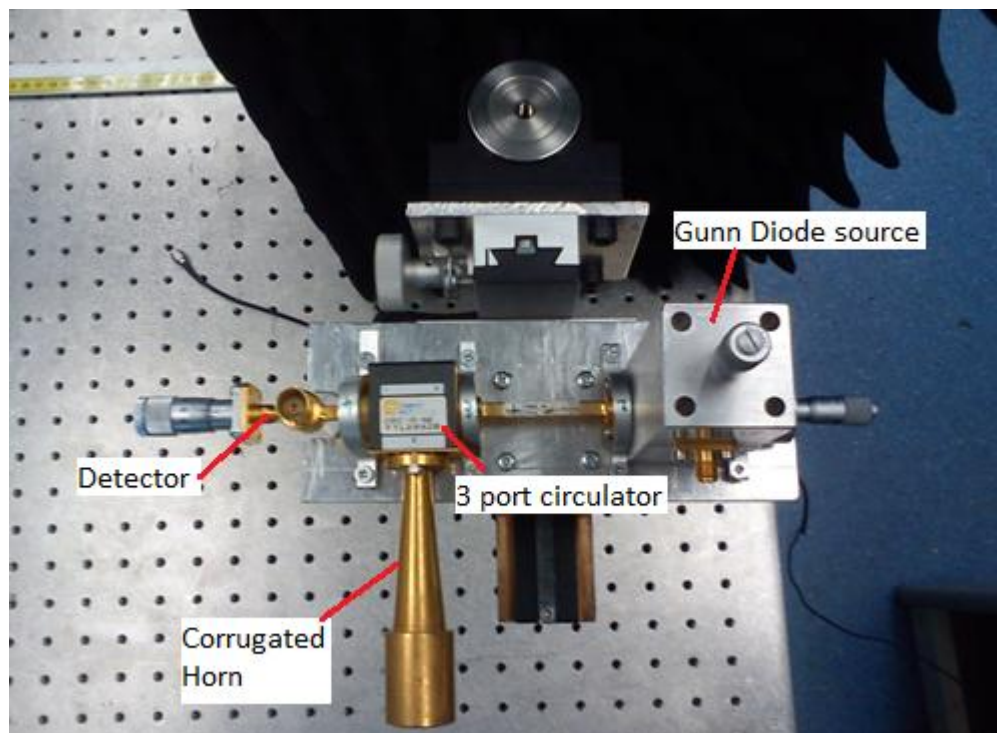*Table 4-1: Results from testing of circulator*

Figure 4-8: Picture of assembled Tx/Rx module.

In Figure 4-8 above the completed module can be seen with the Gunn Diode source on the right the detector on the left and the corrugated horn antenna attached to the third port. The module was mounted on a metal plate for integration into the system

and to aid alignment. This plate was then mounted on a 3 dimensional translational stage for the purposes of fine tuning the system if necessary.

4.4 Retrieval of Signal

4.4.1 Signal Recovery

As discussed above using the Tx/Rx module approach any radiation reflected from the target back through the system is fed into the detector. One difficulty with this method is that a weak signal might be "hidden" in a large amount of noise mainly due to ambient THz radiation due to the sun. Therefore a lock in amplifier is required to filter the desired signal form the noisy background. The lock in amplifier operates by utilising a phase locked loop. If a situation exists where a reference frequency is provided to a lock in amplifier, (either by an internal oscillator or an external signal) a signal can be "pulled" from noise if the signal has a phase directly related to the phase of the reference frequency. This is usually achieved by modulating the signal at the reference frequency either by modulating the source of the signal or mechanically chopping the source. In this setup in Figure 4-9 the source is pulsed by a generated square wave signal and this is also provided as a reference to the lock in. When using a beam chopping technique the chopper is placed between source and detector and reference provided to lock in amplifier without pulsing the source. The lock in amplifier used in this project is an AMETEK Signal Recovery (model: 7265).
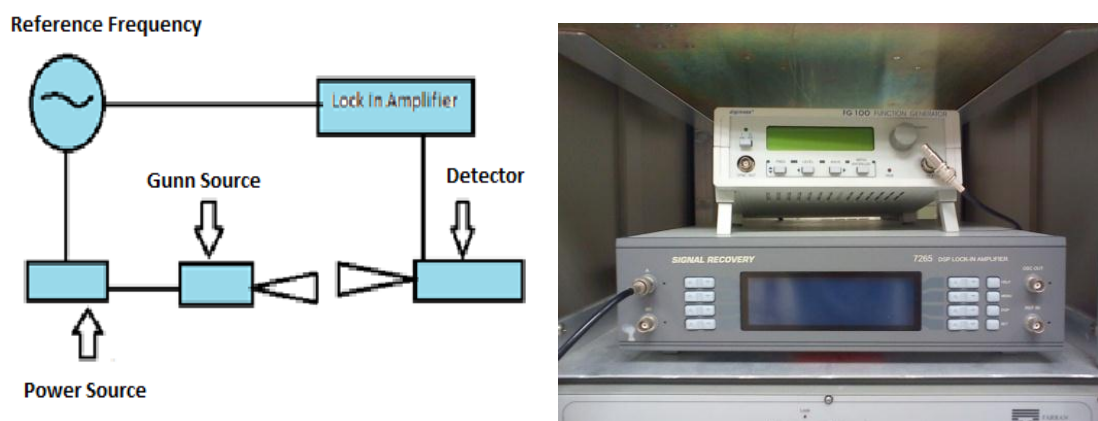

Figure 4-9: Illustration of signal recovery system used (left) and lock in amplifier and function generator (right).

4.4.2 Modulation Techniques

In the configuration shown in Figure 4-9 the signal to be detected is being modulated by pulsing the Gunn diode source by applying a square wave to the power supply. The problem with this approach is that the radiation entering the circulator (through port 1) from the source is pulsed at the reference frequency. Any leakage from the source through to port 3 (the detector port) will be picked up by the lock in amplifier. This reduces the dynamic range which is essentially the signal to noise ratio (ratio of base signal with radiation from antenna being absorbed by perfect absorber to signal reflected from target). The higher this ratio the easier it is to image a target as lower signals can be detected. To investigate this further the Tx/Rx was tested with various media in front of the antenna. The base signal was recorded in free space initially and subsequently with absorber in place. The dynamic range was then investigated by reflecting the radiation using a metal plate placed at different distances from the horn and measuring the signal retrieved.

Description	Signal (mV)	Dynamic Range (dB)
Free space	1.4	
TK absor (0 cm)	1.39	
Tk abs (10cm)	1.39	
TK abs (20cm)	1.4	
Metal Plate (0 cm)	272.2	194.42
Metal Plate (10cm)	12.5	8.92
Metal Plate (20cm)	4.5	3.75
Metal Plate (30cm)	2.5	1.75
Metal Plate (40cm)	1.75	1.28

Table 4-2: Table of results presenting dynamic range of source modulation technique.

It is clear from the Table 4-2 that the unwanted leakage from the source through to the detector is 1.4 mV. It was thought that it may be possible to reduce this by using a mechanical modulation method. By this method a standard optical chopper and

controller is used to modulate the signal by chopping it at the reference frequency which is also passed to the lock in amplifier. With this method the chopper is placed in front of the horn antenna and the signal modulated at this point. The advantage of this method is that the source is not modulated directly and as a result any leakage through to the detector will not be registered by the lock in amplifier. However as the chopper blades are metal any reflections back to the Tx/Rx module are modulated at the reference frequency and so can be picked up by the detector lowering the dynamic range. This effect can be reduced by placing the chopper at an angle with respect to the horn aperture. This approach was tested to see if an optimal situation could be obtained for increasing the dynamic range whilst chopping the beam effectively (see Figure 4-10). The modulator is placed at an angle with respect to the horn face. A movable metal plate is mounted in a translational stage and surrounded by absorber do minimise spurious reflections. The chopper was also placed at different distances from the horn and a movable metal plate placed behind the chopper. This was so that the effects of dynamic range could be compared for the same situations as were tested with the source modulation situation previously outlined.
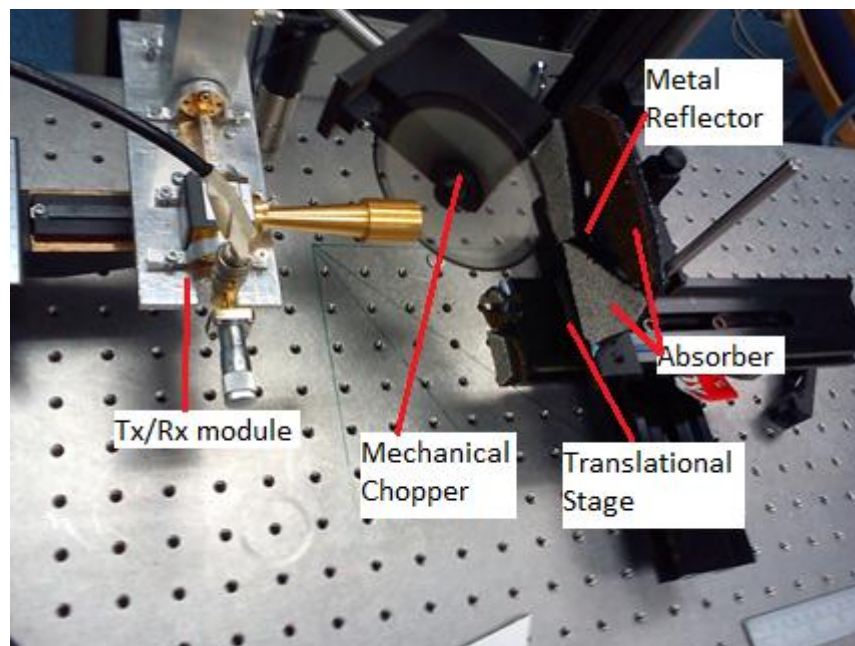

Figure 4-10: Picture of setup used for investigating the effect of different situations on the dynamic range.

Readings were taken with the chopper 1 cm and 5 cm from the horn. Initially Readings were taken with no metal plate in place first to measure reflections from the chopper

73

alone (i.e. base signal highlighted in red in Table 4-3). It was found that at angles 0°, 15° and 30° reflections from the chopper were quite high and so dynamic range too low. However at 45° the base signal drops to 0.08 mV at 1 cm and 0.06 mV at 5 cm which are considerably lower than the base signal using the first modulation method of 1.4 mV. As a result of this the dynamic range increases compared with the situation utilising the source modulation approach.

	Description	0 deg (mV)	15 deg (mV)	30 deg (mV)	45 deg (mV)	DR (45 deg)
1cm	Free Space	152.82	63.22	7.96	0.08	
1cm	Metal Plate (0cm)	30.0	22.32	33.04	18.97	237.125
1cm	Metal Plate (5cm)	130.4	8.7	27.81	9.61	120.12
1cm	Metal Plate (20cm)	146.2	15.12	5.14	4.81	60.12
1cm	Metal Plate (30cm)	150.3	61.20	5.54	2.86	35.75
5cm	Free Space	26.48	9.22	0.10	0.06	
5cm	Metal Plate (0cm)	14.65	9.52	16.98	6.12	102
5cm	Metal Plate (5cm)	18.97	9.75	18.15	4.62	57.75
5cm	Metal Plate (20cm)	22.30	15.61	10.12	3.01	37.62
5cm	Metal Plate (30cm)	25.80	19.51	3.51	1.25	20.83

Table 4-3: Table of results from testing mechanically chopped setup. Results of measurements taken with chopper angle of 45°and corresponding dynamic range are highlighted in green.

Although the base signal obtained using the mechanical chopping was a substantial improvement on using the function generator, it was thought that it would be possible to decrease the reflections further. This was to be done using a dielectric modulator in place of the metal one. The idea was that if the modulator was not made of metal there would be a large reduction in reflections. The modulation itself was achieved by

creating a phase shift so that radiation passing through certain sections of the modulator is 90° out of phase with respect to the other sections. A 90° phase shift was required upon transmission through the dielectric as the radiation has to travel twice through the dielectric. Once when travelling from the module to the target and a second time on its way back resulting in a 180° phase shift as required. As discussed in section 3.4.2 above by incorporating a region which has a refractive index value greater than 1 into the system a phase delay is implemented. This theory was used to create a desired phase delay for the dielectric modulator. The modulator was designed in a similar fashion to the design of the mechanical chopper with sections of the face of the circle being thicker than the other sections. The phase delay was achieved by making the dielectric at the thicker sections a specified thickness thicker than the other sections (see Figure 4-11). As the modulator was to be rotated using the same motor as was used for the mechanical chopper it was necessary for the discs to have the same profile. This is because a photo gate was used for picking up the reference frequency, which imposed some limitations in terms of size and thickness on the design.
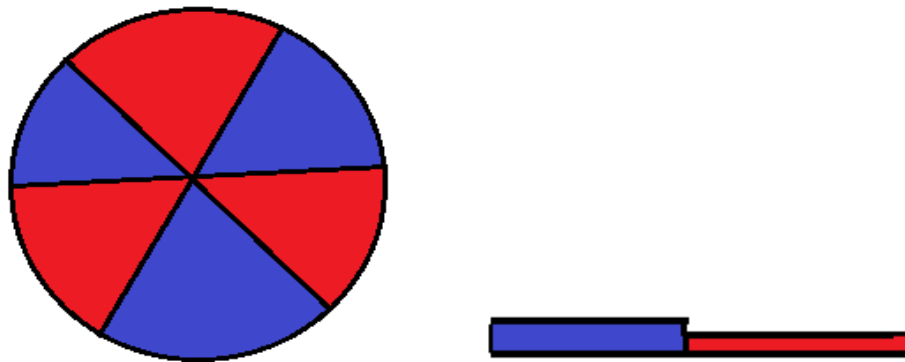

Figure 4-11: Face profile of dielectric chopper to be used (left) and side profile view (right) illustrating design of modulator.

In section 3.4.2 it was shown that the phase change resulting from propagation through a dielectric (compared with free space) is represented by:

$$\Delta\emptyset = \emptyset - \emptyset_0 = (2\pi \frac{d}{c}(n-1))f \qquad (4.1)$$

Since it was desired to have a phase change of 90° then this becomes

$$\frac{\pi}{2} = \left(2\pi\frac{d}{c}(n-1)\right)f. \tag{4.2}$$

Since the modulator was machined from Teflon a refractive index value of 1.6 was used as this is the refractive index at 100 GHz. (2) Solving this expression leads to a value of d of 1.25 mm i.e. the thicker regions have to be 1.25mm thicker than the thinner regions to achieve the required 90° phase shift upon transmission. To minimise reflections further it was decided that the modulator would be mounted at a 10° angle with respect to the horn aperture. Accounting for this change the thickness requirement became 1.231 mm. The Modulator was then manufactured using a milling machine by Mr. David Watson.
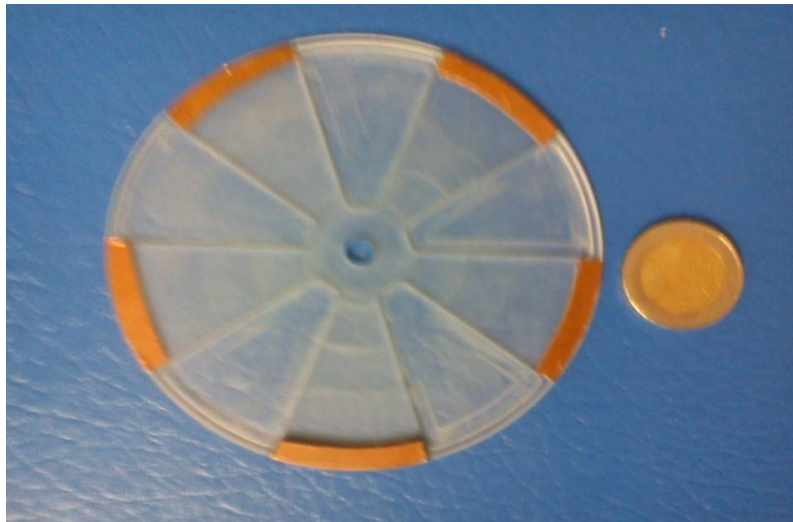

Figure 4-12: Picture of dielectric chopper with metallic tape used for pulsing photo gate used for determining reference frequency.

After manufacturing the three modulation techniques were then tested and compared using the setup pictured in figure 4-10 above. It should be noted that although the same was setup was used in each case, these measurements were taken at a different date to the results presented in Table 4-2Table 4-3 with a different setup of Gunn Diode.

Modulation Method	Base signal (mV)	Metal Plate (mV)	Dynamic Range
Function Generator	.21	84.09	365.6
Mechanical Chopping	.01	16.5	1650
Phase Modulation	.0037	4.69	1267

Table 4-4: Results comparing the three different modulation techniques. The phase modulation technique is not effective when strong signals are being used.

It is clear from Table 4-4 that the base signal is decreased by the phase modulation technique however, the signal picked up with the plate in place is also reduced resulting in a lower dynamic range, than with the mechanical chopping technique. The effect of using the phase modulator in situations with strong signals can be described as follows. Consider a situation where we have a signal *s* which is coherent with the source at the received signal (e.g leakage through the circulator). Assume there is a base signal *n* inherent in the system which is modulated at the same frequency as the signal, this situation is represented in the phasor diagram illustrated in Figure 4-13.
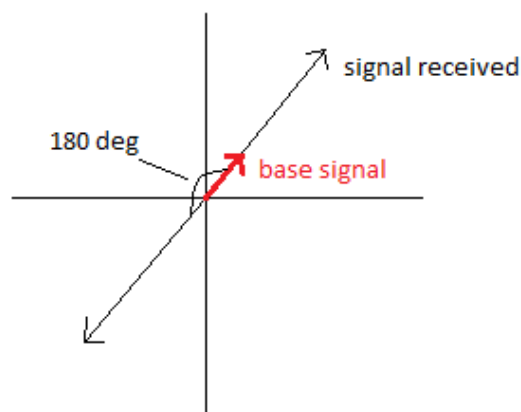

Figure 4-13: Phasor diagram illustrating situation involving phase dielectric modulator.

As the dielectric rotates it modulates the signal by 180° (flips the phasor 180°), the result is that the measured signal $\tilde{s}$ is given by the equation

$$\tilde{s} = |s + n| - |n - s| \cdot \qquad (4.3)$$

It is clear from this expression that if there is a large difference between the length of the signal phasor and the length of the base signal then the measured signal is lower where as if the base signal is relatively large compared to the received signal then a larger signal is recovered. For example consider a situation where there is a base signal of $0.1s$ and another situation where the base is $0.9s$. Substituting into equation 4.3 yields a signal recovered of 0.2 for the first situation and 1.8 for the second situation. It is for this reason that the testing above yielded a weak signal as the received signal is strong compared to the base signal. However in a situation where the base and received are comparable then the signal recovered is larger. As will be discussed later,

the phase dielectric can be used with this prototype as the signal being detected is much weaker in comparison with the base signal.

4.5 Implementation of transmitting receiving stage

4.5.1 Alignment Procedure

The next step in the development of the prototype was to actually position the elements of the system on the optical bench to be used. This required quite accurate positioning to not only minimise power losses but also to ensure that the beam is propagating through the system as modelled in MODAL. This section outlines the procedures used to align the elements and verify the setup.

The first element that was placed in the system was the parabolic mirror. This mirror was mounted on a cylindrical pole. A bracket was fixed to the back of the mirror which slid onto the pole in such a way that the mirror could be slid up and down the pole and rotated around the pole. The pole could be then screwed into the optical bench. The bracket was then rotated until the mirror plate was at an angle of 45° with respect to the plane that the aperture of the horn was placed at (see Figure 4-14). The mirror was then positioned such that the centre of the mirror surface was at the same height as the horn.
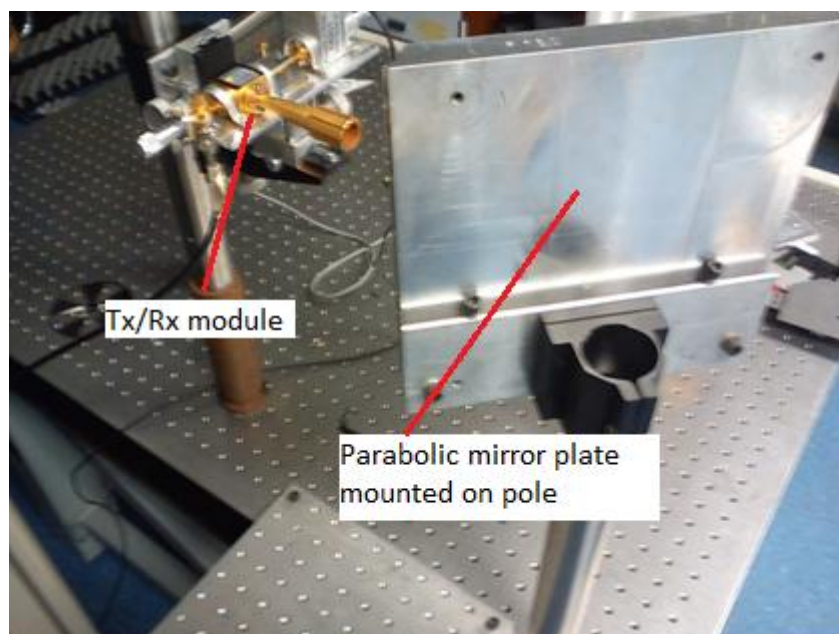

Figure 4-14: Picture illustrating mount used and relative position with respect to Tx/Rx module.

There was some ambiguity about the location of the "point of interest" on the mirror as it was known that it wasn't simply in the centre of the machined parabolic surface. Also it was uncertain whether the mirror was designed so that the focal point was 150 mm from the plate that the mirror was machined from or 150 mm from the point of interest on the mirror surface. As a result the mirror properties had to be investigated further.

A collimator (taken from a spectrometer) was used to focus light from a torch into a collimated beam which was incident on the parabolic surface. The idea was to experiment with this setup until the point of interest was found. In theory if a collimated beam is incident on the mirror at the correct location then the beam should come to a focus 150 mm and at $90°$ to the incident beam. The collimated beam was scanned over and back and a screen used for viewing the focused beam. Eventually after a series of trial and error attempts, the focal point was found at 150 mm from a point on the parabola at an angle of $90°$. The horn aperture of the Tx/Rx module could then be placed at this position.

As the actual phase centre of the horn is ≈ 5 mm behind the aperture the horn was moved forward 5 mm to account for this. To ensure that the horn aperture was positioned at the correct angle (normal from aperture plane at $45°$ to point of interest on mirror) the horn was adjusted on the Tx/Rx mounting plate.

To ensure that the alignment of these two objects was correct a small plane mirror was placed at the horn aperture and a larger plane mirror placed across the metal plate of the parabolic mirror. The author then placed his eye at the location of the beam waist of the first leg. The alignment was verified as an image of the author's eye could be seen meaning that the parabolic mirror was at $45°$ with respect to the aperture plane as desired.

The final part of the first leg setup involved the positioning of the hyperbolic lens. The lens was placed on a shelf attached to a bracket which was then fixed to a cylindrical pole. Care was taken to ensure that the shelf was perpendicular to the axis of the system by placing a flat piece of metal perpendicular to the axis and making sure that the edge of the shelf was parallel with this. This was achieved by using a metal bracket bolted to the optical table. The bracket was also adjusted to the proper height so that

the centre of the lens was at the same height as the horn aperture and by extension the point of interest on the parabolic mirror.

The lens then had to be placed at the correct position on the shelf. The centre of the lens was marked and the lens positioned so that the centre coincided with a line straight down through the point of interest on the mirror as illustrated in Figure 4-15 and Figure 4-16.

Figure 4-15: Setup used for positioning lens mount (left) and technique used for positioning lens on shelf (right).

Figure 4-16: Final arrangement of aligned first leg of system.

4.5.2 Verification of transmitting receiving stage alignment

The next step in the process was to compare the performance of the first leg of the prototype to what was expected from the model in MODAL. To investigate the nature of the beam at the beam waist position (where the tilting mirrors were to be placed) a 3D translational stage was created to scan this region of the system. A second but identical horn detector was mounted on the stage and the lock in amplifier used to detect the signal. The horn was placed at the same height as the source horn and a 2D sweep was carried out around the predicted beam waist position using the apparatus in Figure 4-17.
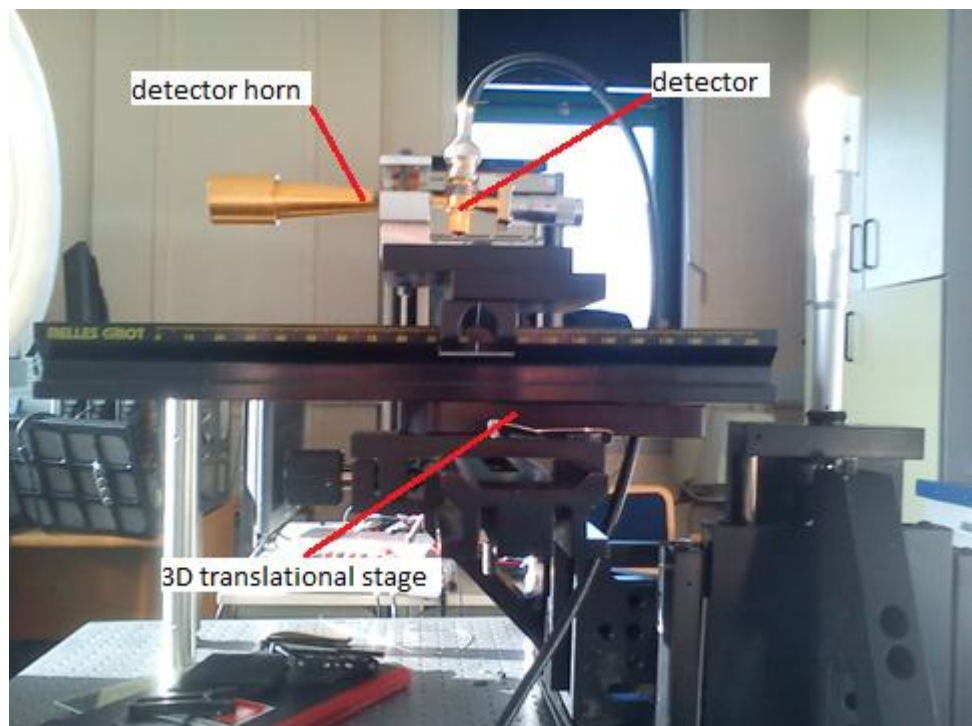

Figure 4-17: 3D translational stage created to investigate beam around predicted beam waist position.

As discussed in section 3.5.3 the beam waist position of the transmitting receiving section was found to be 140.725 mm from the first side of the lens. The results from the 2D scan were recorded in a text file which was then imported and analysed using code written by the author in LabVIEW. The cuts across the beam were plotted (see Figure 4-18). To find the beam waist position a fitting routine was applied to each cut to determine the weighted standard deviation of that cut (see Figure 4-19). The idea of the weighting is that, as each point is being fitted it is compared to the central peak value of the cut and values that are small in comparison are given less weight in the standard

deviation calculation. The result is that if values on the extremities of the cut are small compared to the peak they factor less in the standard deviation of the cut.
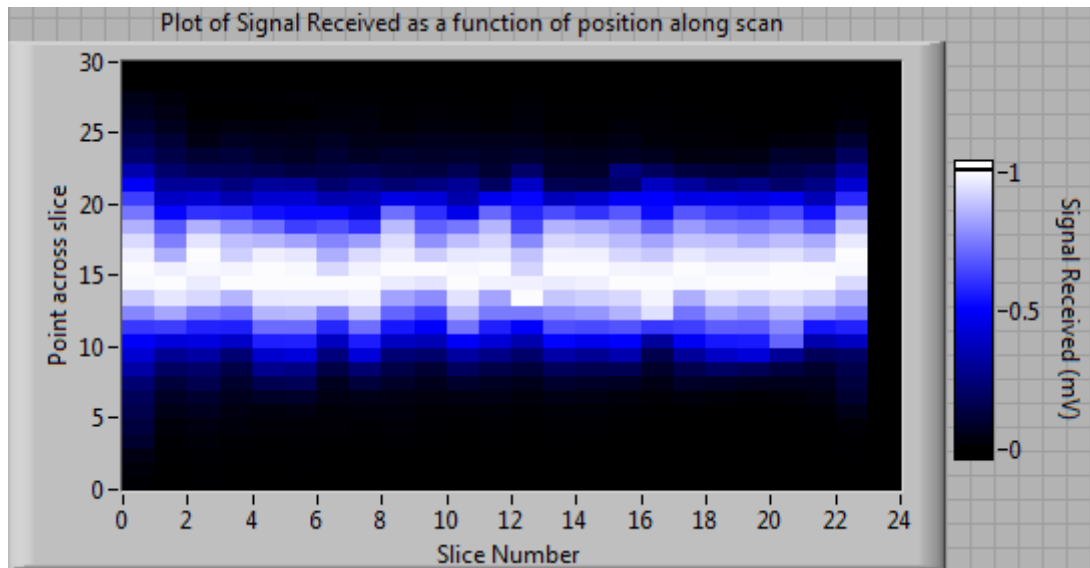

Figure 4-18: Plot of data obtained from 2D scan illustrating beam around beam waist position. The variation of the width of the beam is a result of the effects of standing waves in the system.
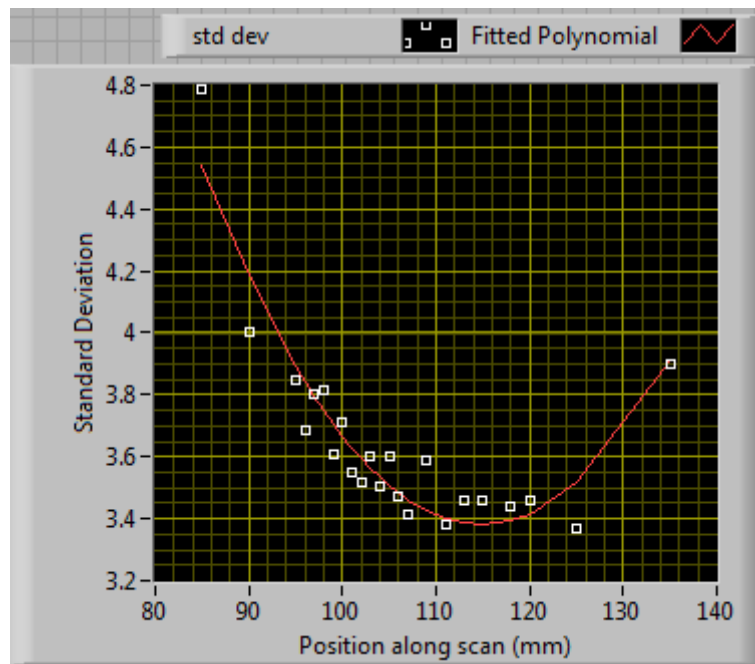

Figure 4-19: Plot of weighted standard deviation values for each cut as a function of position along scan.

It should be noted that the position along scan on the x-axis of the graph on Figure 4-19 referrers to the position on the scale of the 3D translational mount. This must be transformed to have a sensible position with respect to the first side of the lens. Taking

this into account the beam waist position from this scan is determined to be at a location of 138.6 mm from the first side of the lens.

Although this is quite close to the waist found from the beams in MODAL (140.725 mm) there is some uncertainty as the horn reception pattern comes into play. To investigate this further the 2D scan was recreated in MODAL (utilising a scanning dataset) using the same detector horn (see Figure 4-20). The idea was that if the beam waist was found to be in the same location as was found using the manual scan, then the first leg of the prototype could be determined to be behaving as modelled.
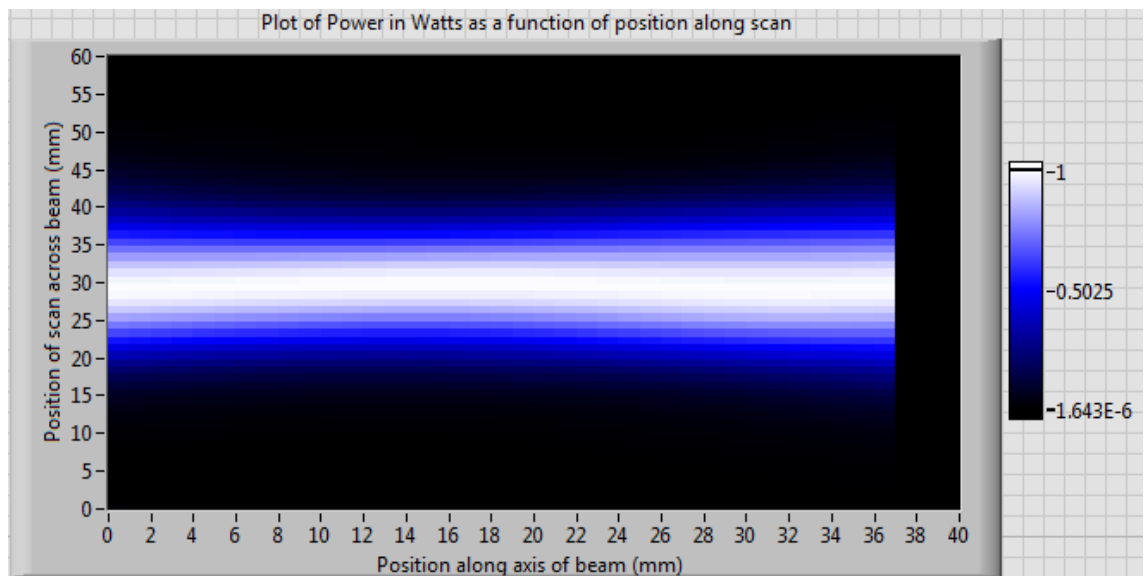

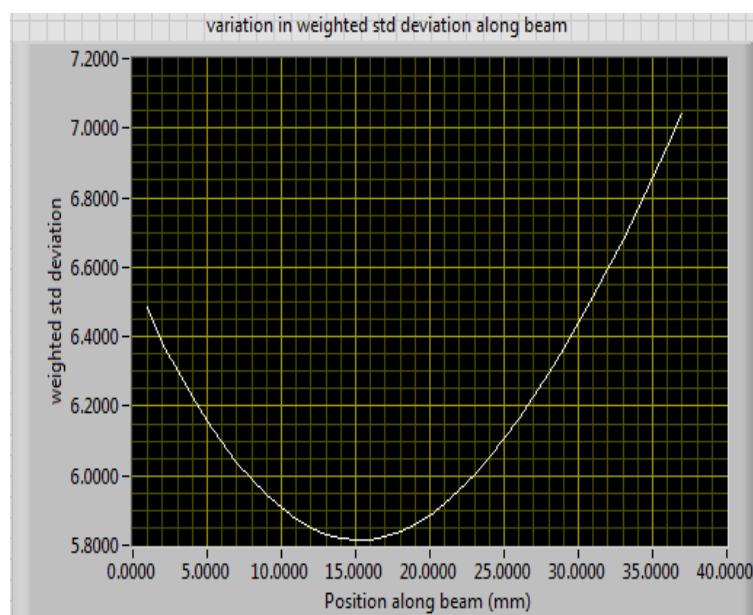*Figure 4-20: Plot of data retrieved from 2D scan in MODAL.*

Figure 4-21: Plot of variation of standard deviation across the scan.

Once again it should be noted that the position on the x-axis in Figure 4-21 corresponds to position along the data set scan with the 20 mm mark corresponding to 140.725 mm from the first side of the lens. This implies that the apparent beam waist is at 135 mm from the first side of the lens. This is in close agreement with the position found using the manual translational stage scan of 138.6 mm. Hence it was determined that the prototype setup was in good agreement with the model in MODAL.

4.6 Development of tilting mirror system

4.6.1 Implementation of mirrors

The next step in the process was to place the tilting mirrors at the beam waist position. The mirrors themselves were squares cut from a rigid sheet of aluminium of thickness $\approx 7\ mm$. The optical surfaces of the mirrors were polished using very fine sandpaper and the mirrors were lubricated with water during polishing to reduce friction. The dimensions of the mirrors were designed so that the mirrors were as large as possible without hitting each other while rotating (if rotating through a full 360°).

As the tilting motion of the mirrors was to be controlled using two stepper motors it was necessary to make extension shafts that clip on to the stepper motor axes. This was so that the mirrors could be mounted a satisfactory distance from the housing of the motion control system to minimise any spurious reflections. These extensions were machined using a lathe. The milling machine was then used to cut a groove into the rods onto which the mirrors could be glued as illustrated in Figure 4-22.
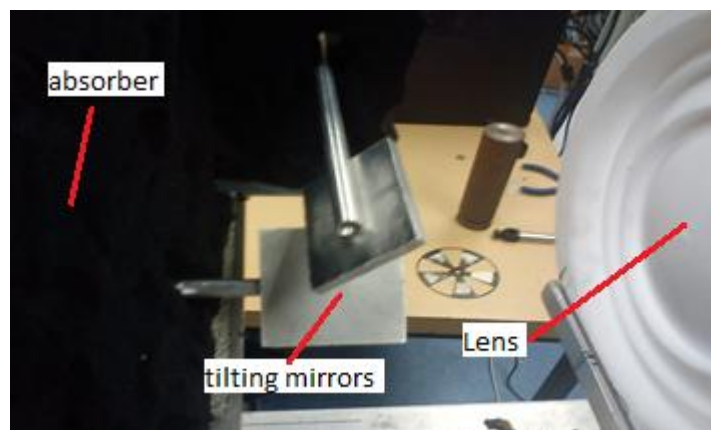

Figure 4-22: Picture of tilting mirrors mounted on extension poles.

Each of the two stepper motors was then mounted on separate vertical plates which in turn were fixed to a large square aluminium plate. This plate was then mounted at the correct height using a cylindrical pole. A hole was drilled in the vertical plates to allow the rods to pass through as illustrated in Figure 4-23.
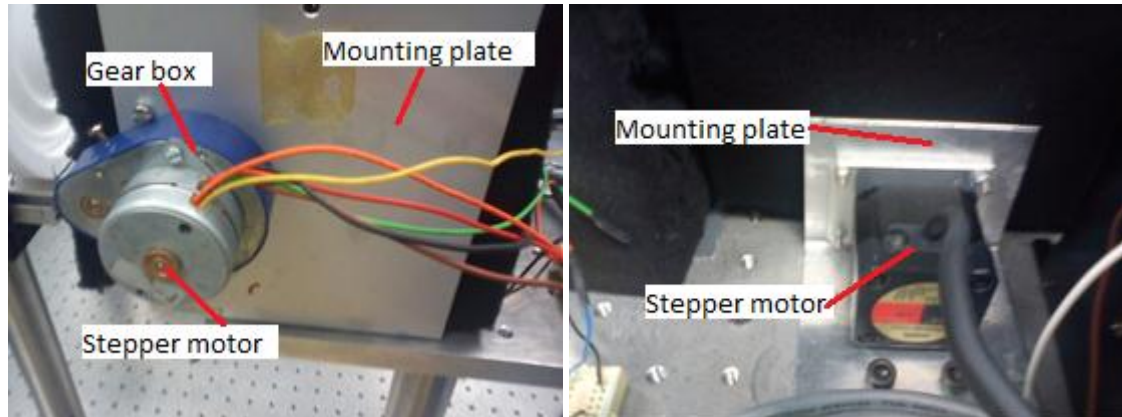

Figure 4-23: Stepper motors mounted on vertical plates. X-axis motor (left) and Y-axis (right) Vertical plates are fixed to large aluminium plate raised to correct height.

When mounting the mirrors and platform mount in the system, care was taken to ensure that the beam waist was located half way between the two mirrors. Since the distance between the two mirrors was 23 mm, the mirrors were placed 11.5 mm closer to the lens to account for this. It was also ensured that the beam was incident on the centre of each mirror when they were placed at an angle of $45°$ with respect to a straight vertical position.

The module was aligned with respect to the optical bench. The edges of the square mounting plate were positioned to be parallel with the mounting holes on the bench. The mirrors were then positioned by having the edge of the plate at a correct distance from the lens mount to have the mirrors in the correct position. Care was also taken to ensure that the vertical mounts for the stepper motors were parallel with the edges of the mounting plate in such a way that the extension rods were perpendicular to the edges. To minimise reflections, absorber material was also placed between the reflective surfaces of the mount and the tilting mirrors. Circular apertures cut form thin pieces of absorber were also placed in front of the tilting mirrors. These were placed between the mirrors and both lenses. The reason for this was to minimise stray reflections on to the mirrors.

4.6.2 Motion control drivers and software

The two stepper motors used were chosen because of their small step size (high resolution). The first motor was produced by McLennan, it is a bi-polar motor and utilises a gear box to increase resolution (s/n 415-8519) see Figure 4-22. The gear box used in this setup has a ratio of 25:1 corresponding in 1200 steps per revolution in full step mode but is also capable of half stepping effectively doubling the resolution. This motor controls the *x*-axis motion across the target screen (left-right scanning motion). The second motor is a 5-phase motor which was produced by Super Vextra (model number PK545-NAC) and has an angular resolution of $.72°$ in full step mode, corresponding to 500 steps per revolution (1000 in half step mode). It controls the *y*-axis scanning motion across the screen (up-down scanning motion).

The driver used for the *x*-axis motor was the Allegro (model no: A4987) DMOS Dual Full-Bridge Motor Driver, it was implemented on a PCB with all necessary components in the electronics workshop in the department. It requires an external power supply of up to 35 V (13 V was determined to be adequate for this motor) and an external logic voltage of 5 V. The driver also has an over current protector whose trip current is determined by a reference voltage and resistor value. In the setup used in this project, the voltage has to be set to .64 V to provide a suitable trip current of .89 A. Motion control software was written by the author in LabVIEW for controlling the motor. The motion was controlled by passing a sequence of pulses to each of the motors connections switching the motors electromagnets on and off in such a way that the shaft rotated as desired.

The driver used for the *y*-axis scanning motor was the Super Vextra 5-Phase motor driver (model no: UDK5128N) and was designed to operate this model of motor. As the driver was designed for the American market, a transformer was needed to convert the mains supply to the desired voltage. A second supply of 5 V was required to operate the logic controls. The code written to control this motor was somewhat less complex as instead of sending a sequence of pulses to each terminal there was only a direction bit and pulse bit required as the actual controlling of the motor was achieved internally by the driver. The motor was then connected directly to the driver via connector terminals.

The interfacing of the motors to the software was carried out using a National Instruments Data Acquisition Card (DAC). The analogue outputs of the DAC were used to provide the 5 V logic Voltage to both drivers and the reference voltage required for setting the trip current for the current protection on the Allegro driver, see Figure 4-24. The digital outputs of the DAC were used to provide the pulses as required to the driver terminals. For initial testing a program was developed that allowed position of the motors to be set and changed as desired.
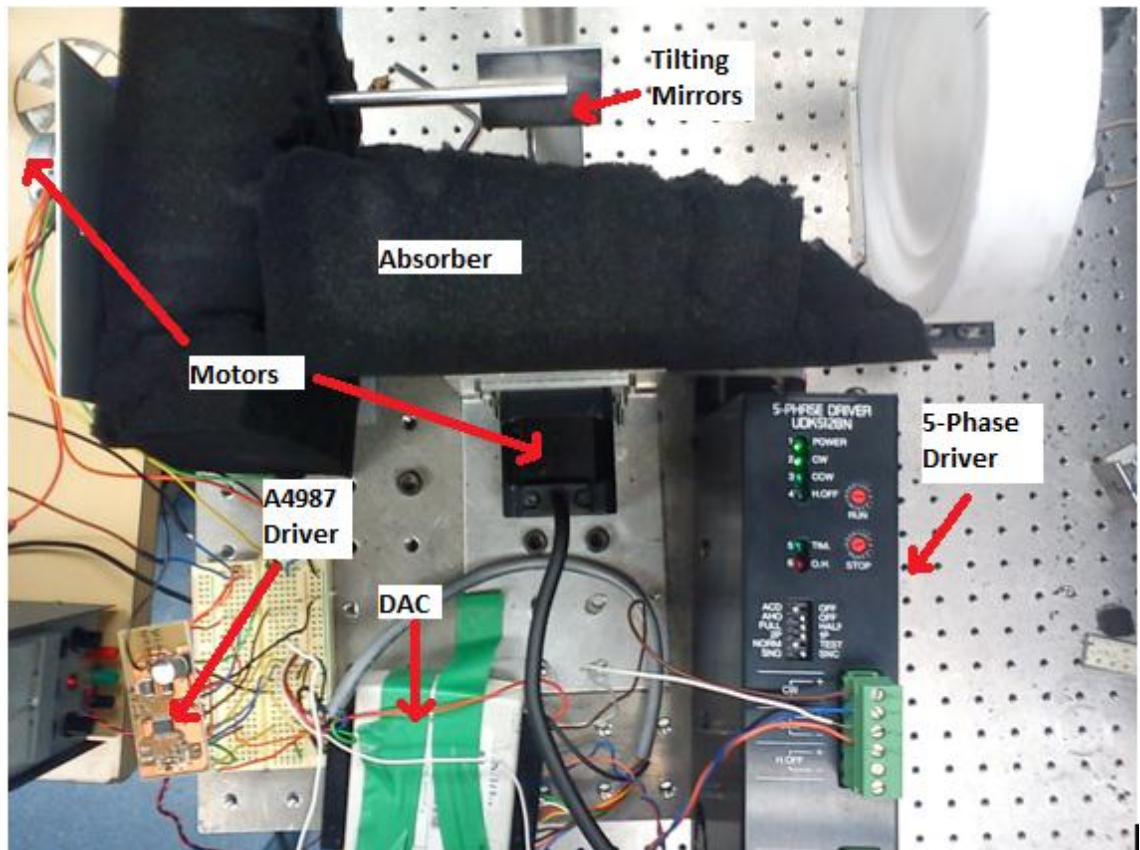

Figure 4-24: Picture of assembled scanning module with driver x-axis motor mounted on breadboard (left) and y-axis driver (right). The DAC is the white box between the two objects. The motor mounts and mirrors can also be seen with absorber placed between the two.

4.7   Implementation of beam focusing stage of the system

Now that the prototype and scanning module were successfully implemented the next step was to implement the beam focusing section of the system. The first step in this involved placing the first side of the lens (side with one step) at a distance of 140 mm (see section 3.5.4) from the tilting mirrors position. The same mount setup that was used for mounting the lens in the transmitting receiving section was used in the beam

focusing section. The alignment of the mount was carried out in a similar fashion to that which was described in section 4.5.1. The edge of the mounting shelf was aligned parallel to the holes in the optical table and hence "square" with any radiation incident on the lens from the tilting mirrors. The radiation incident on the lens was propagating from the lower tilting mirror. It was therefore necessary to ensure that the centre of the lens was at the same height as the centre of the mirror i.e. lower than the centre of the other optical components in the system (23 mm lower). The height of the mount was adjusted to correct for this. The positioning of the lens on the shelf was achieved by marking the centre of the lens and aligning it with the centre of the tilting mirror and hence the centre of the axis of the beam of radiation.

The final component to be put in place was the target plane. This was to be placed at a distance of 355 mm from the second side of the lens. The 3D mount used for scanning around the beam waist of the transmitting receiving section was utilised. This was placed at the target plane location, however the movable nature of the mount allowed for some flexibility in the placement of the object as illustrated in Figure 4-25. Care was taken to ensure that the *y*-axis of the mount was placed parallel to the holes in the table ensuring that any object would be perpendicular to the direction of propagation of any radiation when the mirrors are set to the straight through position (0° tilt).
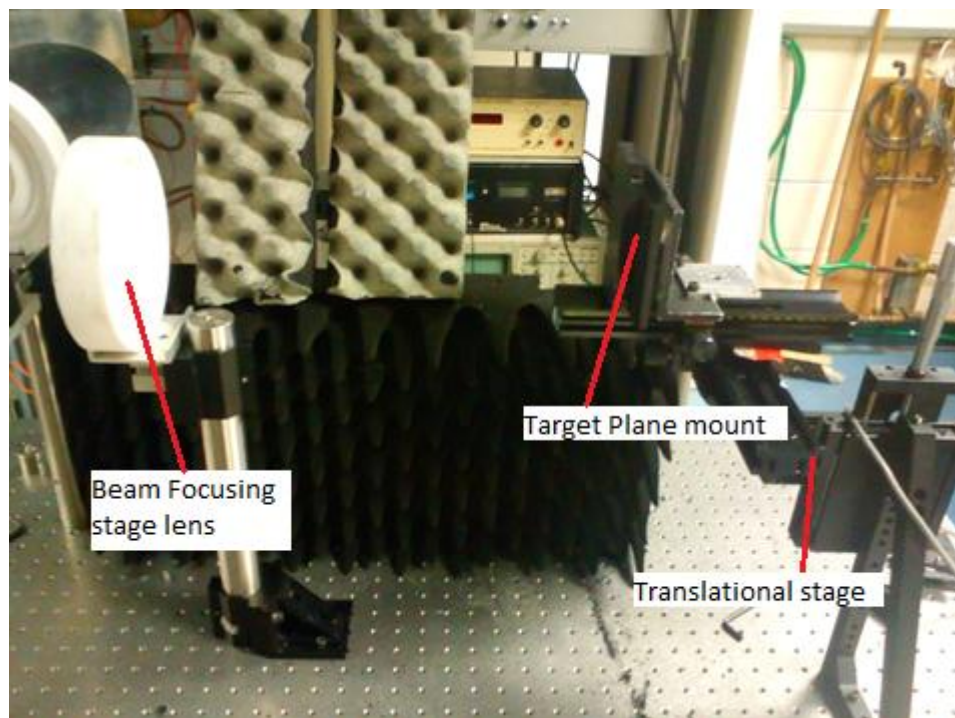

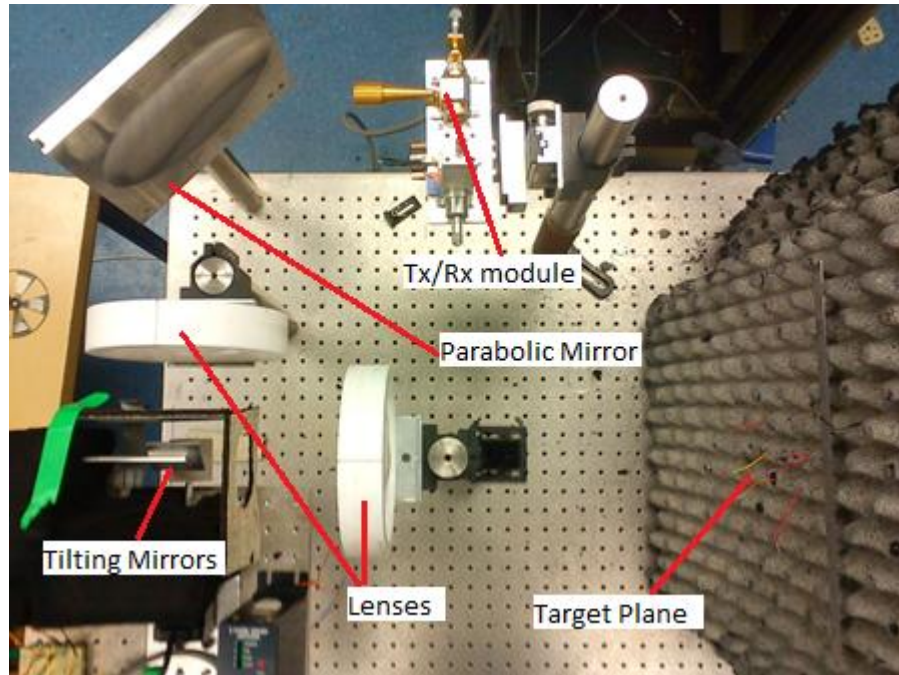*Figure 4-25: Image of setup of final leg of system*

Figure 4-26: Picture of completed system.

4.8 Development of integrated Motion Control and Measurement software

Now that the prototype setup was in place the next step was to develop the software to integrate the motion control of the two individual stepper motors and to recover signals measured from the lock in amplifier. LabVIEW was used for developing this software as it allows easy interfacing with external devices. It was desired that the beam scan the target in a raster pattern as illustrated in section 1.3.2. As discussed in section 4.6.2 the 5-phase motor was used for controlling the up-down motion of the beam (*y*-axis) and the bi-polar motor used for the left-right motion (*x*-axis). When the program was run the user set the home position for each of the mirrors. The user was allowed to define the scanning range of both axes (with respect to the home position) and the number of points to be used.

The mirrors are initially set to the extreme of the scanning range, a cut across the target is then scanned with one mirror while the other is in a fixed position. At the end of the scanning range the stationary mirror is incremented and a scan back across the object is done using the second mirror. In this way the object is being scanned in a raster fashion. This process is repeated until the entire object is scanned.

The signal received by the lock in amplifier was read by the program using a General Purpose Interface Bus (GPIB). Communication was opened with the lock in amplifier using LabVIEW's VISA open VI. The appropriate read and write commands were then used as specified in the user manual to obtain the scaled *x* and *y* components of the signal.

The last component of the program involves plotting the array of values measured for each point on the scan on an Intensity Graph. Some post processing of the data was necessary to plot the measurements as required. For instance every second row of the scan had to be reversed as the mirror was scanning in the opposite direction for these measurements. Also the array had to be transposed so the plot was representative of the target under investigation. See Figure 4-27 for a graphical representation of the program.
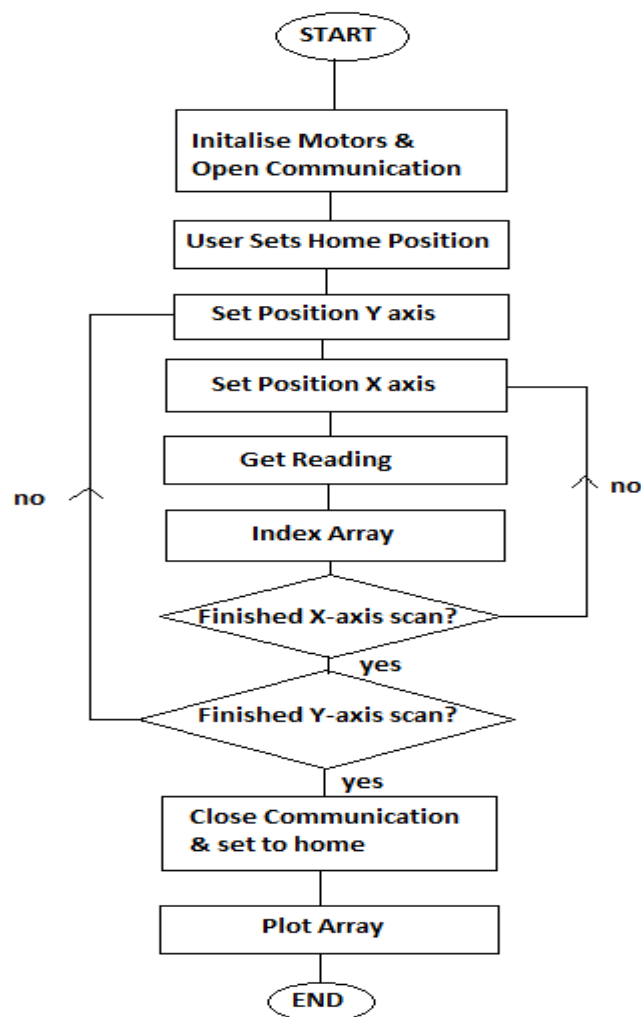

Figure 4-27: Flow chart illustrating operation of software implemented.

4.9 Initial Measurements and problems with streaking

Now that the construction of the prototype was completed the next step was to start imaging objects and try to evaluate the performance of the scanner. Initially it was decided to try and image a rectangular metal plate to investigate what reflections could be detected back from the scanner. As the metal plate was to be placed in front of a sheet of absorbing material a scan with only the absorbing material present was run initially for comparison purposes. As expected there was minimal detail in the image as illustrated in Figure 4-28. Any signal measured was largely due to the leakage from port 1 to port 3 of the circulator i.e. from the source straight through to the detector. This leakage was measured to be .249 mV before the scan was run.
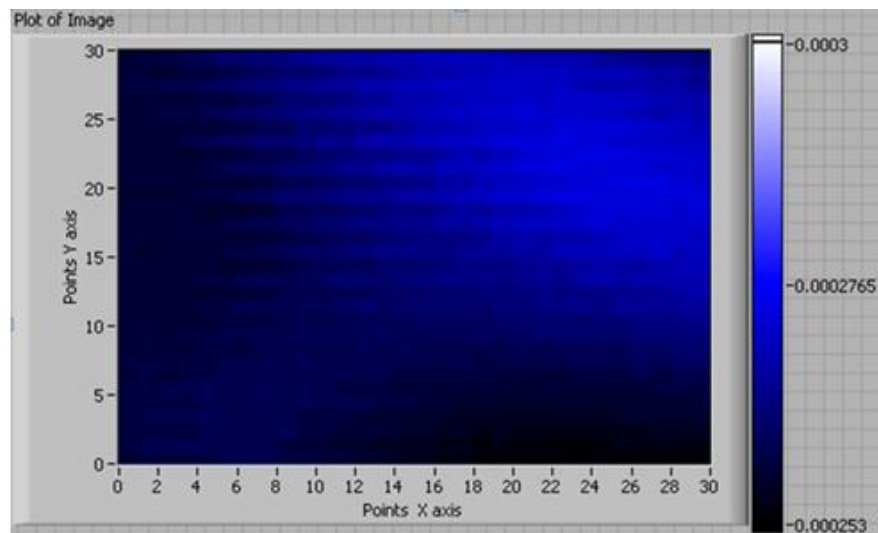

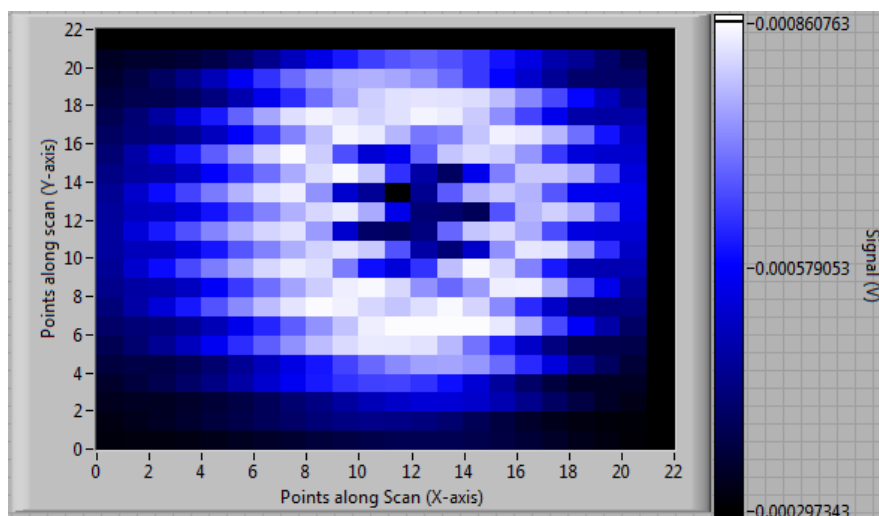*Figure 4-28: Scan with absorber in place, signal is plotted in Volts.*

Figure 4-29: Scan of flat rectangular metal plate.

It is clear from Figure 4-29 that there was quite a large amount of streaking in the image. As the source was unknown it was necessary to investigate and eliminate this effect. At first it was though that the problem lay with either the time constant setting on the lock in amplifier, the frequency of modulation of the signal or the execution timing built into the motion control software. These were suspected as it was thought that either the program was not providing enough time to measure a signal from the lock in amplifier or that the time over which the lock in amplifier integrates a signal was either too short or too long. This is also affected by the modulation frequency.

The measurement scans were then repeated while systematically changing the three parameters. It was found that increasing the modulation frequency increased the quality of the image but only very slightly. Above 3870 Hz the quality did not change so this was deemed the optimum frequency. It was found that increasing the time constant on the lock in amplifier user interface improved quality with a peak in quality at 640 µs any higher than this and the quality stayed the same but the measurement took longer. When investigating the execution timing it was found that the streaking was reduced at 0.7 seconds with longer periods being unnecessary, however any shorter and the streaking increased again. Although optimising these parameters reduced the streaking as illustrated in Figure 4-30 it was still present and this needed to be addressed.
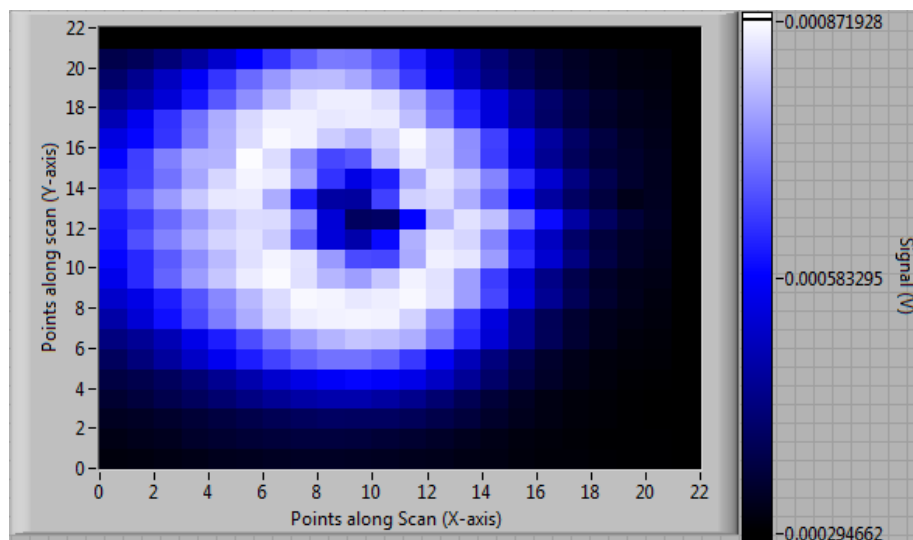

Figure 4-30: Reduced streaking with optimal parameters.

When considering the matter further it was noticed that the rod that the mirror was mounted on had a degree of movement around the motor shaft (backlash). This was the case for the *x*-axis motor rod but not the *y*-axis motor. This was the motor that was moving a lot more frequently throughout the scan due to the scanning pattern being used. It was thought that there could be a backlash error associated with this setup and could perhaps be causing the streaking effect. It was decided to rewrite the code for the scanner so that the scan was still done in a raster pattern but the *y*-axis motor was moving more often i.e. in such a way that the target was scanned up and down in a raster pattern as opposed to left and right. It was thought that the decreased movement of the *x*-axis motor coupled with it not having to change direction throughout the scan would eliminate the backlash error and hence reduce streaking.
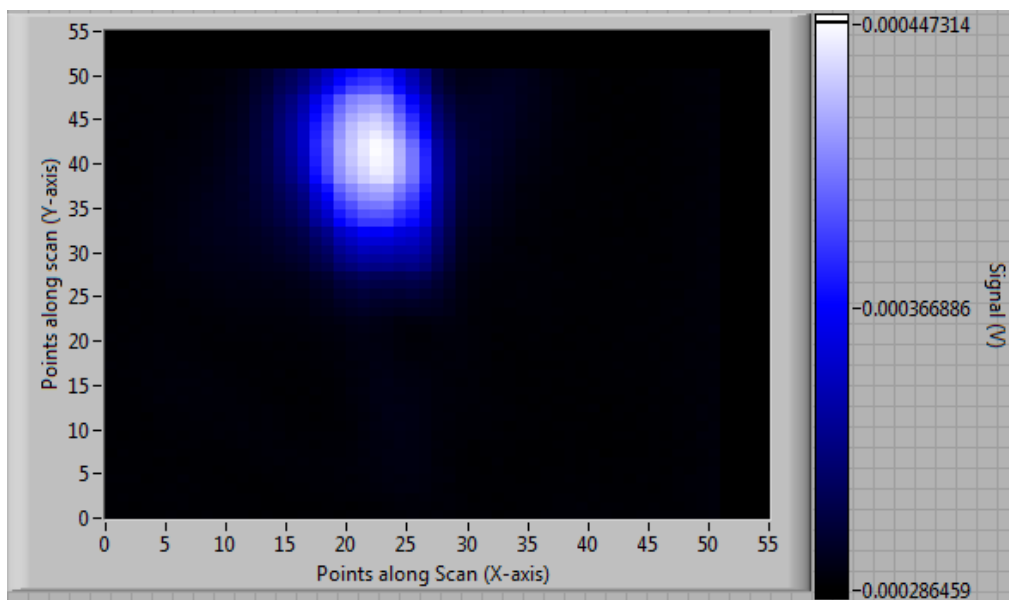

Figure 4-31: Image of reflective plate with streaking eliminated.

Once the code was re-written a scan of a reflective plate was done and plotted as can be seen in Figure 4-31 above. It is clear that the streaking effect has been eliminated as a result of changing the scan pattern. To ensure that the problem did not resurface the movement of the rod around the motor axis was eliminated by filling a small gap between the motor axis and the inside of the extension rod. With this setup time taken to scan an object was quite short with an 80x80 point scan taking just under ten minutes.

4.10 Determination of scanning range and investigation of sensitivity

Now that the problem with streaking in the images had been resolved the next thing that needed to be investigated was the effective scanning range of the prototype. It was decided to investigate this by placing a metallic strip at different locations and in different orientations at the target plane (see Figure 4-32). For example when investigating the range along the *y*-axis (up – down) the strip was place horizontal along the *x*-axis. For each scan the strip was moved up and down gradually to find where the limits of the range were. The strip was placed against an absorber background. When starting the measurements a scan was done with just absorber in place initially to use as a reference. The leakage (base signal) was measured to be .241 mV.
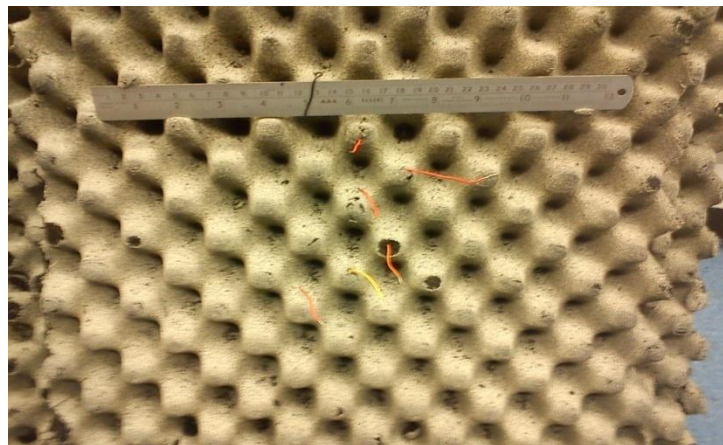

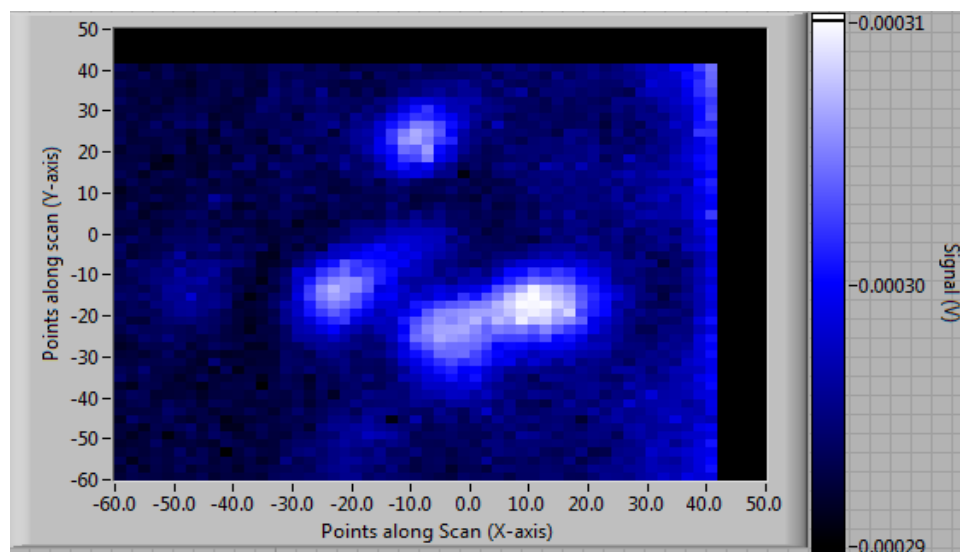*Figure 4-32: Picture of metal strip against absorber with honeycomb structure.*

Figure 4-33: Image with absorber only in place.

The absorbing material used here is different from the absorber used for the measurements in section 4.9. From the plot of the scan with only absorber present in Figure *4-33* it is clear that there is some structure in the image. It was thought this was as a result of reflections from the material itself. To independently verify this, the scan was repeated with another piece of material that was known to be a good absorber.
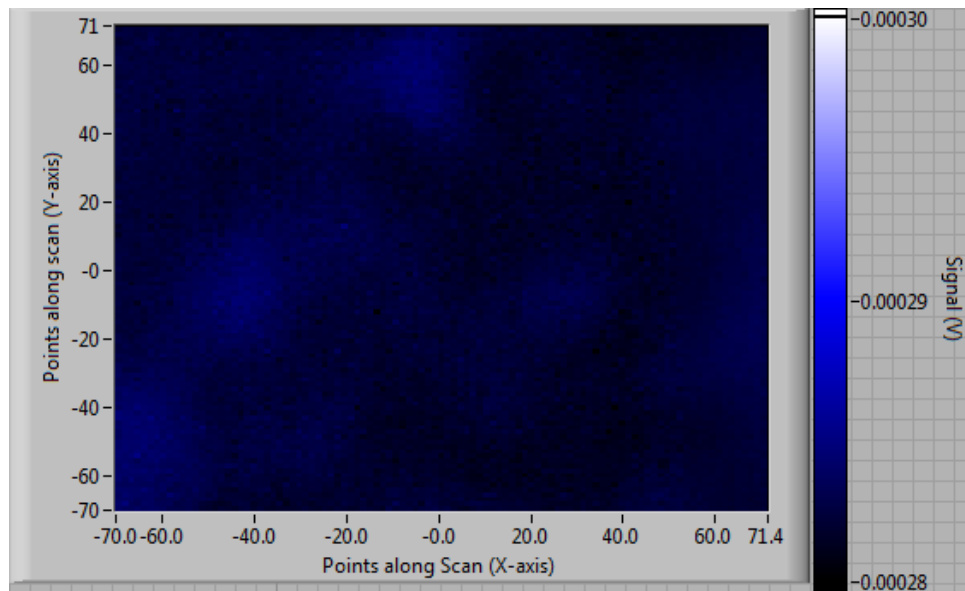

Figure 4-34: Scan of third absorber material.

As the structure is removed with the new absorber in place it has been proved that the detail in figure 4-33 is as expected from the structure of the absorber. It was later discovered that the absorber was bought quite a few years ago and was the least effective out of the absorbers available in the department. Furthermore analysis using the VNA shows that the absorber is not very effective at the wavelength under investigation in this situation (100 GHz). The fact that the absorber structure can be imaged does however indicate that the sensitivity of the prototype is quite good.

It should be noted that the absorber issue was only investigated after the scans contained in the rest of this section were completed and hence the structure of the absorber was still present, however this did not affect the investigation of the scanning range. As discussed earlier that metal strip was placed at different positions along the absorber and the scans repeated. The results of some of these can be seen in Figure 4-35 andFigure 4-36.
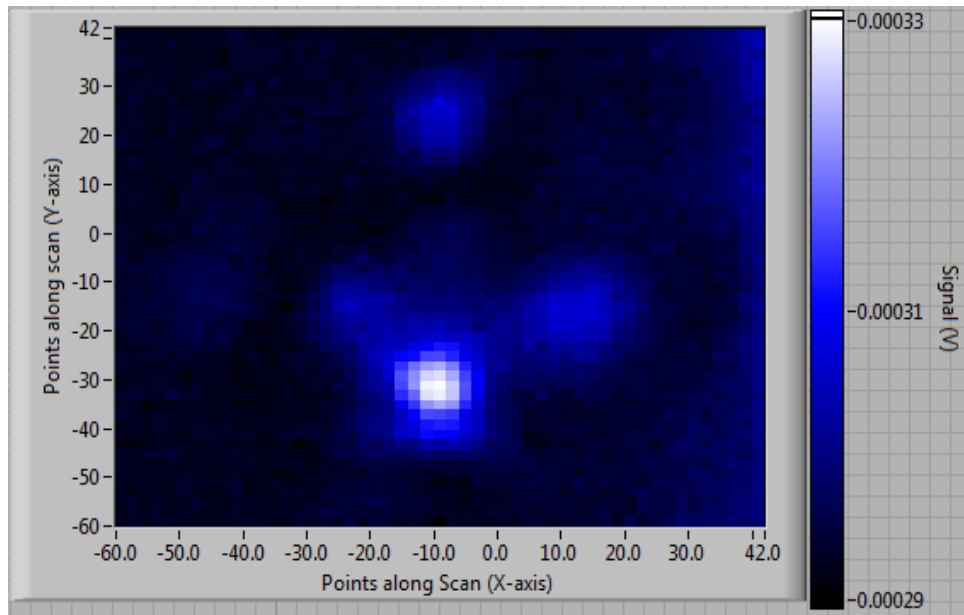
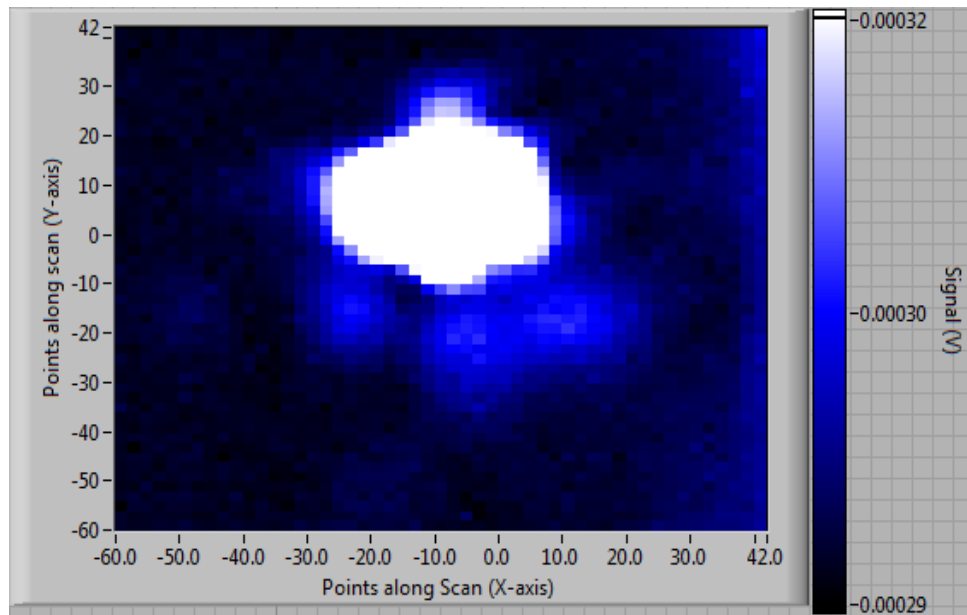*Figure 4-35: First scan where metal strip was detectable.*

Figure 4-36: Metal strip at top of range.

As the units along the axes correspond to stepper motor positions it was required to establish what this corresponded to in terms of position along the object plane. It can be seen form Figure 4-35Figure 4-36 above that the strip was detectable from -40 up to 27 or 67 positions along the scan. It is also known from the placement of the strip at different positions that this corresponds to 8.75 cm along the target plane. This corresponds 0.13 cm per step for the *y*-axis.

When doing a similar analysis on the *x*-axis it was found that a signal was detected over 95 positions along a scan of 11.25 mm corresponding .118 cm per step for the *x*-axis. The calculations for this axis were carried out with the stepper motor set to full step mode (1200 steps per revolution) hence in half step mode the .059 cm on the object plane is covered for each step of the motor. This is consistent as the resolution is higher for this motor a smaller step size is expected

4.11 Scanning of Various Objects

4.11.1 Image of Reflective M shaped reflector and absorber

The next step in the process was to try and image various objects using the prototype. The first object that was attempted was the letter "M" cut from a sheet of absorber (see Figure 4-37). This was placed against a highly reflective background. It was hoped that despite the deliberately blurred beam it might be possible to directly image the reflective M shape.
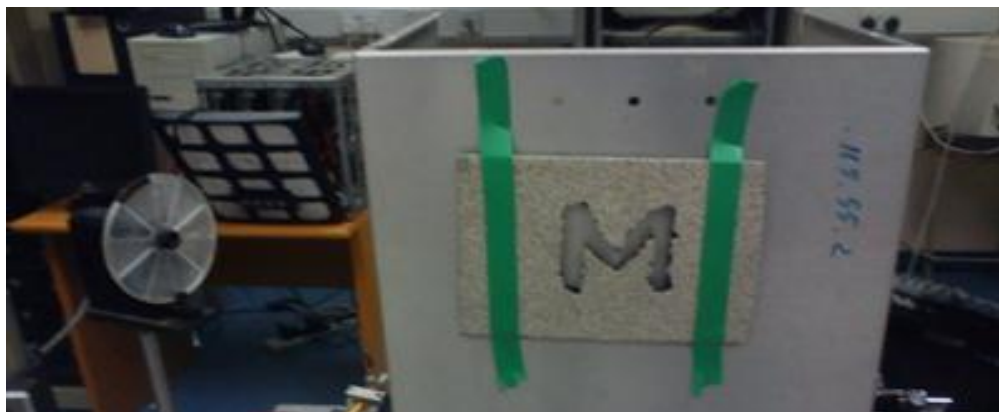

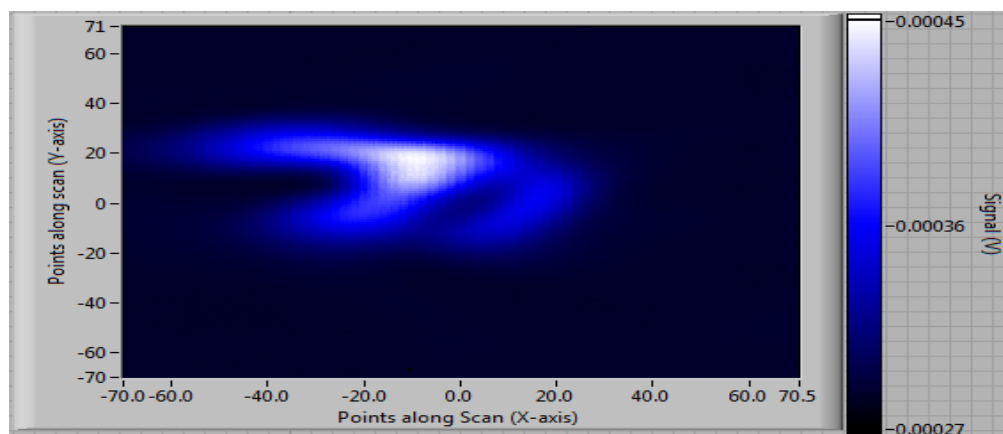*Figure 4-37: M shaped target under investigation.*

Figure 4-38: Resulting image of reflective M.

Form Figure 4-38 it is clear that the M shape is not imaged well, however it is clear that the scanner is picking up some sort of structure from the M. The scanner was deliberately designed to essentially blur images for the purposes of post processing (as discussed in section 1.4.2 above) and for this reason the beam width at the target is wide. This may account for any loss of acuity.

To investigate the situation further it was then attempted to scan an absorber shaped M surrounded by a metallic surface (essentially the inverse of the situation above) as illustrated in Figure 4-39.
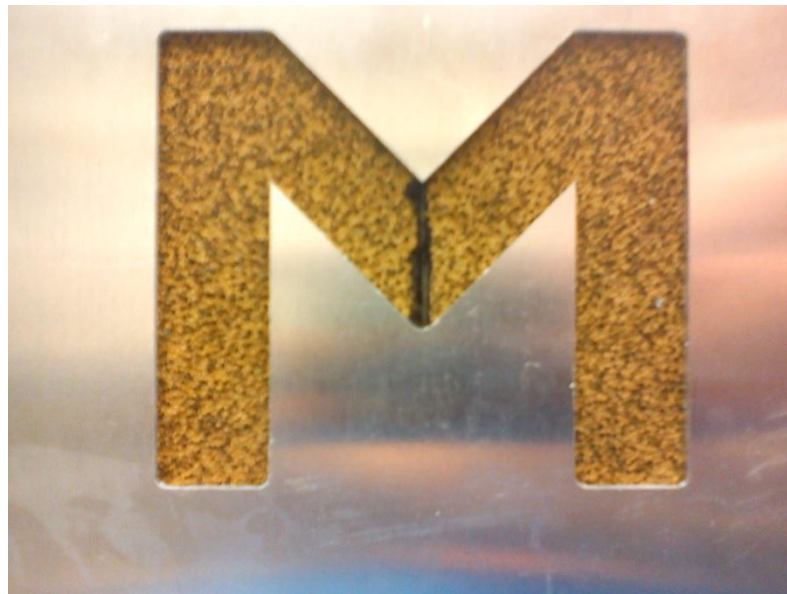

Figure 4-39: Absorber shaped "M" with surrounded by reflective surface.
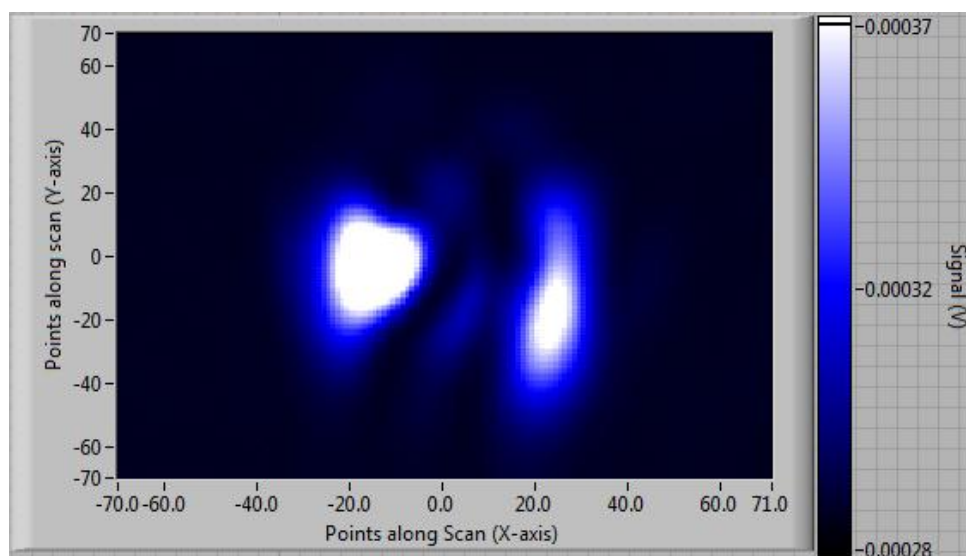
Figure 4-40: Imaged "M" shaped absorber.

From the obtained image illustrated in Figure 4-40 it is clear that there is detail being picked up by the scanner however, once again a clear M shaped image is not obtained.

4.11.2 Imaging of cup with varying amounts of water

The next thing that was attempted was to image a plastic cup containing various amounts of water. The cup was placed against a reflective background. As water is a strong absorber it was expected that the reflections detected would dramatically diminish.

Figure 4-41: Images of plastic cup of water taken in visible wavelengths with camera (left) and at 100 GHz using prototype (right) containing different volumes of water. With cup 1/4 full (top), 2/3 full (middle) and almost completely full (bottom).

It can be clearly seen from Figure 4-41 that as the water level in the cup rises the reflections from the metal plate reduce as expected.
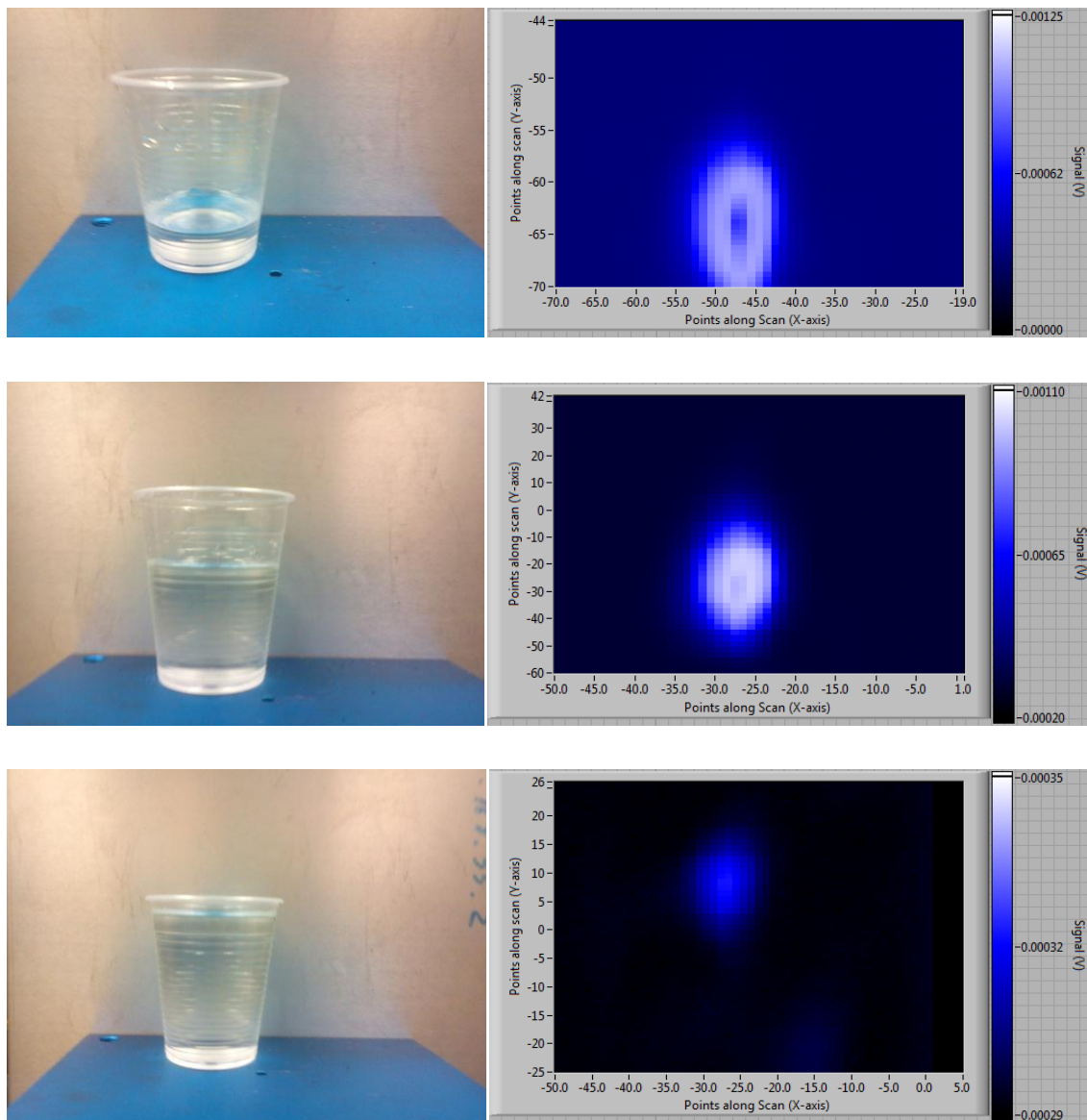
To investigate the situation further the cup was then moved left and right and the scan repeated.
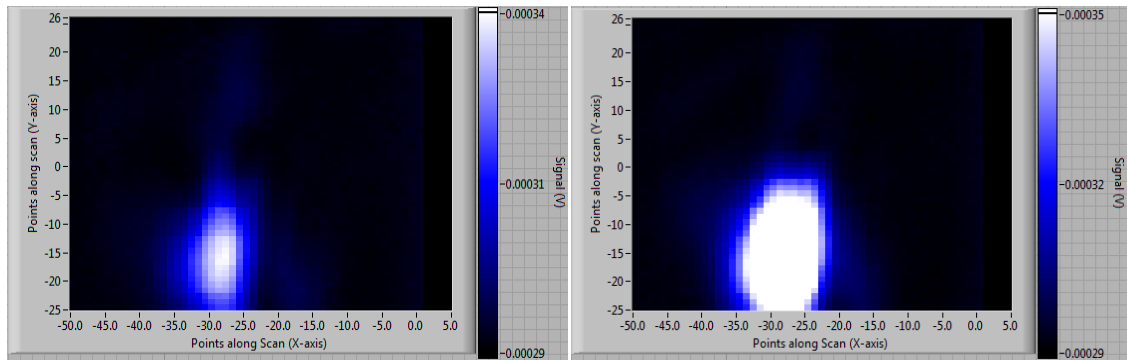
Figure 4-42: Full cup of water shifted 1 cm to right (left) and 2 cm to right (right).

From Figure 4-42 it is clear that as the cup is moved off centre the reflections increase. This is expected as the absorbing water is no longer placed at the centre where the reflections are highest due to the tilting mirrors being at the straight through position (0° tilt).

4.11.3 Imaging of CD case

It was then attempted to image a dielectric CD case (pictured in Figure 4-43) with and without CD's inside. In this case absorber was placed behind the CD holder.

Figure 4-43: CD holder imaged with absorber behind. Case is mounted on an adjustable stand to reach the desired height.
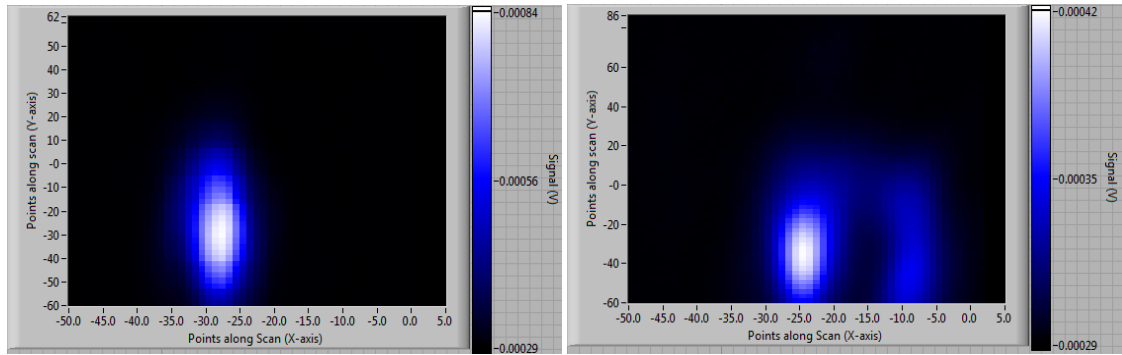
Figure 4-44: Image of empty CD case (left) and case containing CD (right).

From Figure 4-44 it is clear that when the CD is placed in the case a structure can be detected however it is not apparent that it is a CD that is in place. The CD case was then moved left and right and the scans repeated to investigate if there was any response.
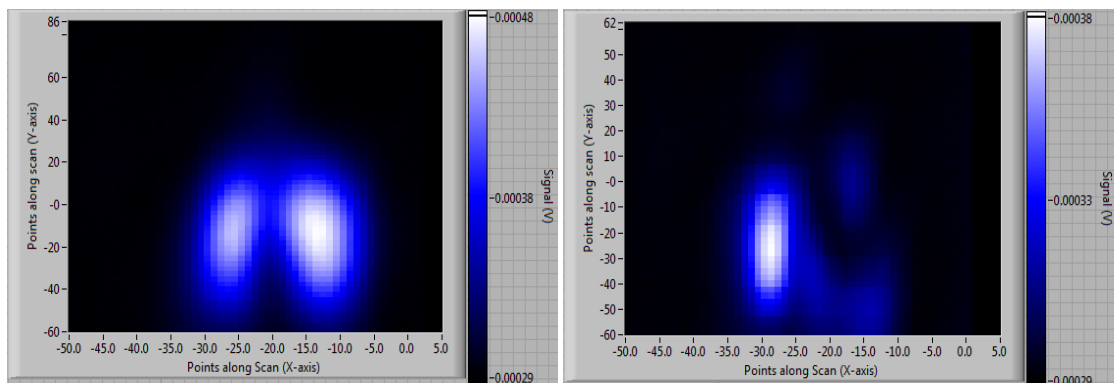
Figure 4-45: Images obtained when case moved 1cm to left (left) and 3cm to left (right).

From Figure 4-44 and Figure 4-45 it is clear that there is a variation of structure inside the case that is being detected. If the CD is removed and scans repeated the profile of the empty case in Figure 4-44 above is obtained once again as would be expected.

4.11.4 Imaging of CD player

The final target that was imaged was a CD player (see Figure 4-46). This was scanned as it was comprised of a varied structure consisting of various plastic and metal parts. It was envisaged that the radiation would pass through the plastic parts and be reflected by the metal parts. Batteries were also placed in the player to increase reflectivity.

Figure 4-46: Picture of CD player under investigation consisting of various plastic and metal components.
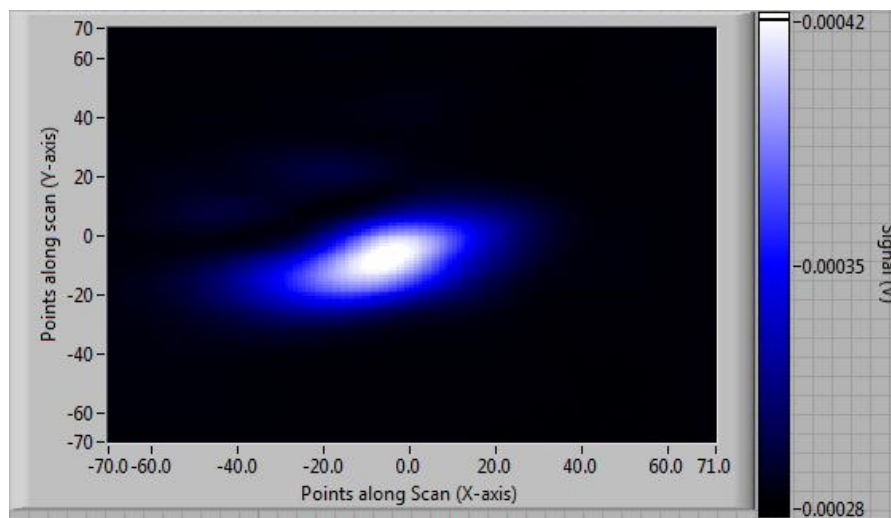
Figure 4-47: Resulting image of CD player.

From the image of the CD player in Figure 4-47 it is clear that there is structure in the reflected radiation that is being detected. Although the elements in the player can't be identified the scan shows the potential for imaging such objects more accurately if a post processing routine was applied to the data.

4.11.5 Imaging using Phase modulation technique

The above images were obtained using the function generator for pulsing the source as the method of modulation. It was then decided to implement the dielectric chopper in the system to see if the sensitivity of the prototype could be increased. As seen in

Figure 4-32 an image of absorbing material was obtained due to the scanner being sensitive enough to image reflections from the absorber. It was decided to image the absorber again to draw comparisons on the two techniques and hence investigate the change in sensitivity.
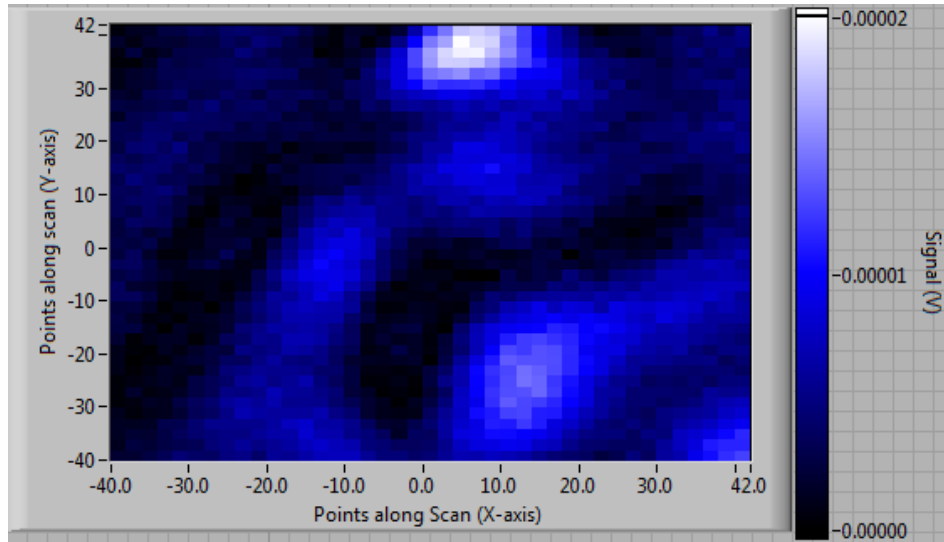
Figure 4-48: Absorber scanned showing structure in absorber.

It is clear from Figure 4-48 that the sensitivity of the system is increased as the base signal is reduced considerably (measured to be .001 mV) allowing the detection of lower level signals. As a result it was possible to image the structure of the absorber in more detail than obtained in Figure 4-32. It was then decided to re-image some of the objects imaged before.
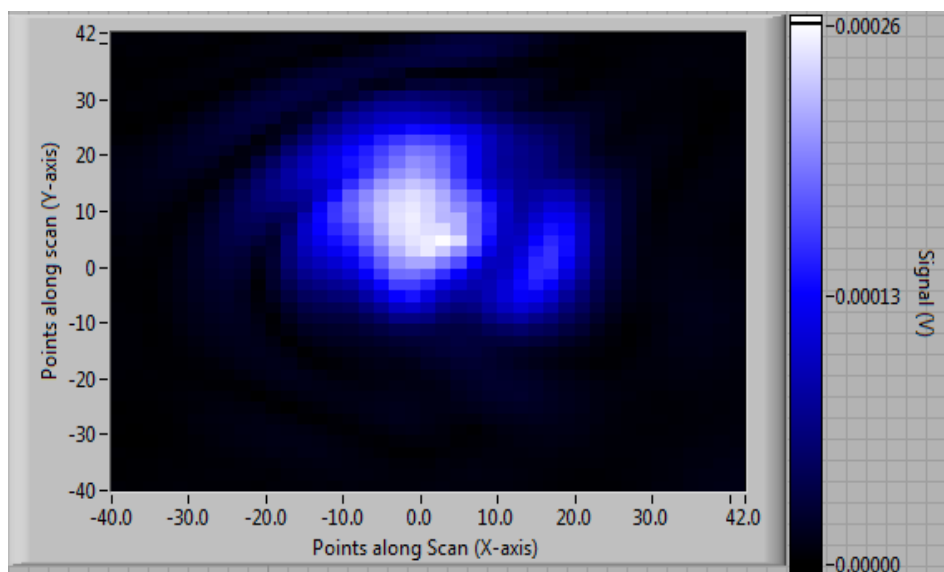
Figure 4-49: Scan of M shaped absorber.

103

Figure 4-49 is an image of the M-shaped absorber pictured in Figure 4-39. It is clear that there is structure pertaining to the structure of the object in the data however the M-shape is not clearly visible. Again this is a result of the blurring effect of the deliberately wide beam at the object plane. The reason the image looks different to the image of the same object in Figure 4-40 is because the modulation technique used is more sensitive to phase variations throughout the image.

5 Chapter 5

Conclusions / Future Work

5.1 Outline of work completed

The purpose of this project was to develop a scanning system for operation in the Terahertz region of the electromagnetic spectrum. The prototype developed was essentially a proof of concept for the scanner design used. The scanner uses a unique approach for imaging in that it uses a pair of computer controlled tilting mirrors to point an incident beam of radiation to a point of interest on the target. The scanner utilises a transmitter receiver module for the purposes of illuminating the target under investigation and detecting reflected radiation. The same optical path through the system is used for both transmission and receiving of radiation. The measurement system of the receiver utilises a lock in amplifier in a phase locked loop for detection of small reflected signals. As the tilting mirrors point the radiation from point to point on the screen an image of the object is then formed on a point by point basis.

The optical design has been outlined for both the transmitting receiving section and beam focusing section of the prototype and the results of the modelling process presented. It was shown that power losses throughout the system are at an acceptable level and it is capable of propagating radiation to illuminate a target and detecting any reflected radiation effectively. Although concessions had to be made on the scanning distance and range the design is more than adequate for the purpose of proof of concept of the scanner.

A motion control system has been developed for the tilting mirrors to be computer controlled. Each mirror is mounted to the axis of a stepper motor. The motion control software for scanning an object in a raster pattern was successfully implemented and a General Purpose Interface Bus used for reading the measurement at a point on the scan from the lock in amplifier. The scanner is capable of scanning an 80x80 point scan taking just under ten minutes.

Several techniques for modulating the signal as required for the phase locked loop were discussed. The pros and cons of mechanical modulation and source modulation

were considered and tested. This led to the development of a dielectric phase modulator to eliminate the problems of leakage from the source to the detector across two decoupled ports in the circulator, and reflections from the mechanical chopper blades. The dielectric modulator was initially tested using a situation with a strong reflected signal. Although the base signal was reduced in comparison with the other methods the dynamic range of the method was lower than the mechanical chopping method. This is as a result of the chopper not being effective in certain situations dealing with high strength signals (as discussed in section 4.4.2). It was shown however that the technique is effective when dealing with small signals as is the case with the finished prototype setup.

The work ended with the scanning of various objects and materials. It was hoped that despite the wide scanning beam at the target plane it would be possible to retrieve a somewhat sharp image of the structure of the objects under study in the image obtained. Although this was not possible it is essential to remember however that obtaining sharp images of objects using a tightly focused beam was never the aim of this setup. The aim as discussed in section 1.4.2 above was to use post processing of the data retrieved to increase the resolution of the images. To this end the beam is deliberately blurred (not tightly focused) at the target. It is however apparent in the images obtained that there is information pertaining to the structure of the object in the obtained image. Thus the scanner prototype can be considered a success.

5.2 Future Work

Work done on the project in the immediate future should focus on developing a detailed understanding of the beam pattern and power incident on the target for different angles of tilt. This is because it is necessary to develop a detailed understanding of the beam incident to perform post processing techniques on the obtained data.

It is envisaged that the post processing method used for the enhancement of the images received will mimic the hyper acuity of the human eye. The hyper acuity of the eye is the ability of the human eye to see beyond the understandable acuity defined by the number and size of the photoreceptors of the human eye. Trying to explain the resolution capabilities of the eye, even including diffraction, the minimum angle of

resolution continues being one minute of arc since the Rayleigh criterion establishes a minimum distance to establish two airy discs as $3.6\,\mu m$. Under this assumption it is clear that the image finally sensed must be absolutely blurred since the diffraction pattern, airy disc, resulting from a single incident plane wave at the aperture (pupil) casts a shadow on the detectors located on the retina which would cover a minimum of 7 detectors as illustrated in Figure 5-1.
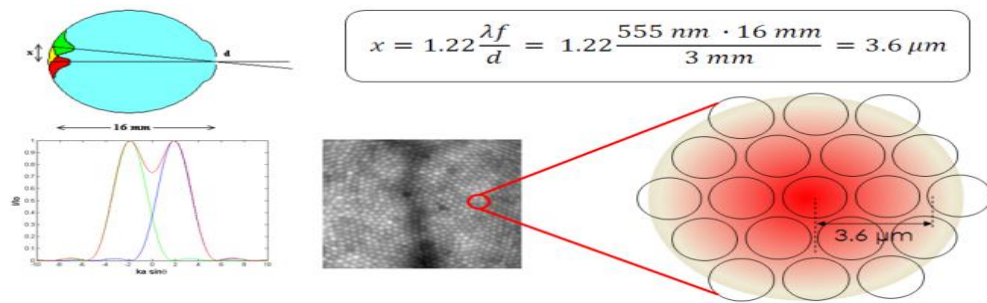

$$x = 1.22\frac{\lambda f}{d} = 1.22\frac{555\,nm\,\cdot16\,mm}{3\,mm} = 3.6\,\mu m$$

Figure 5-1: Explanation of the human eye reception concept (32).

It is understandable that the brain uses some sort of interpolating post processing procedure for resolving points between detectors to obtain a continuity sensation of the images. Consider the situation (see Figure 5-2) below where there is a 5x5 detector array. The detector array is being illuminated by a pinhole aperture and as a result of diffraction the airy disc covers a number of detectors. Using an interpolating process is possible to recreate what would be detected with a 10x10 array. From here it is envisaged that it would be possible to apply a de-convolution technique to the data, restoring the diffraction pattern over the newly created 10x10 image and hence solving the exact impact point of the incident ray to the real 5x5 sensor array i.e. increasing the resolution. (32)

5 x 5 sensor array with an incident ray between 4 sensors...

5 x 5 sensor array illumination created by the same incident ray and diffracted by a circular aperture

Result of the interpolation process, creating a new 10x10 image of the same diffraction pattern

Restoring the diffraction pattern over the new created 10x10 image, solving the exact impact point of the incident ray to the real 5x5 sensor array
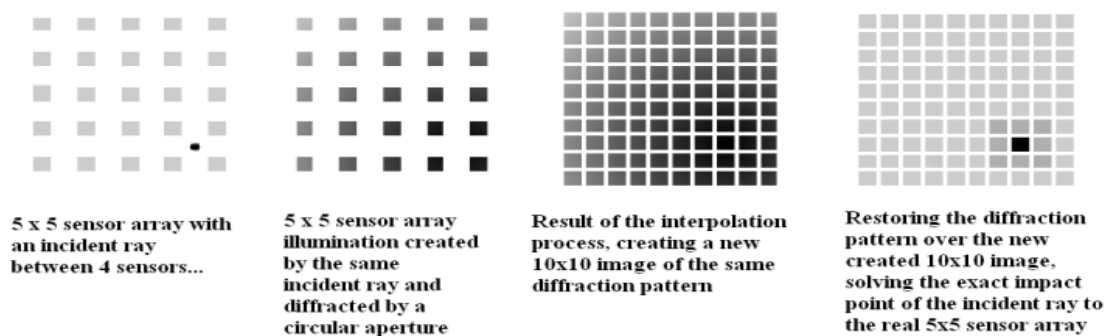
Figure 5-2: Explanation of post processing technique that could be used to increase resolution of images (32).

The scanner system in this project was designed with this post processing technique in mind. The aim was to have a well understood beam throughout the system and also at the target plane. The incident beam also had to be fairly wide ≈ 15 mm at the target for interpolation purposes.

The system could be improved by using custom made components instead of the already existing components used for this prototype. In terms of increasing the scanning distance and range of the prototype the beam focusing stage could be improved by removing the hyperbolic lens and replacing it with a parabolic mirror with a short focal length and large surface area. If the tilting mirrors are placed at the focal point then the resulting collimated beam could be used for scanning. A short focal length is required to not have a collimated beam that is too large in diameter. A large surface area is desired to reduce truncation when the incident beam is tilted through large angles.

6   Appendix A

MODAL description

The Quasi-optical analysis of systems contained in this thesis (including the plots above) was done using a software package called MODAL. MODAL is an acronym for Maynooth Optical Design and Analysis Laboratory. This is an in house software package which has been continually evolving over the last number of years. The package is currently under development by Dr. Marcin Gradziel originally under a Science Foundation Ireland (SFI) grant. A prototype of the software was initially developed by Dr. David White however further development has occurred over a number of years and is currently on version 9.1r27.
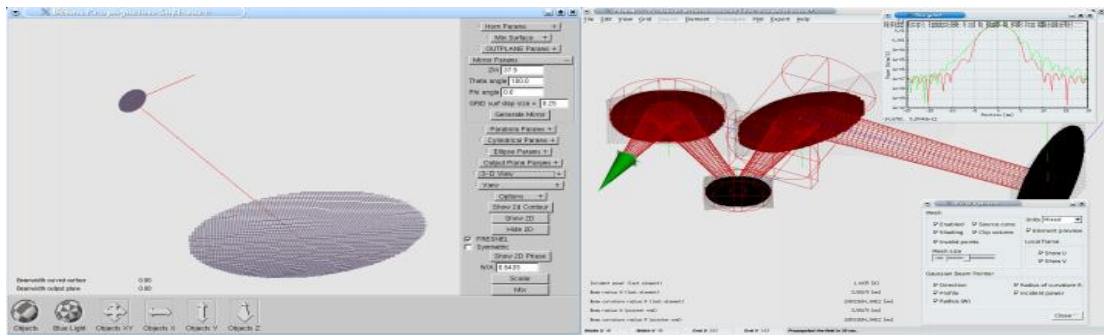
(a)   (b)
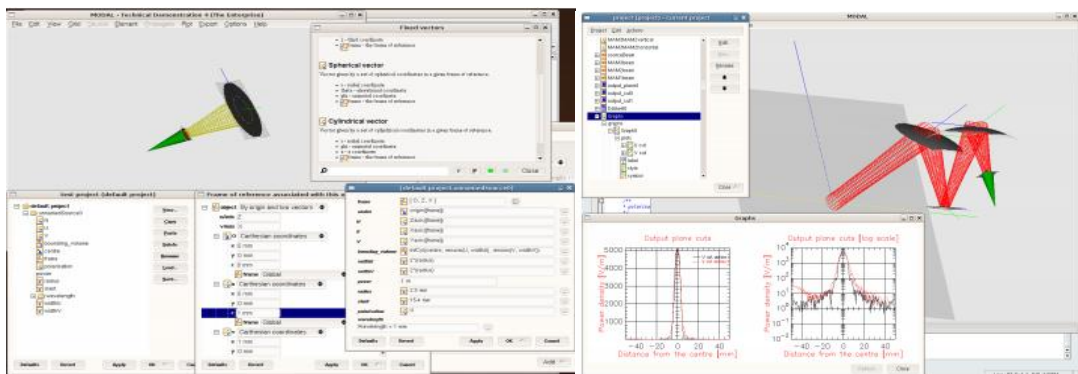
(c)   (d)

Figure 6-1: Screenshots of MODAL at different times throughout its development. (a) shows prototype software in 2003 (5) (b) shows MODAL in 2003/2004 when a linear workflow has been implemented (c) is the state of the software in 2005 with the property editor and physical units implemented (d) shows MODAL in 2006 with project handler and integrated plotting introduced.

The initial idea behind MODAL was to develop a package capable of quick and easy system definition in a 3D environment. This was to be achieved by use of flexible approach to system definition. The user was also to be enabled to view the system/element at different angles in the 3D environment as well as view cuts or contour plots of the field at any point along the system. The software was also specifically designed to target the sub-mm wave/THz region of the electromagnetic spectrum, making MODAL unique among other software packages in that respect. Although other packages are used for modelling sub-mm wave systems they are designed with either RF or infrared purposes in mind. The power of MODAL was to be in its variety of propagation techniques as it incorporates a large number of different methods (GBM, Fresnel Diffraction, Physical Optics etc) combined with its capability for parallel processing (clusters, multiprocessor machines). Another advantage of using in house software is that unlike commercial packages such as GRASP or Microwave Wizard the software can be adapted to the challenge at hand.

MODAL was developed purely with C++ code and is a multiplatform package, currently installable on machines running Linux 32 and 64 bit and Windows 32 bit. The C++ code is composed of roughly 90,000 lines of code however this is heavily templated with the equivalent C code being 3-5 times greater which is completely unmanageable for one developer. Subversion was used to manage source code revisions and Cmake for program building. Libraries such as FLTK/FLU were used for developing the user interface and OpenGL for 3D environment along with PIPlot for plotting of graphs. PVM was also used for managing MODAL's parallel processing responsibilities along with XMLWrapp/libxml2 for managing XML input/output.

In terms of high level design MODAL is equipped with a variety of classes of complex components, some representing physical objects and others representing abstractions or user/storage interface objects. The components currently in existence are discussed below:

➢ **Project** The project contains a user defined set of objects/properties associated with the optical system being defined. It has its own hierarchal editor where components can be added and existing components edited. The program can be saved and an existing program loaded where necessary. The project is viewed

through the project window shown below. The open project can be viewed in real time through a separate window where the angle zoom factor and some other viewing options can be altered.
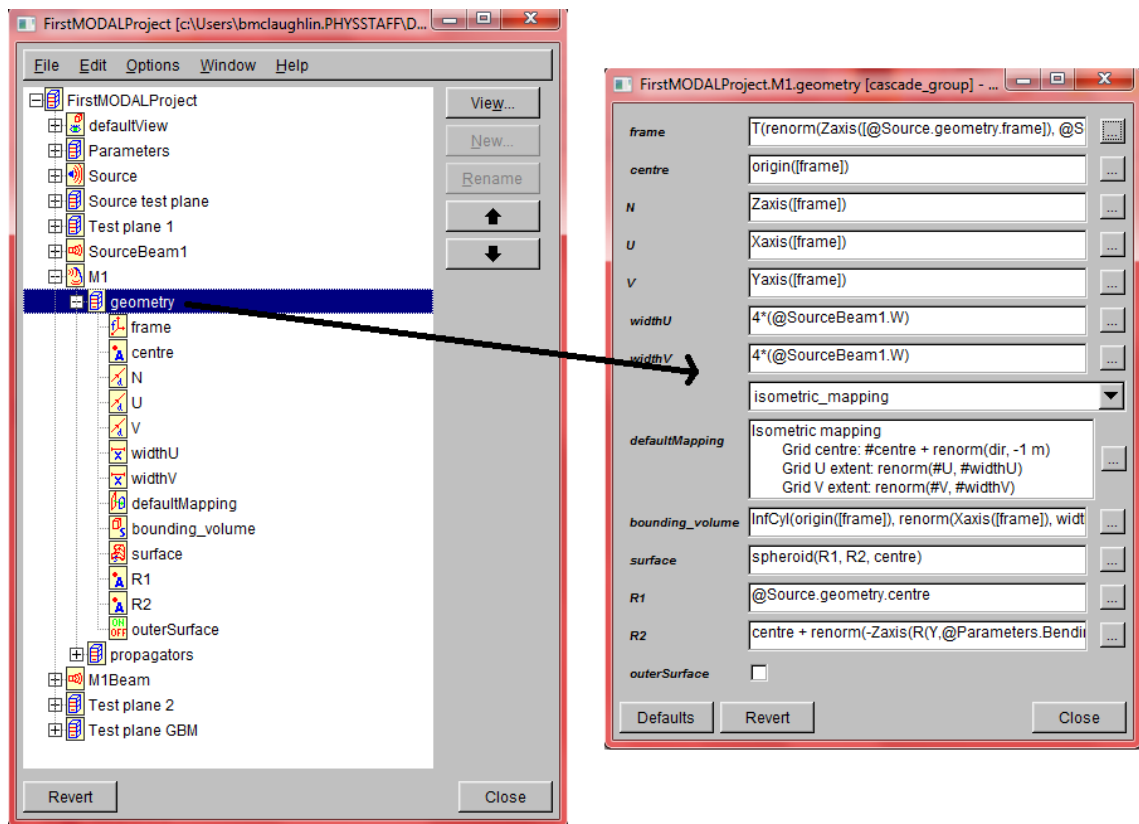

Figure 6-2: MODAL's project viewer with property editor (right).

➢ **Elements** The Elements in MODAL represent the various components that make up an optical system i.e. sources, detectors, mirrors, lenses, output planes and other passive objects such as apertures etc. There are a number of sources including corrugated conical horns, smooth walled horns, plane waves, Hermite Gaussian modes and uniformly illuminated apertures. MODAL also allows the importing of geometries files from scatter which is a piece of software also written in-house for the analysis of various horn antennas at THz frequencies.

With respect to detectors they are similar to the sources but have a set of field modes that the incident field can couple to. Also output planes allow the field to be sampled at any point in the system by simply defining an output plane at the location of interest.

All the elements have a set of properties that must be set for successful orientation in a project. Every element has a local reference frame which must be set, this is defined by a centre point and three axes (N, U, and V) which correspond to the *Z, X* and *Y* axes respectively. For some elements there are properties that are unique to it that have to be set. For sources characteristics about the input field (such as radius of curvature, frequency, polarisation etc) must be defined along with characteristics of the feed device itself, for example in the case of a corrugated horn the length of the horn, and radius of the aperture must be established.

Other optical elements also have unique properties. Lenses and Mirrors are defined in terms of their geometrical surfaces. In the case of implementing a Mirror the procedure by which the mirror is defined is dependent upon the shape of the mirror. In the case of a parabolic mirror the parabola is defined by a reference frame (whose centre can be at any point on a surface) its focal point and the direction from the focal point to the vertex. In the case of ellipsoidal and hyperbolic mirrors the characterisation of the surface is achieved again by the appropriate frame but also the location of the two focal points. Once the surface geometry of an element is defined then the section to be used can be specified using a bounding volume. A bounding volume can be any geometrical shape e.g. a cylinder which when intersected with the surface can be used to select either the section of surface outside or outside of the bounding volume (depending on definition through the geometry window of the object). The lenses are defined by setting the diameter of the lens, its thickness and also the refractive index of the material the lens is comprised off. The surface of the lens is defined in terms of it radius of curvature and conic constant i.e. the surface does not have to be spherical.

➢ **Mapping** Before any propagators are used MODAL uses a mapping system to create sample points on the elements, for the purpose of propagation calculations and also points to be plotted in the 3D viewer when illustrating the surfaces of the objects used as it establishes a relationship between U and V the reference frames and the points on the elements. Mapping in MODAL is done by using a ray tracing technique. With this technique a matrix of rays is created and projected onto the surface of interest to calculate intersection points and surface normals. There are

three main mapping methods, namely, isometric mapping, perspective mapping and uniform far field mapping. With isometric mapping the rays are launched from a 2D grid of points in a certain direction. With perspective mapping they are launched through a 2D grid from a common point of origin (see diagram below). The position of the grid can be defined by the user. The user can also select a varying number of sample points in U and V. In the case of far field mapping a uniform cone of rays is launched from an arbitrary point.
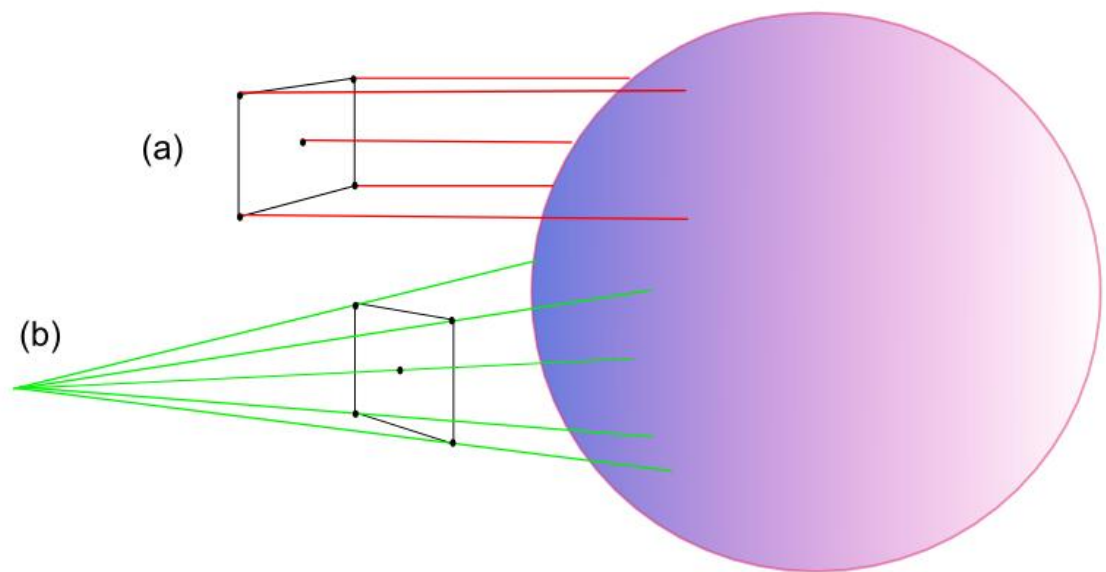

Figure 6-3: Schematic of isometric mapping (a) where rays are launched from points on a grid. Situation (b) illustrates perspective mapping where rays are launched through the points from a common point of origin.

➢ **Propagator** A propagator is used for calculating the field at an element within a system, typically using mapping. There are three main types of propagator, a source field propagator, element propagator and far field propagator. A source propagator calculates the field at a defined source in the system, the element propagator calculates the transmitted or reflected field (in a certain representation) for an element by propagating the fields to (and possibly through) the element from other/previous propagators i.e. each element propagator requires a source which is a pointer to another propagator. A far-field propagator takes a given near field and propagates it into the far field.
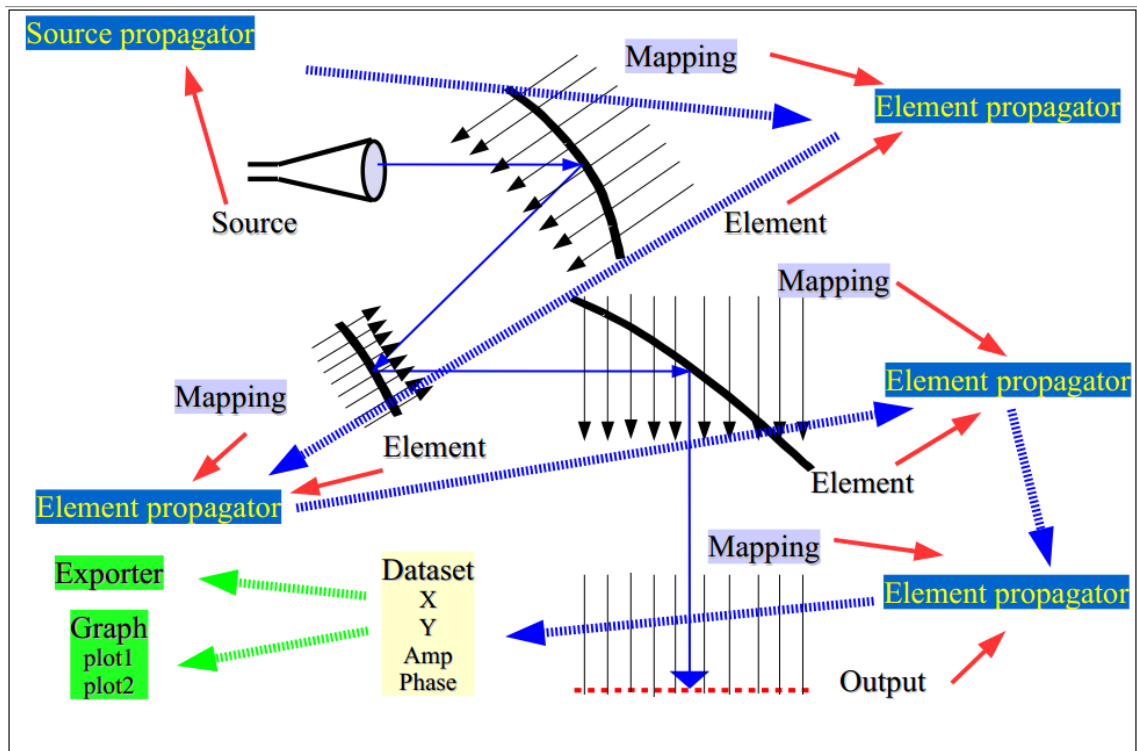
Figure 6-4: Schematic of operation of system in MODAL, where the functionality of the propagators is highlighted by thick blue arrows. Thin blue lines highlight the path of radiation from source through three mirrors to an output plane.

There are a few different field representation and propagation methods in MODAL, the near field can be represented as either a scalar electric field or a vector electric and magnetic field. The scalar field calculations are done using either Fresnel integrals as discussed in section 2.3 above or by utilising Gaussian Beam Mode Analysis as discussed in section 2.2 above. For vector analysis the field is represented using Physical Optics as presented in section 2.4 above. In a similar fashion the far field can also be represented as scalar or vector fields. Due to the adaptable nature of the software new propagation techniques can easily be added.

➢ **Beams** The ability to add beams which show the quasi-optical variation of radiation throughout the system provide a useful design tool to the designer as the system can be tweaked to what is desired e.g. a beam waist at a desired location. When the elements are in place the beams can be initialised between elements by defining an element, a source propagator and propagation distance. A 3D beam is then plotted where the beam width has been calculated using a simple ABCD matrix calculation. The beam calculations also contain information about the beam waist location so these can be calculated exactly.
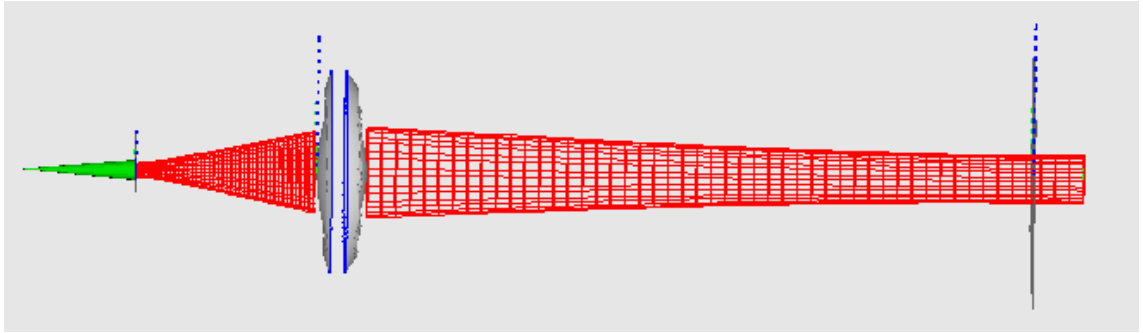
Figure 6-5: Screen shot from MODAL where radiation is propagated from a corrugated horn source through a lens and the field is being sampled (by an output plane) at a beam the waist position. The beam drawings can clearly be seen in red.

➢ **Datasets, Dataset Exporters and Sweeping Datasets** A dataset represents a structured set of columns representing numerical data. These columns are user defined and can be 1D or 2D as long as each column has the same shape. These datasets are used for accessing data accumulated by the propagators for the purposes of graphing or exporting etc. Each column will contain an aspect of the field that is of interest to the user. For example the user could define 3 columns, the first containing say *x* coordinates of field points from a propagator, the second containing *y* coordinates of the propagator and the third containing E_x the magnitude of the *x* component of the Electric field. The columns can be set to suit the user's needs, vector field columns can contain the following information:

- Propagator (source of the field)
- Wavelength (spectral component of the field)
- Component of the field: electric field E, magnetic field H, Poyinting vector S, etc.
- Cartesian component of interest in a given frame of reference
- A particular complex number component: real, imaginary part, magnitude, phase
- A unit for the values (must be consistent with the selected component)

For example the user could output the real value of the *x* component of *S* in the global frame, in W/mm^2.

A Dataset Exporter is used to save data from a dataset to a file.

A sweeping dataset is essentially the same as a regular dataset however it allows up to two parameters in a given project to be varied and key properties of the system recorded. For example consider a situation where we have an optical system

115

comprised of a source mirror and output plane. If the distance from the source to mirror is "*a*" and the distance from mirror to output is "*b*" then by setting a value range and number of steps for each the calculations will be re-run for each step along the value range i.e. property recorded as a function of position. The data is then saved to a dataset as required.

➢ **Metrics** are used to calculate certain parameters of the system numerically. The metrics that are currently available in MODAL include:

- field power - calculates the total power in a field (representation).
- field power fraction - calculates fractional power given two fields, useful for calculating truncation.
- scalar field coupling - for calculating the coupling coefficients between a field and a detector mode(s)
- GBM Mode set parameters - provide the parameters of the mode set used to describe the field
- Vector Mode coupling – calculates the coupling between a scalar field and a detector mode.

These can be calculated at any propagator in the system and therefore at any location by defining an output plane.

➢ **Graphs** As well as exporting data to a file via a dataset exporter the data can also be plotted on publication quality graphs within MODAL. XY Graphs, contour graphs, graph sets and metric graphs can all be created.
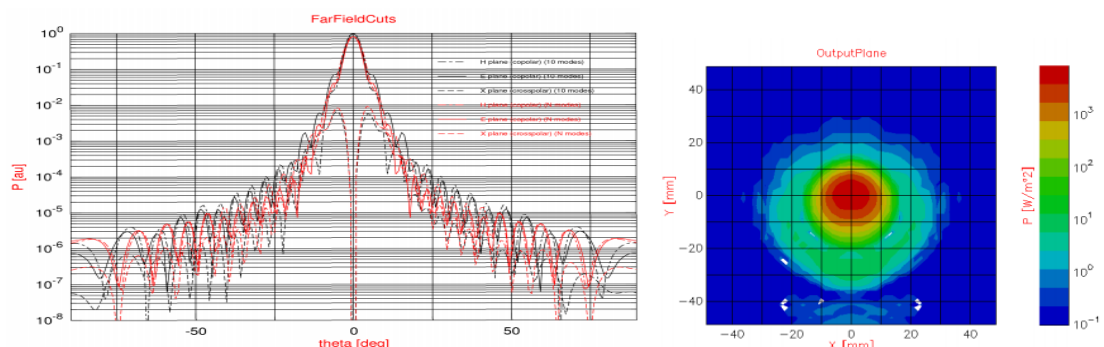

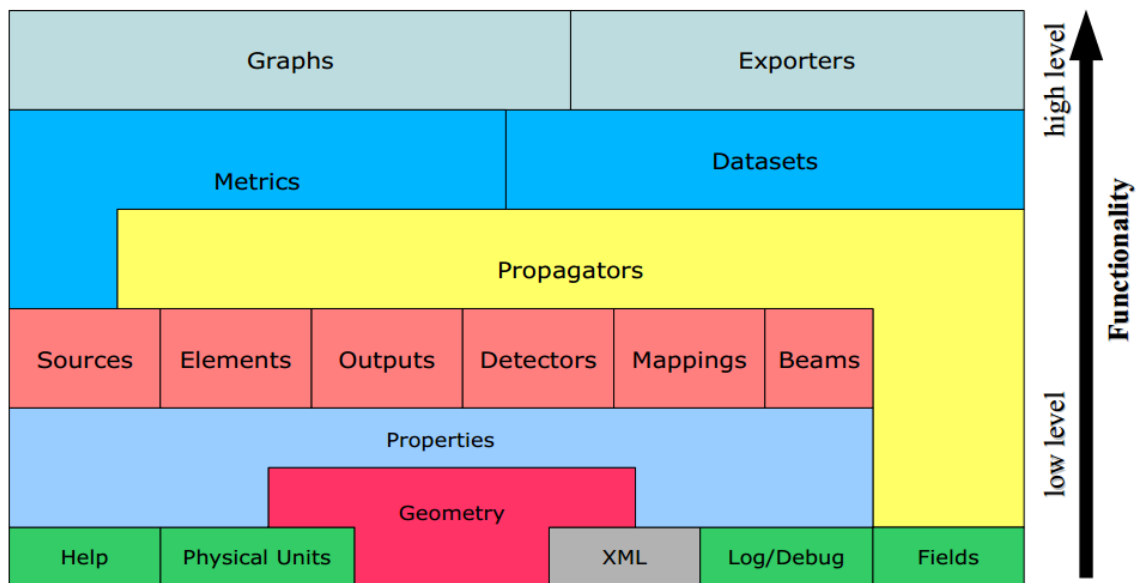*Figure 6-6: Example of XY Graph (left) and contour plot (right.)*

Figure 6-7: Diagram showing the different layers of modal and its functionality levels.

The fact that MODAL is such a user friendly package is down to three main modules namely the property module, the Geometry module and the Physical Units module. The Physical Units module consistently handles inputting and outputting of physical quantities. It knows about units (through dimensionality) i.e. it will recognise the joule as a valid unit for energy but knows that the second is not valid.

The geometry module handles geometrical objects such as scalars, points, directions, surfaces and frames. It allows the objects to be defined in terms of other objects e.g. a vector can be defined in terms of two points (A->B) or a new frame can be defined in terms of a frame and a transformation. The same hierarchal editor is used for all classes which make adding things a lot easier.

 The properties module allows all higher level objects to have a structure. Each property has its own name and can be referred to either relatively or absolutely. This allows objects to have dynamic dependencies e.g. if a graphs depends on a particular dataset it will be informed when the dataset changes. A consistent hierarchal editor is used for all objects.

7 Bibliography

1. *http://myscifi.org/wp-content/uploads/2011/04/EM-spectrum.jpg.* 12/10/2011.

2. **Goldsmith, Paul F.** *Quasioptical Systems - Gaussian Beam Quasi Optical Propagation and Applications.* s.l. : IEEE Press, 1998.

3. **R, Mahon.** *Modal analysis of millimetre wave and Terahertz imaging systems.* s.l. : NUI Maynooth PhD thesis, 2011.

4. *Terahertz Technology.* **P.H., Siegel.** 3, s.l. : IEEE transactions on microwave theory and techniques, 2002, Vol. 50.

5. **D, White.** *The developement of efficient CAD software for Terahertz Optical Design and Analysis.* s.l. : NUI Maynooth Phd Thesis, 2006.

6. *A passive milimetre wave camera for landing under Low Visibility conditions.* **Shoucri M., Davidheiser R., Hauss B., Lee P., Mussetto M., Young S and Yujiri L.** s.l. : National Telesystems Conference, 'Commercial Applications and Dual-Use Technology', conference proceedings, 1993.

7. *Passive Millimetere Wave Imaging.* **Yujiri L., Shoucri M., Moffa P.** 3, Redondo Beach, California, USA. : IEEE Microwave Magazine, 2003, Vol. 4.

8. *THz Standoff Detection and Imaging of Explosives and Weapons.* **Federici J.F., Garya D., Barat R., Zimdarsc D.** 2005. 5781.

9. *THz imaging and sensing for security application - explosives, weapons and drugs.* **Federici J.F., Schulkin B., Huang F., Dale G., Barat R., Oliveira F and Zimars D.** 7, s.l. : IOP Publishing, Semiconductor Sci, 2005, Vol. 20.

10. *Millimetre Wave and Terahertz Technology for the Detection of concealed threats - A review.* **Kemp M.C.** s.l. : Proc. of SPIE Vol. 6402 64020D-1, 2006.

11. *Terahertz imaging of subjects with concealed weapons.* **Dickinson J.C., Goyette T.M., Gatesman A.J., Joseph C.S., Root Z.G., Gilesa R.H., Waldmana J, and Nixonb W.E.** s.l. : Proceedings of SPIE, 2006. 62120Q.

12. **M., Giovenale.** *http://www.frascati.enea.it/thz-bridge/descr_gen2.htm.* s.l. : THz Bridge achievements, Objectives and expected achievements, 22/09/2011.

13. *Terahertz Imaging of burned Tissue .* **Dougherty J.P., Jubic G.D and Kiser W.L., Jr.** s.l. : Proc. of SPIE Vol. 6472, 64720N, 2007.

14. **J, Loughran.** *Terahertz Imaging for medical applications.* s.l. : NUI Maynooth, MSc thesis, 2005.

15. *http://www.rp-photonics.com/gaussian_beams.html.* s.l. : RP Photonics - Encylopedia of Laser Physics and technology, 31/08/2012.

16. **D, White.** *Computer Aided Design of Sub-Millimetre wave Quasi Optical Systems.* s.l. : NUI Maynooth MSc Thesis, 1995.

17. **Siegman A.E.** *Lasers.* Stanford : University Science Books, 1986 . 0935702115.

18. **J.A, Murphy.** *Terahertz Optics & Long wave Quasi-Optical Systems.* s.l. : Lecture Notes, 2012.

19. **Born M., Wolf E.,.** *"Principles of Optics" 7th Ed.* s.l. : Pergamon Press, 1990.

20. *http://en.wikipedia.org/wiki/Huygens%E2%80%93Fresnel_principle.* s.l. : wikipedia article on Fresnell Kirchoff diffraction, 18/10/2011.

21. **Knud Pontoppidan.** *Grasp 8 - Technical Description.* Copenhagen, Denmark : DTK, 2002. 87-989218-0-0.

22. **Colin R.E, Zucker F.J.** *Antenna Theory .* New York : Mc Graw-Hill, 1969.

23. *MODAL Overview.* **M, Gradziel.** s.l. : Presentation, 2008.

24. *Modeling of the Optical Performance of Millimeter-Wave Instruments using MODAL.* **Gradziel M.L., O‟Sullivan, C., Murphy, J. A., Cahill, G., Curran, G. S., Pryke, C., Gear, W., Church, S.,.** s.l. : SPIE Proc , 2008. 64720D.

25. *Quasi-Optical Design and Analysis of Bolometric Interferometers for Cosmic Microwave Background Experiments.* **Curran G.** s.l. : NUI Maynooth Phd Thesis, 2010.

26. **Lanigan, W.** *Automated Fourier Optics Test facility for the evaluation of Phase Gratings at 100GHz.* Maynooth : NUI Maynooth MSc Thesis, 1998.

27. **May, R.** *The developement fo Quasi-Optical Techniques for Long Wavelength Imaging.* Maynooth : NUI Maynooth Phd Thesis, 2008.

28. **Harrison, Karl.** http://www.3dchem.com/molecules.asp?ID=200. 2013.

29. **Rochester University.** *Astronomy 203/403 Fall 1999 Lecture Notes.* Rochester : Rochester University, 1999.

30. *http://www.st-andrews.ac.uk/~jcgl/Scots_Guide/RadCom/part10/page3.html.* s.l. : University of St Andrews, Web page on free space modes, 02/10/2011.

31. *http://www.microwaves101.com/encyclopedia/circulators.cfm.* Tuscon AZ : P-N Designs.inc, 10/10/2012.

32. *Resolution Capabilities of Future THz Cameras .* **J. Lizarraga, C. del Río,.** 2011.